The Dissertation Committee for Soojae Park certifies that this is the approved version of the following dissertation:

Durability of Adhesive Joints between Concrete and FRP Reinforcement in Aggressive Environments

Committee:

____

Kenneth M. Liechti, Supervisor

____

Eric B. Becker

____

Mark E. Mear

____

K. Ravi-Chandar

____

Sharon L. Wood

Durability of Adhesive Joints between Concrete and FRP Reinforcement in Aggressive Environments

by

Soojae Park, B.S., M.S.

Dissertation

Presented to the Faculty of the Graduate School of
the University of Texas at Austin
in Partial Fulfillment
of the Requirements
for the Degree of
Doctor of Philosophy

The University of Texas at Austin
August, 2004

To Jesus Christ

Acknowledgements

I would like to thank Dr. Kenneth Liechti, my advisor, who taught me everything I needed to do to finish this work. His consistent and warmhearted support cannot be overemphasized. I would like to thank the National Science Foundation (CMS-0085015) and the Department of Aerospace Engineering and Engineering Mechanics at the University of Texas at Austin for funding. All the members of my committee are greatly appreciated as well as all the professors who taught me knowledge of science and engineering. I would like to thank my colleague friends for productive discussion and information.

I would like to thank all my family members, Jin-Yi, Danny, Eugenie, Hannah and Joshua for their patient love and persistent trust.

‘Thank you, Father, for everything you supplied me in abundance through Jesus Christ.’

Durability of Adhesive Joints between Concrete and FRP Reinforcement in Aggressive Environments

Publication No. ___________

Soojae Park, Ph.D.
The University of Texas at Austin, 2004

Supervisor: Kenneth M. Liechti

The durability of the bondline between concrete and its fiber-reinforced polymer reinforcement was characterized at various temperature and humidity levels. The bondline consisted of an epoxy primer, an epoxy putty and an epoxy saturant. In principle, fracture could occur anywhere in this bondline, but attention was focused on the concrete/primer interface in this study because preliminary experiments indicated that this was the dominant failure mechanism.

The initial part of the constitutive modeling of the epoxy primer was conducted using linear viscoelastic experiments. Confined compression experiments determined two linear material functions simultaneously. Because this was a relatively new experiment, the results were validated by conducting bulk compliance experiments. The viscoelastic region of the bulk modulus was as wide as that of the tensile and shear relaxation moduli. This result contradicts previous conceptions but is agreement with some other recent observations. Thermal and hygral expansions were also measured and used in a hybrid nonlinear viscoelastic constitutive model.

The hybrid model captured the hygrothermal nonlinear viscoelastic deformation of the epoxy primer. This model is a combination of Schapery's model and Popelar's shear modified free volume model. Torsion tests were conducted and used to calibrate the distortional parameters in the free volume model. Tension experiments were performed at four different temperature and humidity levels and were used to calibrate the dilatational, thermal and hygral parameters in the hybrid model. The linear and hygrothermal nonlinear viscoelastic constitutive models were used in the analysis of time-dependent interfacial fracture between concrete and epoxy primer.

A generalized time-dependent J integral was used as a fracture parameter for characterizing the time-dependent interfacial fracture. This was used instead of the strain energy release rate and the stress intensity factor because of the nonlinear viscoelastic deformation of the primer. Schapery's pseudo stress model was calibrated using tension data at various temperature and humidity levels because it is required for the generalized J integral. An instrumented wedge test was conducted in order to determine the interfacial fracture energy at several loading rates and various temperature and humidity levels. The crack length was measured as a function of wedge speeds during steady state crack growth. The generalized J integral and cohesive zone size or failure zone size were computed using finite element analyses that incorporated the pseudo stress model. The pseudo stress model, cohesive zone size and the generalized J integral were all used to compute the work input into the failure zone, which was then equated to the fracture energy. The loading rate, temperature and humidity level all affected the fracture energy, which decreased with increasing temperature and humidity levels.

Table of Contents

1. Introduction

2. Linear Viscoelastic Behavior

2.1 Experiments

2.2 Analysis

2.2.1 *Bulk Longitudinal Relaxation Experiments*

2.3 Results and Discussion

3. Hygrothermal Nonlinear Viscoelastic Behavior

3.1 Experiments

3.2 Analysis

3.3 Results and Discussion

4.2 Pseudo Stress Model

4.3 Generalized J integral for Nonlinear Viscoelastic Media

List of Tables

List of Figures

1. Introduction

1.1 Overview

Bonding has widely been used in engineering structures as a mechanical fastening method. Carbon and glass fibers are bonded to matrix material in fiber reinforced polymers (FRP). FRP is bonded to various materials such as aluminum, ceramics, etc. Bonding offers outstanding advantages over other fastening techniques mainly by reducing stress concentrations and weight. More recently, adhesive bonding of FRP to concrete has been considered for strengthening existing civil engineering structures (Nanni, 1999). Since concrete is much weaker in tension, the reinforcement is generally needed for strengthening the parts of the structure that are under tension. Placing holes in the tension-dominated section of the structure would be detrimental due to the induced stress concentrations which generally lead to crack initiation followed by rapid crack propagation. In addition, such bonded repairs can be conducted without terminating the service life of the structures since it does not involve demolition.

The adhesives and matrix materials that will be used for such reinforcements are polymeric and time-dependent and also sensitive to the presence of solvents. Wider use of adhesive bonding has been delayed by the limited data particularly in aggressive environments. The time-dependent characteristics of the materials are often neglected in simpler elastic analyses. Furthermore, linear viscoelastic response only occurs over a small strain range but corners and cracks induce large strains and nonlinear effects.

A typical bond line consists of several components. Closest to the concrete is a thin layer of primer. This is followed by epoxy putty to level concrete bond surface. A layer of epoxy saturant is spread on top of the putty as a binder for the unidirectional fibers. More saturant is brushed over the fibers. The whole repair is then coated with a protective layer against ultraviolet radiation and abrasion. One failure mode consists of delamination between the concrete and the FRP leaving a thin layer of primer on the concrete fracture surface, indicating the failure of the primer. As a result, it is important to determine the deformation behavior of the primer over a wide range of strain at various temperature and humidity levels. This involved an examination of the linear and nonlinear viscoelastic behavior of the primer.

1.2 Literature Review of Viscoelasticity

Viscoelasticity refers to the time-dependent behavior of materials at different strain rates. The time dependence can be observed most directly in creep tests under constant loading or relaxation tests under constant strain. The material response remains linear as long as the applied strain level is small, although the same material can exhibit nonlinear response at higher strain levels.

Linear viscoelasticity under shear and tensile loadings has well been developed (Ferry, 1980). However, there is much less data available for the bulk response of viscoelastic materials. McKinney, Edelman and Marvin measured dynamic bulk viscoelastic properties (1956), using piezoelectric elements to dynamically pressurize the sample and sense its volume changes. Popelar and Liechti (1997) determined the bulk creep behavior of epoxy over a 15°C temperature range. Deng and Knauss (1997) measured the dynamic bulk compliance of Poly (Vinyl Acetate) (PVAc) over a large temperature range and observed that the transition range of the bulk response was as large as that of the shear response. Similar results were observed for the dynamic bulk compliance of Poly (Methyl Methacrylate) (PMMA) (Sane and Knauss, 2001a).

Alternatively, dynamic bulk longitudinal properties have been measured using wave propagation (Ferry, 1980). When the thickness of the specimen is much larger than the wavelength, the lateral contraction can be ignored. The resulting experimental simplicity made it more attractive than experiments that observe the quasi static response. In addition, the bulk longitudinal behavior closely approaches the bulk behavior in the rubbery regime, thereby providing a good estimate of bulk properties. However, the difference between the bulk and bulk longitudinal behavior is clearly observed in the glassy regime.

For homogeneous, isotropic and linearly viscoelastic materials, two material functions are required. In the past, these linear viscoelastic functions were determined from separate experiments. One of the methods for accomplishing this task is to measure the transverse strain in addition to the axial strain during uniaxial relaxation or creep experiments. For relatively stiff materials, strain gages are commonly used for this purpose. However, strain gages can reinforce soft polymeric materials, thereby, distorting the intrinsic material response. Even a relatively stiff polymeric material softens at high temperature making it susceptible to reinforcement by strain gages. Peretz and Weitsman (1982) considered the effect of the strain gage reinforcement on polymers. Arzoumanidis and Liechti (2003) used an axial extensometer to calibrate corrections to strain gages on urethane specimens, especially at lower frequencies. Instead of strain gages, optical interferometry has been used in the past (Romanko and Knauss, 1980). However, even small variations in the measurement of Poisson's ratio can dramatically distort the bulk modulus values obtained through interconversion (Sane and Knauss, 2001b).

In order to avoid a direct measurement of Poisson's ratio, the uniaxial modulus and shear modulus have often been separately determined due to the relative simplicity of each experiment. The bulk behavior of the material can subsequently be determined through interconversion. However, this approach has not been successful due to the fact that the viscoelastic component of the bulk behavior occurs over fewer decades than in either the tensile or shear behavior of the material (Tschoegl, Knauss and Emri, 2002). Another potential difficulty in determining bulk modulus using two separate experiments can arise due to batch to batch variations and fluctuations in ambient humidity. Humidity levels are often not carefully controlled and even small changes in humidity levels can cause large variations in material response. Consequently, the so called standard protocol of Tschoegl, Knauss and Emri (2002) was established. It required that the basic viscoelastic functions be determined simultaneously on the same specimen, under the same environmental conditions.

In addition, interconversion from tensile relaxation modulus, $E(t)$ and shear relaxation modulus, $\mu(t)$ to bulk relaxation modulus, $K(t)$ requires very precise measurements due to the characteristics of the relationship between these material functions. In Carson transform space, we have

$$\tilde{K}=\frac{\tilde{\mu}\tilde{E}}{3\left(3\tilde{\mu}-\tilde{E}\right)}, \tag{1.1}$$

where ~ indicates the Carson transform, which is the s-multiplied Laplace transform of a quantity (e.g., $\tilde{K}(s)=s\bar{K}(s)$). Looking at the denominator in Equation 1.1, the quantity $\tilde{E}$ approaches $3\tilde{\mu}$ in the rubbery regime. This makes K(t) very sensitive to even small errors in E(t) or $\mu(t)$. Thus, direct measurement of the bulk behavior is highly desirable.

Bulk longitudinal relaxation experiments were designed to satisfy these two strict requirements of the standard protocol. Through this experiment, two bulk-related material functions can be measured and converted to bulk and shear moduli. The confined cylinder configuration offers one method of achieving this.

Matsuoka and Maxwell (1958) were the first to use the confined cylinder configuration for polymer. They assumed that the confined cylinder was rigid. However, this rigid boundary condition automatically yields the bulk modulus rather than the bulk longitudinal modulus. Recently, Ma and Ravi-Chandar

(2000) measured the lateral expansion of the confining cylinder in order to include it as a realistic boundary condition. In addition, the confining cylinder acted as a barrier that constrained unstable deformations such as barreling under compression. However, this experiment was designed for aluminum which is stiff enough to create very high lateral expansion of the confining cylinder. As a result, this experiment provided axial compression with relatively small amounts of lateral pressure. Ravi-Chandar and Ma (2000) utilized the same configuration on two polymers, polycarbonate and PMMA, using several different confining cylinders in order to examine the effect of hydrostatic pressure on the large deformation behavior of the materials. This configuration will be used for in this study.

Numerous nonlinear viscoelastic models have been developed. Most of the approaches can be divided into two categories (Drozdov, 1998). In the first approach, elastic springs and viscous dashpots are combined in series and in parallel to yield so called differential models. The linear dashpot, the power-law dashpot, the Eyring dashpot and the Briant dashpots were considered separately and in combination to yield various viscoplasitc models. A variety of combinations of nonlinear elastic springs and nonlinear viscous dashpots were also examined. In all cases, increasing the number of springs and dashpots is likely to better predict the material response.

On the other hand, nonlinear integral models have been developed in one dimension, using the Boltzmann superposition principle. Guth et al. (1946) derived constitutive equations for the nonlinear viscoelastic behavior of rubber by introducing some nonlinear functions of strain to replace the strain in the linear viscoelastic constitutive equation. Talybly (1983) expressed the strain as a nonlinear function of stress in a similar manner. Makhmutov et al. (1983), and Viktorova (1983) separated one integral operator into two kernels to account the plastic effects or damage accumulation.

Leaderman (1943) introduced the concept of reduced time to incorporate the nonlinearity into the relaxation kernel in a similar manner to time-temperature superposition. The reduced time concept was connected to the free volume which was introduced by Doolittle (1951) and explicitly related by Knauss and Emri (1987) and Losi and Knauss (1992). The free volume model proposed by Knauss and Emri (1981) predicted the tensile behavior of PVAc with a shift factor that was a function of temperature and dilatation.

This free volume model was modified by Popelar and Liechti (1997) to account for the effect of shear on the free volume because a strong nonlinearity was also observed even under shear-dominated loadings. A distortional term that accounted for the effect of shear on free volume was introduced. The effect of solvent on the free volume was noted by Knauss and Kenner (1980) and Popelar and Liechti (1997). Both studies established the applicability of a time-moisture superposition. However, moisture diffusion phenomena in the material could not be fully characterized because full saturation was not possible. Popelar and Liechti (2003) employed the Tait equation to include the effect of the distortional stress to the modified free volume for urethane, which was further studied via stress-based and strain based formulations by Arzoumanidis and Liechti (2003). The effect of salt water at high temperature on the material behavior was investigated by Park and Liechti (2003). It was found that the presence of salt water produced a stronger nonlinear effect.

Schapery (1964, 1966, 1969a, 1969b, 1997) generalized nonlinear integral models for nonlinear viscoelastic media through thermodynamic developments. Most existing integral models of nonlinear behavior can be represented by this approach. It offers freedom of choice in the material parameters that need to be calibrated experimentally. Lai and Bakker (1996) extended Schapery's model (1969b) to three-dimensions.

1.3 Literature Review of Fracture Mechanics

The concrete/FRP bondline contains a number of polymeric materials. As such, it can be expected that fracture in the bondline is likely to be time-dependent and therefore involve viscoelastic fracture mechanics. Linear elastic fracture mechanics could be applicable in the glassy regime and deep in the rubbery one where the material properties are independent of time or rate. However, a linear elastic fracture mechanics approach is not suitable over the transient regime of viscoelastic materials where material responses change rapidly with applied strain rate. In this regime, the energy release rate is not well defined due to the fact that the amount of energy released depends on the loading and unloading rates in the material surrounding a crack tip. In the elastic case, the energy release rate can be obtained by comparing the energy of two states before and after crack growth. However, viscoelastic crack growth requires the time history of stress or strain during crack growth.

Knauss was one of the early pioneers who investigated the effects of rate on the crack growth behaviors of rubbery materials by making use of the infinite strip geometry (1969, 1970). It was observed that crack velocities depended on the temperature level at which the experiments were conducted and a time-temperature shift factor was applied to crack propagation data in a similar manner that it had been applied in the development of master curves for linear viscoelastic material functions. However, the lowest temperature at which the fracture experiments were conducted was above the glass transition temperature. As a result, the material far removed from the crack tip was always in the rubbery regime. Two fracture criteria were proposed; either constant crack opening displacement or constant fracture energy. Either criterion can describe crack propagation in at least one material. The fracture energy criterion was in better agreement with crack growth rate data.

Schapery developed viscoelastic fracture theories that allowed for the transient behavior of the material well removed from the crack tip and considered crack initiation and growth in linear viscoelastic media under traction-controlled loading (1975a, b, c). He applied linear viscoelasticity theories to the material outside the failure zone where the material breaks apart. He applied the extended correspondence principle that had been established by Graham (1968) to obtain the solution to the linear viscoelastic Griffith problem. He idealized the failing material within the failure zone as a constant stress region. This local energy approach with a Dugdale/Barrenblatt cohesive zone was simpler than a global approach and avoided solving boundary value problems with time-dependent material properties.

Cristensen proposed a rate-dependent criterion for crack growth in the two extreme cases of high- or low-rate conditions using a global approach from the principle of the conservation of energy (1977, 1979, 1981). He considered steady state crack growth in an infinite strip under fixed applied displacements. Because a step displacement loading was applied, the stress was assumed to be constant far away from the crack tip. As a result, it was possible to compute the global energy from the glassy and rubbery moduli. However, this approach cannot be used over the transient regime. Gamby and Chaoufi (1999) used Cristensen's criterion with material properties that had been measured at a single temperature level. Testing over a wider temperature range might be necessary for obtaining the two extreme (glassy and rubbery) material properties. The variation of the fracture energy could have been due to the dependence of the maximum strain levels on the crack velocity because the maximum strain generally depends on the strain rates prescribed.

The C_t parameter was introduced for creep crack growth in the steady state creep regime (Saxena, 1986). This parameter can be easily measured and used for steady state creep, which corresponds to a linear analysis. Tertiary creep is more likely to occur at the crack tip due to the large deformation experienced there.

A viscoelastic cohesive zone model was developed using a micromechanical approach (Allen and Searcy, 2001). Cohesive zone models have been recently used for crack analysis as a means of representing the failing material near a crack tip even though experimental calibration is extremely difficult. This has caused difficulties in the transferability of cohesive zone parameters between different specimen geometries and loading types (Georgiou et al., 2004). Allen and Searcy replaced the material heterogeneity in the damaged zone by an equivalent area with effective homogeneous material properties, which included the tensile relaxation modulus of a fibril.

Kaminsky and Chernoivan (2002) considered a linear viscoelastic fracture problem with prescribed displacement using rigid growing wedge. They used a time-dependent cohesive zone length in conjunction with a constant stress in the traction-separation law. This analysis may account for crack initiation, but is not suitable for crack propagation because it made use of a correspondence principle which could not entertain moving boundaries.

Schapery was probably the first to include a region of nonlinearly deforming material between the linearly deforming and failing materials. The stress over the failure zone was allowed to be time-dependent. All previous works had focused on the fracture process zone and a region of linear viscoelasticity. Schapery developed a nonlinear viscoelastic constitutive model which was specially required for use with the generalized J integral (1981, 1984, 1986, 1990). By introducing pseudo models for nonlinear viscoelastic constitutive relationships, Schapery was able to establish simpler correspondence principles between mechanical states of elastic and viscoelastic media, which did not require Laplace transformation. Eventually, the generalized J integral was proposed as a nonlinear viscoelastic fracture parameter which allowed the fracture energy to be expressed as a product of a linear viscoelastic function with the generalized J integral.

Williams (1959) determined the asymptotic fields for a crack between two dissimilar materials. The asymptotics contained a so-called oscillatory singularity which gave a rise to interpenetration of the crack faces near the crack tip. The concept of the complex stress intensity factor for interface cracks was introduced by Rice and Shih (1965) and Dundurs' parameters (1969) were presented that reduce the total number of independent linear elastic constants for a bimaterial to two. The complex stress intensity factor was further developed (Hutchinson et al., 1987 and Rice, 1988). Shih and Asaro (1988) used J_2 deformation theory with power-law strain hardening for an elastic-plastic medium bonded to a rigid substrate. HRR-type singularities were observed over the plastic zone and the complex stress intensity factors were determined over the zone of K-dominance.

Cao and Evans (1989) determined that interfacial toughness depended on mode-mix. Liechti and Chai (1992) determined the interfacial fracture toughness of a glass/epoxy interface for various mode-mixes. A rate dependent plasticity model was used for the epoxy in conjunction with a cohesive zone model in a finite element analysis that determined the contribution of viscoplastic dissipation to the interfacial fracture (Swadener and Liechti, 1998). Liechti and Wu (2001) used rate-dependent traction-separation law by using a nonlinear Kelvin unit for a cohesive zone.

1.4 Objective and Approach

The objective of this study was to study the fracture behavior between concrete and external CFRP reinforcement in aggressive environments. The overall approach consisted of experiments, analyses and computations. New experimental techniques were developed in order to establish a three-dimensional nonlinear viscoelastic constitutive model at various temperature and humidity levels. Driven wedge experiments were used to examine interfacial crack growth between concrete and an epoxy primer, again over a range of temperature and humidity levels.

Linear and nonlinear viscoelastic constitutive models were developed in order to capture the time-dependent characteristics of the epoxy primer that was used in the bondline. A nonlinear viscoelastic fracture analysis of the interfacial fracture between concrete and the epoxy primer was performed in order to determine the fracture energy at various crack growth rates and temperature and humidity levels.

The models developed in this study provide a basis for durability analyses of concrete/FRP bondlines that can account for diffusion-assisted fracture.

2. Linear Viscoelastic Behavior

In this section, we describe a series of experiments and analyses that were used to characterize the linear viscoelastic behavior of the primer. Two types of experiments were conducted; (a) bulk longitudinal relaxation and (b) bulk creep. The analyses were used to extract the bulk and shear relaxation moduli of the primer.

2.1 Experiments

The advantage of conducting bulk longitudinal relaxation experiments is that two linear viscoelastic functions can be determined simultaneously. The bulk creep experiments were used to check the properties extracted from bulk longitudinal relaxation experiments. Both experiments were conducted in an environmental chamber for temperature control.

2.1.1 *Bulk Longitudinal Relaxation Experiments*

Bulk longitudinal relaxation experiments were performed on a solid cylindrical specimen with a diameter of 3.3 cm and a length of 5.72 cm as shown in Figure 2.1. A 6.35-cm long steel confining cylinder had an inner diameter of 3.3 cm and an outer diameter of 3.89 cm. These dimensions were chosen on the basis of Lamé’s solution for a thick-walled cylinder and balanced the need to minimize lateral strains while ensuring that they were measurable. The internal surface of the confining cylinder was honed in order to minimize friction between the specimen and the confining cylinder. The epoxy primer resin and hardener were mixed with a 10:3 weight ratio and poured into the confining cylinder. Bubbles were removed under vacuum. After the specimen was cured at ambient temperature for 7 days, it was placed in an oven at 91°C for 36 hours. This latter conditioning step produced specimens with Fickian diffusion characteristics. The specimen was then removed from the confining cylinder so that the ends could be machined perpendicular to the specimen axis.

The specimen was returned to the confining cylinder and was compressed in the axial direction by the pistons at the top and the bottom (Fig. 2.1). Their displacements were measured by two LVDT's. A servohydraulic, uniaxial testing machine was used to apply the compressive load. Due to the high sensitivity of the bulk response of the material to the machine stiffness, the local rather than the global displacement was controlled. A step history in the local displacement was maintained through feedback control. The nominal longitudinal strain was 5×10^{-4} m/m.

Two strain gages were installed on the external surface of the confining cylinder in order to measure the hoop strain which could be related to the radial strain of the specimen and the traction on the internal surface of the confining cylinder using Lamé's solution. Due to thick wall of the confining cylinder, which was designed to minimize the lateral strain, the noise-to-signal ratio had to be kept low, so shielded wires were used to eliminate various sources of noise. Because the hoop strain gages were not temperature compensated in the Wheatstone bridge circuit, a temperature correction was applied to the strain gage signals (Micro-Measurements) at higher temperatures. The axial stress was determined from the load cell signal and the cross sectional area of the specimen.

The applicability of Lamé's solution was checked by applying internal pressure to the confining cylinder which was filled with glycerin and compressed by the pistons with O-ring seals. The measured hoop strains were in very good agreement with Lamé's solution when a plane stress condition was used.

To ensure the alignment of the compression platens, an initial axial loading was applied and removed. This resulted in self-alignment of two compression platens. Full contact between the specimen and the internal wall of the confining cylinder was obtained by applying a constant displacement rate until a consistent slope in the load-displacement response was observed. Several small preloads were applied for several hours in order to ensure that the full contact had occurred. A temperature chamber maintained the target temperature to within approximately 1°C. However, the temperature of the specimen was held to a much closer tolerance due to the fact that the specimen was placed in the confining cylinder which acted as a heat reservoir. The load, LVDT displacements and hoop strains were recorded using a custom LabView program on a personal computer with a 16-bit A/D board (National Instruments PCI-MIO-16XL).

2.1.2 *Bulk Creep Experiments*

Bulk creep experiments were performed as a check on the validity of the bulk longitudinal experiments. Unlike most bulk creep experiments, very low pressure levels were required for the current experiments. This was achieved by effectively increasing the gage length of the specimen by folding it.

Bulk creep experiments were performed on nominally 0.5 mm thick strips of epoxy primer with a width of 1.3 cm and a length 2.67 cm as shown in Figure 2.2. The epoxy strips were glued to stainless steel shims in a zigzag manner. A total of 22 layers yielded an effective gage length of 58.7 cm. The specimen system of epoxy and stainless steel shims were mounted in a cylindrical pressure vessel made of glass through which the deformation of the specimen was observed. In order to prevent diffusion effects, glycerin was used as the pressurizing fluid instead of water.

The pressure was created by compressing the fluid with the actuator of a servohydraulic, uniaxial testing machine. A 138 kPa-pressure transducer measured pressure levels. The measured pressure signal was fed back to the controller which maintained constant pressure levels.

As seen in Figure 2.2, the dilatation of each layer of the specimen added to the deformation of its neighbor, thus creating a magnified displacement between the top layer of the specimen and the fixed reference point at the bottom. The uniformity of the contraction of each layer was reflected in the apparent shearing angle.

A telemicroscope (Questar QM1) was used to measure the accrued displacement of the specimen system which was placed in an oven for high temperature experiments. The microscope has a working distance of 0.61m. An overall schematic of the apparatus is shown in Figure 2.3.

A fully automated, real-time video tracking technique was used to measure the displacement using LabView with IMAQ (National Instruments). Edge detection was used with a clamping feature in order to measure the distance between the specimen and the fixed reference post. The resulting resolution in strain was as small as 6×10^{-7} m/m based on the elongated gage length. This automated real-time video tracking technique was convenient for measuring the dilatation because the measurement was essentially made outside the pressure vessel.

Because the displacement was magnified by a factor of 22, relatively low pressure levels were required to create measurable strain levels. The maximum pressure levels ranged from 276 to 676 kPa, which allowed the pressure vessel to be made of glass. The resulting strain levels were on the order of 1×10^{-4} m/m, which were ideal for linear viscoelastic behavior. The temperature chamber maintained the temperature to within approximately 1°C. However, the temperature in the pressure vessel was much more uniform due to the fact that the specimen was placed in the glycerin which acted as a heat reservoir. The pressure and local strain measurement were recorded using a custom LabView program with a personal computer and a 16-bit A/D board.

2.1.3 *Thermal and Hygral Expansion*

The models of nonlinear viscoelastic behavior that will be considered in this study require the coefficients of thermal and hygral expansion. This section describes the experiments that were conducted for this purpose.

The temperature and humidity levels for the experiments ranged from 29 to 49°C and 35 to 95% RH at 40.6°C, respectively. The experiments were performed on dog-bone specimens with gage sections that were nominally 5.08 cm long by 2.0 mm wide and 0.5 mm thick. These were the same specimens that were used for uniaxial tension (Fig. 3.2). The specimens were cut from a sheet using a special punch. The small thickness was required in order to minimize saturation times which were estimated using Fickian diffusion. The same environmental chamber and extensometer that were used in the uniaxial tension experiments were also used to control and measure, respectively, the thermal and hygral expansions.

The coefficient of thermal expansion was measured by raising the temperature in a series of steps. The expansion was measured once the specimen had equilibrated at each temperature level. Once the thermal behavior of the material response had been determined, the hygral effect was examined at a series of humidity levels at a fixed temperature level of 40.6°C. In order to ensure hygral equilibrium at each level, the time required for 95% of complete saturation was computed using Fick's law:

$$t = \frac{s^2}{D}\left[\frac{\ln(1-G)}{-7.3}\right]^{\frac{1}{0.75}}, \tag{2.1}$$

where s is the thickness of the specimen and D_x is the diffusivity (Shen and Springer, 1976). The diffusivity of the epoxy primer at 40.6°C was provided by

Roy (2003). The quantity G is the degree of saturation; in this case it was taken to be 95%. At each relative humidity level in the experiments, at least 25 hours was needed for this level of saturation.

2.2 Analysis

This section provides the analysis that is needed to extract the linear viscoelastic property functions from the bulk longitudinal relaxation and the bulk creep experiments. The stress analysis of the former is more involved. In addition, the procedures that were used to obtain other linear viscoelastic property functions from the original ones are described.

2.2.1 *Bulk Longitudinal Relaxation Experiments*

Two linear viscoelastic functions were determined from the bulk longitudinal relaxation tests. Lame's solution for a thick-walled cylinder was used to determine the boundary conditions in the radial direction.

2.2.1.1 *Linear Viscoelastic Constitutive Equations*

A linear viscoelastic constitutive equation for homogeneous and isotropic materials can be written with a single index as

$$\sigma_i = \int_0^t C_{ij}(t-\tau)\frac{\partial \varepsilon_j}{\partial \tau}d\tau \qquad \text{i= 1, 2, …, 6,} \qquad (2.2)$$

where $\sigma_1 = \sigma_{11}, \sigma_2 = \sigma_{22}, \sigma_3 = \sigma_{33}$, $\sigma_4 = \sigma_{23}$, $\sigma_5 = \sigma_{13}$, $\sigma_6 = \sigma_{12}$, $\varepsilon_1 = \varepsilon_{11}$, $\varepsilon_2 = \varepsilon_{22}$, $\varepsilon_3 = \varepsilon_{33}$, $\varepsilon_4 = 2\varepsilon_{23}$, $\varepsilon_5 = 2\varepsilon_{13}$, $\varepsilon_6 = 2\varepsilon_{12}$ and $C_{ij}(t)$ is the stiffness matrix.

$$C_{ij}(t) = \begin{bmatrix} C_{11}(t) & C_{12}(t) & C_{12}(t) & 0 & 0 & 0 \\ C_{12}(t) & C_{11}(t) & C_{12}(t) & 0 & 0 & 0 \\ C_{12}(t) & C_{12}(t) & C_{11}(t) & 0 & 0 & 0 \\ 0 & 0 & 0 & C_{44}(t) & 0 & 0 \\ 0 & 0 & 0 & 0 & C_{44}(t) & 0 \\ 0 & 0 & 0 & 0 & 0 & C_{44}(t) \end{bmatrix} \tag{2.3}$$

where $C_{44}(t) = \frac{1}{2}\left[C_{11}(t) - C_{12}(t)\right]$.

Thus, only two linear viscoelastic functions out of $C_{11}(t), C_{12}(t)$ and $C_{44}(t)$ need to be determined.

When the coordinate system is numbered as, z=1, r=2, $\theta = 3$ for bulk longitudinal relaxation experiments, a step-loading in axial strain applied at t=0 is

$$\varepsilon_1 = \varepsilon_1^o H(t) \tag{2.4}$$

where ε_1^o is constant and $H(t)$ is the Heaviside function.

Due to the flexibility of the confining cylinder, the radial strain in the specimen will be nonzero. However, as a first approximation, the radial and hoop strain are taken to be zero, but the actual strains are used to compute the radial traction. Thus,

$$\varepsilon_i = 0, \quad \text{i= 2, 3, .., 6} \tag{2.5}$$

Since the axial stress, $\sigma_1(t)$ was measured by the load cell and the radial and hoop stresses, $\sigma_2(t) = \sigma_3(t)$, were determined from the strain gages on the external surface of the confining cylinder, substituting the strains and the stresses into the constitutive equations yields

$$C_{11}(t) = \frac{\sigma_1(t)}{\varepsilon_1^o}, \quad C_{12}(t) = \frac{\sigma_2(t)}{\varepsilon_1^o}. \tag{2.6}$$

The components of $C_{ij}(t)$ can be related to the bulk relaxation modulus, $K(t)$ and the shear relaxation modulus, $\mu(t)$ through a different form of the linear viscoelastic constitutive equations. One of the constitutive equations which relates the components of $C_{ij}(t)$ to $K(t)$ and $\mu(t)$ in a linear manner is

$$\begin{aligned}\sigma_{ij}(t) &= \int_0^t K(t-\tau)\frac{\partial \varepsilon_{kk}(\tau)}{\partial \tau}\delta_{ij}d\tau + \int_0^t 2\mu(t-\tau)\frac{\partial e_{ij}}{\partial \tau}d\tau \\ &= \int_0^t K(t-\tau)\frac{\partial \varepsilon_{kk}(\tau)}{\partial \tau}\delta_{ij}d\tau + \int_0^t 2\mu(t-\tau)\frac{\partial}{\partial \tau}\left[\varepsilon_{ij}(\tau) - \frac{\varepsilon_{kk}(\tau)}{3}\delta_{ij}\right]d\tau,\end{aligned} \tag{2.7}$$

where e_{ij} is a strain deviator.

Substituting $\varepsilon_{11}(t)$ as the only nonzero strain yields

$$\sigma_{11}(t) = \int_0^t \left[K(t-\tau) + \frac{4}{3}\mu(t-\tau)\right]\frac{\partial \varepsilon_{11}(t)}{\partial \tau}d\tau \tag{2.8}$$

For $\varepsilon_{11} = \varepsilon_{11}^{o}H(t)$,

$$\sigma_{11}(t) = \left[K(t) + \frac{4}{3}\mu(t)\right]\varepsilon_{11}^{o} \tag{2.9}$$

The hoop stress, $\sigma_{22}(t)$ is known from the strain gages and Lamé's solution and is also given by

$$\sigma_{22}(t) = \int_0^t \left[K(t-\tau) - \frac{2}{3}\mu(t-\tau)\right]\frac{\partial \varepsilon_{11}(\tau)}{\partial \tau}d\tau \tag{2.10}$$

Again, for $\varepsilon_{11} = \varepsilon_{11}^{o}H(t)$,

$$\sigma_{22}(t) = \left[K(t) - \frac{2}{3}\mu(t)\right]\varepsilon_{11}^{o} \tag{2.11}$$

Thus, comparing Equations (2.6), (2.9) and (2.11), we have

$$C_{11}(t) = K(t) + \frac{4}{3}\mu(t), \qquad C_{12}(t) = K(t) - \frac{2}{3}\mu(t) \tag{2.12}$$

$C_{11}(t)$ is usually referred to as M(t), the bulk longitudinal relaxation modulus [Ferry, 1980]. Equation (2.12) indicates that, once $C_{11}(t)$ and $C_{12}(t)$ are found, the bulk modulus, $K(t)$ and the shear modulus, $\mu(t)$ can also be determined. Note that since $C_{11}(t)$ and $C_{12}(t)$ are linear combinations of $K(t)$ and $\mu(t)$, Carson transformations were not needed here.

2.2.1.2 *Lamé's Solution for Thick-walled Cylinder*

Lamé's solution for a thick-walled cylinder under internal pressure, p_i and plane stress was used. The plane stress condition was employed because the confining cylinder was free to move in the axial direction.

The solution for a hollow cylinder with an inner radius, a and an outer radius, b is given by

$$\sigma_{rr}(r) = \frac{a^2 p_i}{b^2 - a^2}(1 - \frac{b^2}{r^2}),$$

$$\sigma_{\theta\theta}(r) = \frac{a^2 p_i}{b^2 - a^2}(1 + \frac{b^2}{r^2}),$$

$$\varepsilon_{zz}(r) = \frac{-2\nu}{E}\frac{a^2 p_i}{b^2 - a^2} \tag{2.13}$$

and

$$u_r(r) = \frac{a^2 p_i r}{E(b^2 - a^2)}\left[(1-\nu) + (1+\nu)\frac{b^2}{r^2}\right].$$

On the internal surface of the confining cylinder (r=a) and denoting the ratio, $R = b/a$,

$$\sigma_{rr}(a) = \frac{p_i}{R^2 - 1}(1 - R^2),$$

$$\sigma_{\theta\theta}(a) = \frac{p_i}{R^2 - 1}(1 + R^2) \tag{2.14}$$

and

$$u_r(a) = \frac{p_i a}{E(R^2 - 1)}\left[(1-\nu) + (1+\nu)R^2\right].$$

On the external surface of the confining cylinder (r=b),

$$\sigma_{rr}(b) = 0,$$

$$\sigma_{\theta\theta}(b) = 2\frac{p_i}{R^2 - 1},$$

$$\varepsilon_{\theta\theta}(b) = 2\frac{p_i}{E(R^2 - 1)} \tag{2.15}$$

and

$$u_r(b) = 2\frac{p_i}{E(R^2 - 1)}Ra.$$

The hoop strain on the external surface is related to the internal pressure through

$$p_i = \frac{1}{2}E\varepsilon_{\theta\theta}(b)(R^2 - 1), \tag{2.16}$$

which is also radial stress applied to the specimen.

The radial displacement on the internal surface can be related to the hoop strain on the external surface via

$$u_r(a) = \frac{a}{2}\left[(1-\nu) + (1+\nu)R^2\right]\varepsilon_{\theta\theta}(b). \tag{2.17}$$

Due to full contact throughout the experiments, this is also the radial displacement of the outer surface of the specimen. Thus, the radial strain in the specimen is

$$\varepsilon_{rr} = \left[(1-\nu) + (1+\nu)R^2\right]\frac{\varepsilon_{\theta\theta}(b)}{2}. \tag{2.18}$$

Equations 2.16 and 2.18 indicate that the radial and hoop stresses and the radial strain in the specimen can be obtained from measurements of the hoop strain on the external surface of the confining cylinder.

2.2.1.3 *Correction for a Compliant Confining Cylinder*

The bulk longitudinal relaxation modulus, M(t) was obtained (Eqn. 2.6) under the assumption that the axial strain was the only nonzero one. However, the confining cylinder does deform and this effects the extraction of the bulk longitudinal relaxation modulus.

Taking into account the nonzero radial and hoop strains in the specimen leads (Eqn. 2.1) to

$$\sigma_1(t)=\int_0^t C_{11}(t-\tau)\frac{\partial\varepsilon_1(\tau)}{\partial\tau}d\tau+2\int_0^t C_{12}(t-\tau)\frac{\partial\varepsilon_2(\tau)}{\partial\tau}d\tau$$

and (2.19)

$$\sigma_2(t)=\int_0^t C_{12}(t-\tau)\frac{\partial\varepsilon_1(\tau)}{\partial\tau}d\tau+\int_0^t\left[C_{11}(t-\tau)+C_{12}(t-\tau)\right]\frac{\partial\varepsilon_2(\tau)}{\partial\tau}d\tau,$$

where $C_{12}(t)=C_{13}(t)$ and $\varepsilon_2(t)=\varepsilon_3(t)$.

For $\varepsilon_1=\varepsilon_1^o H(t)$ and $\varepsilon_2=\varepsilon_2(t)$,

$$\sigma_1(t)=C_{11}(t)\varepsilon_1^0+2\int_0^t C_{12}(t-\tau)\frac{\partial\varepsilon_2(\tau)}{\partial\tau}d\tau$$

and (2.20)

$$\sigma_2(t)=C_{12}(t)\varepsilon_1^0+\int_0^t\left[C_{11}(t-\tau)+C_{12}(t-\tau)\right]\frac{\partial\varepsilon_2(\tau)}{\partial\tau}d\tau.$$

If the magnitude, ε_2^0 of $\varepsilon_2(t)$ cannot be neglected and it does not vary over the period of time during which the load is applied, it can be taken to be a step function $\varepsilon_2^0 H(t)$, which leads to

$$\sigma_1(t)=C_{11}(t)\varepsilon_1^0+2C_{12}(t)\varepsilon_2^0$$

and (2.21)

$$\sigma_2(t)=C_{12}(t)\varepsilon_1^0+\left[C_{11}(t)+C_{12}(t)\right]\varepsilon_2^0.$$

Denoting the values of $C_{11}(t)$ and $C_{12}(t)$ obtained from a rigid confining cylinder as $C_{11}^0(t)$ and $C_{12}^0(t)$, the step-function corrected values are

$$C_{11}^{S}(t)=\frac{\sigma_1(t)-2\varepsilon_2^0 C_{12}^0(t)}{\varepsilon_1^0}$$

and (2.22)

$$C_{12}^{S}(t)=\frac{\sigma_2(t)-\varepsilon_2^0 C_{11}^0(t)}{\left[\varepsilon_1^0+\varepsilon_2^0\right]}.$$

Note that when $\varepsilon_2^o=0$, $C_{11}^S(t)=C_{11}^0(t)$ and $C_{12}^S(t)=C_{12}^0(t)$.

If $\varepsilon_2(t)$ varies during loading, it can be taken as $\varepsilon_2(t)=\varepsilon_2^0\left[H(t)+f(t)\right]$, where *f(t)* represents the change in the measured hoop strain.
Denoting $C_{11}(t)$ as the fully corrected value leads to

$$C_{11}(t)=C_{11}^S(t)-\frac{2\int_0^t C_{12}^0(t-\tau)\varepsilon_2^0\dot{f}(\tau)d\tau}{\varepsilon_1^0} \tag{2.23}$$

Note that $C_{12}^0(t)$ appears in Equation 2.23. However, $C_{12}^S(t)$ is already known from Equation 2.22 and is a better estimate of $C_{12}(t)$. Thus, a better estimate of $C_{11}(t)$ is

$$C_{11}(t)=C_{11}^S(t)-\frac{2\int_0^t C_{12}^S(t-\tau)\varepsilon_2^0\dot{f}(\tau)d\tau}{\varepsilon_1^0} \tag{2.24}$$

Note that if *f(t)* = 0, $C_{11}(t)$ is the same as $C_{11}^S(t)$.

Similarly,

$$C_{12}(t)=\frac{\sigma_2(t)-\varepsilon_2^0 C_{11}(t)}{\left[\varepsilon_1^0+\varepsilon_2^0\right]}-\int_0^t\left[C_{11}(t-\tau)+C_{12}^S(t-\tau)\right]\varepsilon_2^0\dot{f}(\tau)d\tau \tag{2.25}$$

Note that the true value of $C_{12}(t)$ was not used in Equation 2.24, so the current value of $C_{12}(t)$ was substituted for $C_{12}^S(t)$ in Equation 2.24 and an updated value of $C_{11}(t)$ was substituted in Equation 2.25. It was found that this one iteration was sufficient for determining the accurate values of $C_{11}(t)$ and

$C_{12}(t)$. This indicates that the optimum degree of confinement had been obtained. More iterations would otherwise have been required. The rapid convergence can be seen in Figure 2.4, which shows that it is relatively easy to account for the compliant confining cylinder.

2.2.2 *Bulk Creep Experiments*

The bulk creep compliance, $B(t)$ is obtained by applying a hydrostatic pressure, $p(t) = p_0 H(t)$ and measuring the dilatation, $\theta(t)$. For small deformations, the dilatation is the sum of three normal strains. Under hydrostatic pressure, these have the same magnitude, making the dilatation three times the measured strain.

The bulk creep compliance is defined as

$$B(t) = -\frac{\theta(t)}{p_o}. \tag{2.26}$$

2.2.3 *Interconversion*

The linear viscoelastic functions for an isotropic material are related in the Carson transform domain because their relationships can be expressed in the same form as they are in linear elasticity. In the Carson transform domain, the linear viscoelastic constitutive equations (Eqn. 2.2) become

$$\bar{\sigma}_i = \tilde{C}_{ij}\bar{\varepsilon}_j. \tag{2.27}$$

Because $K(t)$ and $\mu(t)$ can be obtained from $C_{11}(t)$ and $C_{12}(t)$, all the other linear viscoelastic functions can be derived from them. The three linear viscoelastic functions required in this study are

$$\tilde{E} = \frac{9\tilde{K}\tilde{\mu}}{3\tilde{K} + \tilde{\mu}}, \quad \tilde{\nu} = \frac{1}{2}\left[\frac{3\tilde{K} - 2\tilde{\mu}}{3\tilde{K} + \tilde{\mu}}\right] \quad \text{and} \quad \tilde{B} = \frac{1}{\tilde{K}}. \tag{2.28}$$

where $E(t)$ is the tensile relaxation modulus, $\nu(t)$ is the relaxation Poisson's ratio and $B(t)$ is the bulk creep compliance.

The first step for interconversion was to fit $K(t)$ and $\mu(t)$ with the Prony series

$$K(t) = K_\infty + \sum_{m=1}^{M} K_m e^{-\frac{t}{\rho_m^K}}$$

and (2.29)

$$\mu(t) = \mu_\infty + \sum_{m=1}^{M} \mu_m e^{-\frac{t}{\rho_m^\mu}}.$$

The coefficients of 19-term Prony series for each function are listed in Table 1. They were determined using a collocation method.

The Carson transforms of $K(t)$ and $\mu(t)$ were used obtain $\tilde{E}(s)$, $\tilde{\nu}(s)$ and $\tilde{B}(s)$ and their Laplace transforms. The inverse Laplace transforms were obtained using a collocation method to obtain $E(t)$, $\nu(t)$ and $B(t)$.

The Laplace inversion scheme was checked by taking the Carson transform of $K(t)$ and converting $\bar{K}(s)$ back to $K(t)$. Good agreement was obtained. The linear viscoelastic functions, $E(t)$, $\nu(t)$ and $B(t)$ were fitted with 19-term Prony Series (Table 1).

2.3 Results and Discussion

The results from the bulk longitudinal relaxation and bulk creep experiments are now presented. The effectiveness of the interconversion process is examined and the data for $E(t)$, $\nu(t)$ and $B(t)$ are given.

2.3.1 *Bulk Longitudinal Relaxation Experiment*

Bulk longitudinal relaxation experiments were performed at various temperature levels. The bulk relaxation modulus, $K(t)$ and the shear relaxation modulus, $\mu(t)$ were obtained from $C_{11}(t)$ and $C_{12}(t)$ through simple algebraic operations. It was necessary to use the iterative scheme outlined above to obtain $C_{11}(t)$ and $C_{12}(t)$ in spite of the relatively thick wall of the confining cylinder.

In order to ensure linearity, the axial strain in every experiment was less than 0.1%. $C_{11}(t)$ was obtained at various temperature levels from 10.7°C to 75°C in Figure 2.5 and was a monotonically decreasing function. On the other hand, at each temperature, $C_{12}(t)$ was nearly constant or slightly decreased with time (Fig. 2.6).

The bulk relaxation modulus, $K(t)$ was determined from $C_{11}(t)$ and $C_{12}(t)$ at the corresponding temperature levels in Figure 2.7. It exhibited noticeable temperature dependence. The rubbery state was clearly observed even though the glassy was not. Testing at lower temperature levels would have been required to completely capture the glassy modulus. However, this was not needed for the nonlinear viscoelastic modeling which follows. Time-temperature superposition was applied to the bulk modulus using horizontal shifting to form a master curve (Fig. 2.8). The bulk modulus was expressed as a Prony series with 19 terms in Table 1.

The shear relaxation modulus, $\mu(t)$ was determined from $C_{11}(t)$, $C_{12}(t)$ at various temperature levels as shown in Figure 2.9. The shear relaxation modulus exhibited a stronger dependence on temperature and time than did the bulk modulus. Horizontal shifting was performed in the same manner as for the bulk modulus in Figure 2.10 and the master curve was fit to a Prony series with 19 terms (Table 1).

The thermal shift factors for the bulk and shear relaxation moduli are shown in Figure 2.11. Their values were mostly the same except between 50 and 65°C where slightly more shifting was required for the bulk relaxation modulus. The data was used to fit Arrhenius and WLF expressions below and above the glass transition temperature (T_g, determined below), respectively.

The Arrhenius shift factor can be expressed as

$$\log a_T = \frac{\Delta F}{2.303R}\left(\frac{1}{T} - \frac{1}{T_M}\right), \tag{2.30}$$

where ΔF is the activation energy per gram mole and R =1.987 ($cal / g - mole\,^{O}K$) is the universal gas constant. The relationship between $\log a_T$ and the reciprocal of absolute temperature is linear. For the primer being considered here, ΔF was 59237 $cal / g - mole\,^{O}K$ and T_M was taken to be T_g.

Above the glass transition, the data was compared to the WLF equation

$$\log a_T = \frac{-C_1(T - T_M)}{(C_2 + T - T_M)} \tag{2.31}$$

with the commonly accepted WLF constants, C_1 = 8.86 ($^{o}C^{-1}$)and C_2 =101.6 (^{o}C) (Williams et al., 1955) with the reference temperature, $T_M = T_g$ + 50°C. Good agreement between the data and the WLF equation was obtained, with some variation in the middle of the temperature range.

In order to determine the glass transition temperature, the loss tangent was computed from $C_{11}(t)$ which was assumed to behave as a power law at each temperature level (Fig. 2.5). That is

$$C_{11}(t) = At^n \tag{2.32}$$

where n is the power law exponent, which was negative because $C_{11}(t)$ was a monotonically decreasing function.

If we introduce the complex modulus, $C_{11}^*(i\omega)$ as

$$C_{11}^*(i\omega) = \tilde{C}_{11}(s)\Big|_{s=i\omega} = C_{11}'(\omega) + iC_{11}''(\omega), \tag{2.33}$$

then, the loss tangent is defined as

$$\frac{C''_{11}}{C'_{11}} = \tan\left(-\frac{\pi}{2}n\right). \tag{2.34}$$

This procedure resulted in the loss tangent data shown in Figure 2.12. Since the maximum loss tangent corresponds to the glass transition temperature, it was 23.5°C for the primer being considered in this study.

The linear viscoelastic functions, $E(t)$ and $\nu(t)$ were obtained through the interconversion procedures described above. The four linear viscoelastic functions, $K(t)$, $\mu(t)$, $E(t)$ and $\nu(t)$ are shown in Figure 2.13 and Prony series expressions for $E(t)$ and $\nu(t)$ are given in Table 1. The viscoelastic behavior of $E(t)$, $\mu(t)$ and $\nu(t)$ occurred over 13 decades in time. Surprisingly, the bulk relaxation modulus varied over the same number of decades. This has also been recently noted by Deng and Knauss (1997), Sane and Knauss (2001), and Arzoumanidis and Liechti (2003). Previous conceptions of the bulk modulus were that it varies over fewer relaxation times than shear. These differences may be due to the particular material being considered, particularly if it is multiphase material. They may also be due to the fact that it can be difficult to measure the bulk modulus over a wide range of temperatures.

2.3.2 *Bulk Creep Experiments*

Bulk creep experiments were performed at various temperature levels in order to check the validity of the bulk longitudinal relaxation experiments. The bulk creep compliance, $B(t)$ was determined from 14.4°C to 53.7°C. Figure 2.14 shows the data prior to and following horizontal shifting. The extension of the gage length allowed very low pressure levels (676 to 276 kPa) to be used. This resulted in dilatation values that were always less than 1.0x10^{-4} m^3/m^3, thereby ensuring linearity. Temperature levels higher than 53.7°C could not be considered because of leakage problems. Even though the temperature range was quite limited and the rubbery state was not achieved, variations in the bulk creep compliance occurred over six decades.

The master curve of $B(t)$ was compared (Fig. 2.15) with the deduced values that were obtained from the bulk longitudinal relaxation experiments. Note that the directly measured bulk creep compliance did not cover the full range. However, agreement between two functions was quite good over the range where the creep compliance could be measured directly. This validated the procedures that were developed to extract the bulk and shear relaxation moduli from the confined cylinder experiments.

2.3.3 *Thermal and Hygral Expansion*

The thermal expansion experiments were conducted from 29.0 to 49.3°C. The results are presented in Figure 2.16, where two different slopes can be observed. The discontinuity in slope occurred at about 39°C, which is 15°C higher than the value of glass transition that was determined using mechanical experiments. The range of temperatures used in these experiments was relatively limited and meant to correspond to the anticipated operating temperatures of this material. Differential scanning calorimetry data obtained over 200°C temperature range were quite nonlinear in 29.0 to 49.3°C temperature range. So, no matter whether 39.6°C is the glass transition temperature or not, the thermal expansion curve presented in Figure 2.16 was used in the nonlinear analysis. The thermal expansion data was fit to the bilinear function:

$$f_T(T) = \alpha_{v1}\Delta T + (\alpha_{v2} - \alpha_{v1})\Delta T \cdot H(T - T_B) \tag{2.35}$$

where $\alpha_{v1} =$ 6.8x10^{-5} and $\alpha_{v2} =$ 17.1x10^{-5} (m/m/°C) were the slopes and $T_B =$ 39.6°C.

The hygral expansion tests were performed at a fixed temperature of 40.6°C and at various humidity levels. The hygral expansion is shown in Figure 2.17. The data was fit to the form:

$$f_c(c) = \beta_{v2}\Delta c^2 + \beta_{v1}\Delta c + \beta_{v0}, \tag{2.36}$$

where β_{v2} = 1.33x10^{-6} (m/m/%RH^2), β_{v1} = -7.04x10^{-5} (m/m/%RH) and β_{v0} = 6.91x10^{-4}. The maximum hygral strain was about 0.6% over the range of humidity levels considered here. This was more than double the thermal strain that was observed in thermal expansion experiments. In fact, it would take temperature change of about 50°C to achieve similar levels of expansion. The coefficients listed above were used in the shift factor for nonlinear viscoelasticity.

2.4 Conclusions

Bulk longitudinal relaxation experiments were performed to determine the two linear viscoelastic functions, $C_{11}(t)$ and $C_{12}(t)$ of the epoxy primer using a single specimen in a confining cylinder. Lamé’s solution for a thick-walled cylinder was used to extract two functions so that the compliance of the confining cylinder could be accounted for. The linear viscoelastic functions, $K(t)$, $\mu(t)$, $E(t)$ and $\nu(t)$ were related to and determined from $C_{11}(t)$ and $C_{12}(t)$ using three-dimensional, linear viscoelastic constitutive equations. The bulk relaxation modulus varied over 13 decades, which is considerably larger than is commonly believed.

Bulk creep experiments were performed to obtain $B(t)$, which was compared with the bulk relaxation response that was deduced from the bulk longitudinal relaxation experiments. Good agreement was obtained, thereby validating the confining cylinder concept.

The hygrothermal expansion of the primer was also considered. Both the thermal and hygral responses were nonlinear. The parameters that characterized these responses were extracted and will be used in nonlinear viscoelastic models that follow.

3. Nonlinear Viscoelastic Behavior

A series of experiments and analyses were conducted in order to characterize the nonlinear behavior of the epoxy primer. These efforts are described below.

3.1 Experiments

The experiments that are described here are the ones that were needed in order to characterize material response beyond the linear viscoelastic range. The choice of experiments was dictated by the nonlinear viscoelastic models that were considered. These included napkin ring and uniaxial tension experiments under ramp loading over a range of temperatures and humidity levels.

3.1.1 *Napkin Ring Torsion*

The napkin ring specimens were machined from a solid cylindrical blank, which had been molded to a 2.41-cm diameter. The napkin ring specimen was 7.5 mm long and had a wall-thickness of 1.2 mm. A torsion testing device was designed and constructed for applying torsion to the napkin ring specimen (Fig. 3.1). A babbitted pillow block bearing was used in order to ensure rotational and axial freedom while minimizing radial play. This arrangement ensured that the axial load was zero. Proper mounting of the holder and bearing was maintained by making use of an alignment shaft that was then replaced by the gripping shafts. The shaft end which was glued to the specimens, was stepped down to the outer diameter of the specimen to provide specimen alignment. The specimen was glued with a cyanoacrylate glue to the stainless steel gripping shafts, whose surfaces were roughened for optimum bonding strength.

The shaft on the left (Fig. 3.1) was fixed while the other was rotated at three different shear strain rates as the loading arm was pushed down by the actuator of a servohydraulic, uniaxial testing machine. A 445-N load cell was placed between the end of the loading arm and the actuator to measure the load, which was then converted to the corresponding torque. All the shear experiments were conducted at 23.5°C and 35% RH.

The fully automated, real-time video tracking technique described earlier was used to measure the rotation of the shaft. The rotation of two perpendicular lines that intersected at the center of the outer end of the rotating shaft was monitored using an IMAQ angle measurement scheme. The friction between the shaft and the bearing was measured beforehand and subtracted from the total torque even though its magnitude was always less than 1% of full scale. The measurements of the load, actuator displacement and angle of twist were recorded with a personal computer and a 16-bit data acquisition board.

3.1.2 *Uniaxial Tension*

Uniaxial tensile testing was performed on dog-bone tensile specimens with gage sections that were nominally 5.08 cm long by 2.0 mm wide and 0.5 mm thick (Fig. 3.2). The specimens were stamped out using a special punch. The small thickness was required in order to minimize saturation times which were estimated using Fickian diffusion. Uniaxial tensile tests were performed at 3 different grip displacement rates, 4 different temperature levels and 4 relative humidity levels.

Because of the extremely small width and thickness of the specimen, a conventional extensometer could not be used. Instead, a lightweight extensometer was designed to minimize the effect of its weight on the material response. The extensometer consists of a modified paper clip and a stainless steel leg with a thickness of 0.15 mm. It weighed 0.3 g with a gage length of 3.56 cm and the leg was clamped to the specimen by the clip. A dot, which was partially covered by the extensometer leg before loading, was marked on the specimen. As the loading increased, the rest of the dot appeared from behind the extensometer leg and was monitored by the telemicroscope. Its length change was recorded using the same real-time video tracking technique that was used for the bulk creep compliance measurements. A calibration between the actuator displacement and the local strain measurement was established at the two lower displacement rates. The same calibration was then applied to the highest displacement rate, which was too fast for the temporal resolution of the video tracking system. Although this calibration did not change much (less than 10%), it was repeated for all temperatures and humidity levels. The specimen was glued to the grip and a 45-N load cell was used to measure the load. All specimens failed in the gage section.

The uniaxial tension experiments were conducted at temperature levels from 23.5 to 48.9°C. The relative humidity levels ranged from 35 to 95% RH. The minimum period required to fully saturate the specimen at each humidity level was 25 hours based on Fickian diffusion data (Roy, 2003). An environmental chamber maintained the temperature and humidity levels to within 1°C and 2 to 5% RH at high and low humidity levels, respectively. The load, machine displacement and local strain measurements were acquired with a 16-bit data acquisition board in a personal computer, which was also used to record the data.

3.2 Analysis

The distortion modified free volume model (Popelar, Liechti, 1997, 2003) was used and further developed to include the effect of high humidity in conjunction with Schapery's (1969b) model, which was extended to three dimensions. The modified free volume model uses free volume as a unifying parameter to represent various sources of nonlinearity such as temperature, humidity and stress or strain. Some needed linear viscoelasticity equations are reviewed and extended to nonlinear viscoelasticity.

In three dimensions for general loadings, linear viscoelastic constitutive equations can be divided into dilatational and deviatoric components,

$$s_{ij}(t) = \int_0^t 2\mu(t' - \tau') \frac{\partial e_{ij}(\tau)}{\partial \tau} d\tau$$

and (3.1)

$$\sigma_{kk}(t) = \int_0^t 3K(t' - \tau') \frac{\partial \theta(\tau)}{\partial \tau} d\tau,$$

where s_{ij} and e_{ij} are the stress and strain deviators, respectively and $\theta \equiv \varepsilon_{kk}$ is the dilatation. The temperature and moisture reduced time in the kernel in Equation 3.1 takes the form:

$$t' - \tau' = \int_\tau^t \frac{1}{a\left[T(\xi), c(\xi)\right]} d\xi, \tag{3.2}$$

where a is the hygrothermal shift factor and c is the solvent concentration.

3.2.1 *Schapery's Model*

Schapery's one-dimensional representation (1969b) for nonlinear viscoelasticity was extended to three dimensions by Lai and Bakker (1996) for the strain in terms of stress to

$$\begin{aligned} \varepsilon_{ij}(t) &= \frac{1}{2} J_0 g_0 s_{ij}(t) + \frac{1}{2} g_1 \int_0^t \Delta J(t' - \tau') \frac{d(g_2 s_{ij})}{d\tau} d\tau \\ &\quad + \frac{1}{9} B_0 g_0 \delta_{ij} \sigma_{kk}(t) + \frac{1}{9} \delta_{ij} g_1 \int_0^t \Delta B(t' - \tau') \frac{d(g_2 \sigma_{kk})}{d\tau} d\tau \end{aligned} \tag{3.3}$$

where the material functions, g_0, g_1, and g_2 were taken to be the same for distortional and dilatational components so that $g_0 = g_0(\sigma_{kk})$, $g_1 = g_1(\hat{\sigma})$, $g_2 = g_2(\hat{\sigma})$ and $a_\sigma = a_\sigma(\sigma_{kk})$. The quantity $\hat{\sigma} = \sqrt{3 s_{ij} s_{ij} / 2}$ is the von Mises effective stress and the shear and bulk creep compliances are expressed in terms of their glassy and time-dependent components through $J(t) = J_0 + \Delta J(t)$ and

$B(t) = B_0 + \Delta B(t)$. In this model, time is accelerated by the hydrostatic stress, so that

$$t' - \tau' = \int_{\tau}^{t} \frac{1}{a_{\sigma}[\sigma_{kk}(\xi)]} d\xi . \tag{3.4}$$

The experiments that were used here to develop a model of nonlinear viscoelastic behavior were conducted in displacement control. As a result, it is more convenient to express the stress in terms of strain and the following relationships were introduced:

$$s_{ij}(t) = 2g_0^{\mu}\mu_{\infty}e_{ij} + g_1^{\mu}\int_0^t 2\Delta\mu(t'-\tau')\frac{\partial\left[g_2^{\mu}e_{ij}\right]}{\partial\tau}d\tau$$

and (3.5)

$$\sigma_{kk}(t) = 3g_0^{K}K_{\infty}\theta + g_1^{K}\int_0^t 3\Delta K(t'-\tau')\frac{\partial\left[g_2^{K}\theta\right]}{\partial\tau}d\tau.$$

Now, g_0^K, g_1^K, g_2^K, g_0^{μ}, g_1^{μ}, g_2^{μ} and a_{σ} are functions of dilatation and effective strain as sources of nonlinearity. Note that the nonlinearity could be different in distortion and dilatation. The shear and bulk relaxation moduli are expressed as $\mu(t) = \mu_{\infty} + \Delta\mu(t)$ and $K(t) = K_{\infty} + \Delta K(t)$, respectively. The kernel in the constitutive relations is given by

$$t' - \tau' = \int_{\tau}^{t} \frac{1}{a[T(\xi), c(\xi), \varepsilon_{eff}(\xi), \theta(\xi)]} d\xi , \tag{3.6}$$

where the shift factor was taken to depend on distortional as well as dilatational strains in keeping with the developments of Popelar and Liechti (1997, 2003).

In Equation 3.3 and previous models, the effects of temperature and solvent concentration were introduced through the free volume and, consequently, the shift factor. For the epoxy primer being considered here, the nonlinear effects associated with higher temperatures and levels of solvent concentration required additional modification. This was introduced by making g_0, g_1 and g_2

functions of temperature and solvent concentration in addition to distortional and dilatational strains. Thus,

$$
\begin{aligned}
&g_0 = g_0(T, c, \varepsilon_{eff}, \theta) \\
&g_1 = g_1(T, c, \varepsilon_{eff}, \theta) \qquad (3.7) \\
&g_2 = g_2(T, c, \varepsilon_{eff}, \theta).
\end{aligned}
$$

3.2.2 *Modified Free Volume Model*

The modified free volume model (Popelar and Liechti, 1997, 2003) is a special case of the three-dimensional version of Schapery's model (1969b). All the sources of nonlinearity are integrated through a single parameter, the so called free volume. The free volume accounts for the effects of temperature, solvent concentration and dilatational and distortional strains on the shift factor.

Free volume was first related to the time-temperature shift factor by Doolittle (1951). Knauss and Emri (1981) and Knauss and Kenner (1980) recognized that the free volume was also effected by the dilatational strain and solvent concentration, respectively. Thus, dilatation can also accelerate time through the shift factor. In order to include the effect of shear-dominated loadings, Popelar and Liechti (1997, 2003) introduced the modified free volume model. It was postulated that the distortional strain also contributed to the free volume. In this model, the kernel becomes

$$t' - \tau' = \int_{\tau}^{t} \frac{1}{a[T(\xi), c(\xi), \varepsilon_{eff}(\xi), \theta(\xi)]} d\xi . \qquad (3.8)$$

The shift factor shown in Equation 3.8 has had (Popelar and Liechti, 1997) the form.

$$\log a = -\frac{B_d}{2.303 f_d}\left(\frac{\alpha_v \Delta T + \beta_v \Delta c + \delta\theta}{f_d + \alpha_v \Delta T + \beta_v \Delta c + \delta\theta}\right) - \frac{B_s}{2.303 f_s}\left(\frac{\varepsilon_{eff}}{f_s + \varepsilon_{eff}}\right). \qquad (3.9)$$

The parameters, B_d and f_d and B_s and f_s are dilatational and distortional parameters, respectively. Both sets of parameters must be calibrated experimentally.

Thus, the constitutive equation (3.5) can be reduced to the modified free volume by taking

$g_0^K = g_1^K = g_2^K = g_0^\mu = g_1^\mu = g_2^\mu = 1$.

For stiffening in the rubbery regime, Popelar and Liechti (1997) introduced a long-time shear modulus that was taken to vary exponentially with strain such that

$$\mu_\infty = \tilde{\mu}_\infty e^{\left(\varepsilon_{eff} / \varepsilon_0\right)}, \tag{3.10}$$

which can be accounted for by g_0^μ with all the others taken as unity. The parameter, $\tilde{\mu}_\infty$ is the long-time shear modulus from linear viscoelasticity and ε_0 is a free parameter. Park and Liechti (2003) found that a urethane adhesive displayed rate-dependence at large strains. This was accounted for by introducing a rate-dependent shear long-time modulus

$$\mu_\infty = \tilde{\mu}_\infty \log\left(\frac{\dot{\varepsilon}_{eff}}{\dot{\varepsilon}_0}\right)^n, \tag{3.11}$$

where $\dot{\varepsilon}_0$ and n are free parameters. This indicates that g_0^μ can be a function of the effective strain rate.

3.2.3 *Hybrid Model*

As will be seen in results section, the modified free volume model worked quite well up to 48.9°C and 65% RH. In essence, this means that nonlinear parameters in Schapery's model were all unity. Under more severe conditions, it was necessary to combine the nonlinearities introduced by Schapery's model with those of the modified free volume approach. This combination is designated the hybrid model.

The shift factor shown in Equation 3.9 was unable to capture thermal and hygral effects at high temperature and humidity levels. The thermal dilatation experiments indicated that the thermal strain was a bilinear function of the temperature (Fig. 16). This function (Eqn. 2.35) replaced the $\alpha_v \Delta T$ term in Equation 3.9. For hygral effects, the term $\beta_v \Delta c$ was replaced by $\beta\left(\beta_{v2}\Delta c^2 + \beta_{v1}\Delta c + \beta_{v0}\right)$, reflecting the hygral dilatation response (Fig.17). The shift factor therefore became

$$\log a = -\frac{B_d}{2.303 f_d}\left(\frac{\delta\theta + f_T(T) + \beta f_C(c)}{f_d + \delta\theta + f_T(T) + \beta f_C(c)}\right) - \frac{B_s}{2.303 f_s}\left(\frac{\varepsilon_{eff}}{f_s + \varepsilon_{eff}}\right). \tag{3.12}$$

The factor β was introduced to scale hygral effects as will be seen in the results.

For relative humidity levels below 65% RH, the quantities $g_i^\mu = g_i^K = 1$. Above this level, g_2^μ and g_2^K remained the same while $g_0^\mu = g_0^K = g_1^\mu = g_1^K = g$, where

$$g = H[c-65]\{1 - 0.0132(c-65)\} \tag{3.13}$$

and

$$\begin{aligned} s_{ij}(t) &= g\int_0^t 2\mu(t'-\tau')\frac{\partial e_{ij}}{\partial \tau}d\tau \\ \sigma_{kk}(t) &= g\int_0^t 3K(t'-\tau')\frac{\partial \theta}{\partial \tau}d\tau. \end{aligned} \tag{3.14}$$

3.3 Results and Discussion

The nonlinear viscoelastic behavior of the epoxy primer was characterized using the models presented above. This adhesive exhibited nonlinear behavior under the shear and tension experiments that were conducted over a range of temperature and humidity levels.

3.3.1 *Shear*

The data was obtained at three different shear strain rates from 1.9x10^{-5}, 1.9x10^{-4} and 1.9x10^{-3} rad/s at 23.5°C and 35% RH. At the two lower strain rates, failure occurred in the gage section while premature failure occurred at the grips at the highest strain rate. Apparently, the bond between the steel grips and the adhesive could not withstand the higher load levels that occurred at the highest strain rate.

Torsion gave rise to a highly nonlinear response in the epoxy (Fig. 3.3). The slope of the response was initially stiff and then decreased. The maximum was then followed by a load drop and dramatic softening behavior. After the load drop, the stress level remained almost constant and then some gradual stiffening behavior was observed prior to failure. Very strong viscoelastic effects were observed between each prescribed strain rate because the testing temperature was close to the glass transition temperature.

Napkin ring torsion tests were used to calibrate the parameters for the model presented in Equation 3.12. Under pure shear without any change in temperature and humidity, the stress and strain are related through

$$\sigma_{12}(t) = \int_0^t 2\mu(t' - \tau')\frac{\partial \varepsilon_{12}}{\partial \tau}d\tau$$

and (3.15)

$$\sigma_{kk}(t) = \int_0^t 3K(t' - \tau')\frac{\partial \theta}{\partial \tau}d\tau = 0.$$

where $t' - \tau' = \int_\tau^t \frac{d\xi}{a[\varepsilon_{eff}(\xi)]}$ and Equation 3.12 reduces to

$$\log a = -\frac{B_s}{2.303 f_s}\left(\frac{\varepsilon_{eff}}{f_s + \varepsilon_{eff}}\right). \tag{3.16}$$

Various sets of B_s and f_s were checked until the optimum match was obtained between the model and the data at 1.9x10^{-4} rad/s (Fig. 3.3).

A parametric study of the effect of B_s and f_s indicated that f_s was very influential and had to be close to the shear strain level where the load drop occurred. Once this value of f_s was chosen, various sets of values for B_s and f_s were tested to see if they captured the plateau and gradual stiffening behavior that followed the load drop. It was necessary to vary f_s slightly (±0.05 rad) to achieve the best fit. This set of distortional parameters (B_s=2.2 and f_s = 0.105) produced very good predictions of the data at the other shear strain rates.

The resulting time shift factor is shown as a function of shear strain in Figure 3.3. The rapid change in the time shift factor in the initial portion of the stress-strain curve caused such an acceleration in the stress relaxation that it created the load drop. As the rate of change in the time shift factor decreased, the constant-strain rate applied to the specimen balanced the relaxation so as to create the plateau region, which was eventually followed by the gradual stiffening. The magnitude of the time shift factor at large shear strains corresponded to a temperature of 65^{o}C in the thermal shifting factor. The constant slope of the stiffening behavior at large strains indicates that the rubbery state had been reached.

3.3.2 *Tension*

After the distortional parameters had been determined in torsion, the dilatational parameters had to be found by applying a combination of distortion and dilatation which arise in uniaxial tension. As a result, the shift factor in the absence of changes in temperature and humidity now becomes

$$\log a = -\frac{B_d}{2.303 f_d}\left(\frac{\delta\theta}{f_d + \delta\theta}\right) - \frac{B_s}{2.303 f_s}\left(\frac{\varepsilon_{eff}}{f_s + \varepsilon_{eff}}\right) \tag{3.17}$$

The axial stress can be obtained from

$$\begin{aligned}\sigma_{11}(t) &= \int_0^t K(t'-\tau')\frac{\partial\varepsilon_{11}}{\partial\tau}d\tau + 2\int_0^t K(t'-\tau')\frac{\partial\varepsilon_{22}}{\partial\tau}d\tau \\ &+\frac{4}{3}\int_0^t \mu(t'-\tau')\frac{\partial\varepsilon_{11}}{\partial\tau}d\tau - \frac{4}{3}\int_0^t \mu(t'-\tau')\frac{\partial\varepsilon_{22}}{\partial\tau}d\tau.\end{aligned} \tag{3.18}$$

However, notice that the transverse strain which appears in Equations 3.17 and 3.18 was not measured. Consequently, it would have to be determined from the condition that the transverse stress was zero. That is

$$\begin{aligned}\sigma_{22}(t) &= \int_0^t K(t'-\tau')\frac{\partial\varepsilon_{11}}{\partial\tau}d\tau + 2\int_0^t K(t'-\tau')\frac{\partial\varepsilon_{22}}{\partial\tau}d\tau \\ &-\frac{2}{3}\int_0^t \mu(t'-\tau')\frac{\partial\varepsilon_{11}}{\partial\tau}d\tau + \frac{2}{3}\int_0^t \mu(t'-\tau')\frac{\partial\varepsilon_{22}}{\partial\tau}d\tau = 0.\end{aligned} \tag{3.19}$$

The determination of the transverse strain in this way usually requires an iterative method (Popelar and Liechti, 2003). However, since Poisson's ratio was already known, E(t) and $\nu(t)$ were used, instead of K(t) and $\mu(t)$. Thus,

$$\begin{aligned}&\sigma_{11}(t) = \int_0^t E(t'-\tau')\frac{\partial\varepsilon_{11}}{\partial\tau}d\tau \\ &\text{and} \\ &\varepsilon_{22}(t) = \int_0^t \nu(t'-\tau')\frac{\partial\varepsilon_{11}}{\partial\tau}d\tau.\end{aligned} \tag{3.20}$$

This formulation allowed ε_{22} to be determined directly without iteration. As a matter of interest, the values of ε_{22} determined from the two approaches were compared and a very good match was obtained.

The data from the uniaxial tension experiments at 23.5°C and 35% RH is shown in Figure 3.4a. A peak stress was observed at all strain rates. It was followed by a load drop and plateau at the lowest strain rate. Premature failure in the gage section at the higher strain rate precluded any load drop and plateau region.

The data was compared (Fig. 3.4a) with predictions using Equation 3.20. The data at the lowest strain rate was used to extract the dilatational parameters which were $B_d = 29$, $f_d = 0.1$ and $\delta = 0.08$. Note that in the past (Knauss and Emri, 1981, 1987; Popelar and Liechti, 1997, 2003; Arzoumanidis and Liechti, 2003), the parameter δ was always taken to be unity. This was acceptable because the coefficient of thermal expansion was not measured. This flexibility was lost in this study because thermal expansion was measured. Good agreement between measurements and predictions at the higher strain rates was obtained.

3.3.3 *Thermal Effect*

The results from the uniaxial tension experiments at four strain rates and temperatures at ambient humidity are shown in Figure 3.4. As the temperature increased, the load drop decreased and the plateau region shortened. At lower temperatures, where the material would be more brittle, the specimens failed at relatively small strains. At high temperatures, strain levels greater than 40% were realized. Rubbery behavior was seen at higher temperature levels and small strain rates.

The hybrid model as calibrated thus far has been shown to account for the effect of strain rates on the behavior of the material under ambient conditions. Equation 3.12 suggests that the hybrid model should be able to account for higher temperature and humidity levels. It can be seen that thermal effects should be accounted for directly by making use of the thermal expansion coefficients given earlier (Eqn. 2.35). The parameter β (Eqn. 3.12), which scales the hygral expansion coefficients has yet to be determined.

The validity of the thermal modeling ($\beta = 0$) was examined at 32.2, 40.6 and 48.9°C. The results are shown in Figure 3.4. It can be seen that the predictions fit the data very well without any changes in parameters with the possible exception of 48.9°C where the model response was consistently stiffer at large strains. It is possible that diffuse damage was occurring in the experiments that was not accounted for in the model. This might also explain why no difference was observed at lower temperatures, where the strain to failure was much smaller.

3.3.4 *Hygral Effect*

In considering how to characterize the effect of solvent on the nonlinear behavior of the primer, one possibility would be to set $\beta = 1$ in Equation 3.12. This would give equal weight to the effect of thermal and hygral expansion on the free volume. The results of this possibility are shown in Figure 3.5a. It can be seen that the acceleration of the time scale of the material was too great. The rubbery response in the model manifested itself much earlier than was indicated by experiments. This implied that the effect of actual hygral expansion on the free volume was taken too high and that some scaling of β was required.

A parametric study of the effect of β was conducted. The value $\beta = 0.2$ provided (Fig. 3.5b) good agreement at 65% RH. However, it was not possible to obtain good fits at 75 and 95% RH with the same value of β. In fact it was not possible to find one value of β that resulted in good matches between predictions and measurements at all humidity levels. The reason for preferring $\beta = 0.2$ was that it reflected the limit of what could be accomplished by horizontal shifting. Any further accommodation of the data required vertical shifting, which is part of Schapery's approach.

A similar need for vertical shifting in the presence of high humidity levels was observed in experiments on fully saturated urethane adhesive that was subjected to uniaxial tension (Park and Liechti, 2003). For urethane at 60°C, the modified free volume model consistently over predicted the data at all four strain rates. Again, the acceleration in material clock was not able to fully capture the material response. For both the epoxy primer and urethane at high humidity levels, vertical shifting was required to reflect the added softening of the material at high humidity levels.

As indicated in the initial presentation of the hybrid model, it essentially provides horizontal and vertical shifting to account for the presence of solvent. The formulation given in Equation 3.14 was in terms of distortional and dilatational components. For fitting purposes, it was more convenient to work in terms of tensile relaxation and Poisson's ratio.

$$\sigma_{11}(t) = g\int_0^t E(t'-\tau')\frac{\partial\varepsilon_{11}}{\partial\tau}d\tau$$

and (3.21)

$$\varepsilon_{22}(t) = \int_0^t \nu(t'-\tau')\frac{\partial\varepsilon_{11}}{\partial\tau}d\tau.$$

Note that the g function in first equation is the same as the one that appears in Equation 3.14 and that it did not appear in the second equation. This is entirely consistent with the formulation in Equation 3.14.

In Figure 3.5b, we saw that $\beta = 0.2$ and $g = 1$ worked well for 65% RH, but higher humidity levels required some vertical shifting, due to stronger nonlinearity. This was accomplished by noting the degree of shifting that was required at each humidity level. As a result,

$$g = H[c-65]\{1-0.0132(c-65)\}. \tag{3.22}$$

It can be seen that this humidity dependent vertical shifting factor provided very good agreement with the data. Thus, we have, for the first time, a nonlinear viscoelastic model that accounts for large strains, temperature and humidity.

3.4 Conclusions

The nonlinear viscoelastic behavior of the epoxy primer was determined through a series of experiments that involved two different stress states at various temperature and humidity levels. Napkin ring torsion and uniaxial tension experiments were conducted at three different strain rates. Four temperature and humidity levels were also considered in the tension experiments. Each of these experiments was used to progressively calibrate a hybrid model that introduced the nonlinear behavior through a horizontal shift factor that depended on dilatational and distortional strain, temperature and solvent content and a vertical shift factor that was required to fully account for the effect of high levels of solvent.

4. Nonlinear Viscoelastic Interfacial Fracture Mechanics

Wedge tests were conducted in order to characterize the interfacial fracture behavior between the primer and concrete. A pseudo stress model (Schapery, 1984) was calibrated as a nonlinear viscoelastic model that is particularly suitable for viscoelastic fracture analysis. The time-dependent generalized J integral was used to compute the fracture energy under steady state crack growth at various temperature and moisture levels.

4.1 Experiments

Driven wedge testing was performed on specimens consisting of concrete coated with a thick layer of epoxy primer (Fig. 4.1). The concrete substrates were fabricated with a mixing ratio of 156, 390, 1066 and 710 kg of water, cement, pea gravel and sand per cubic meter, respectively. The maximum size of aggregates was 0.952 cm. The concrete was placed into a 15.3 cm-long by 6.87 cm-wide mold which had a depth of 3.82 cm. Concrete cylinders with a diameter of 10.2 cm and a height of 20.3 cm were fabricated at the same time for use as compression specimens. The concrete specimens were removed from the molds and placed in a humidity chamber for 14 days.

MBrace^{TM} composite strengthening system specifications (1998) were followed for the surface preparation of the concrete bond surface. Sand blasting was used to remove mortar until the sand aggregates appeared. An air blower was then used to remove dust from the concrete surface. The resulting concrete surface did not require any grinding.

The epoxy primer resin and hardener were mixed with a 10:3 ratio by weight and applied to the concrete within the 45 minute working time. After the epoxy primer was cured under ambient condition for 7 days, the specimens were post-cured in an oven at 91°C for 36 hours in order to ensure that diffusion kinetics were Fickian. It had been found that the primer lost weight when it was not post-cured in this way.

An initial crack was created by applying a ramp loading/uploading cycle with a wedge velocity of 0.254 m/sec. This relatively high loading rate produced very sharp initial cracks. For steady state crack growth, the wedge was driven past the initial crack front location, at which time the crack growth became steady. The crack length a was measured in real time using automated digital image analysis scheme (National Instruments IMAQ with LabView). In addition, images were acquired and recorded for subsequent determination of the wedge displacement, h. In order to minimize a specimen-to-specimen variation, single concrete specimen was used. For high temperature and humidity experiments, initial cracks were created at room temperature and the specimens were then heated in an environmental chamber. The rest of the experimental procedures were the same.

4.2 Pseudo Stress Model

Schapery (1984, 1986) developed correspondence principles which do not require Laplace transformation, but, instead, require the use of special viscoelastic constitutive models known as the pseudo strain and pseudo stress models. These were developed specially for nonlinear viscoelastic materials. In this work, the pseudo stress model was calibrated using the uniaxial tension data at various temperature and humidity levels that was presented in Chapter 3.

4.2.1 *Correspondence Principle*

Schapery established three correspondence principles between nonlinear elastic boundary value problems and nonlinear viscoelastic boundary value problems. The so-called reference solutions σ_{ij}^R, ε_{ij}^R and u_i^R were defined to satisfy the elastic field equations of equilibrium,

$$\frac{\partial \sigma_{ij}^{R}}{\partial x_j} + F_i^R = 0\,, \tag{4.1}$$

and strain-displacement,

$$\varepsilon_{ij}^{R} = \frac{1}{2}\left(\frac{\partial u_i^R}{\partial x_j} + \frac{\partial u_j^R}{\partial x_i}\right). \tag{4.2}$$

The surface tractions are related to the stress components through

$$T_i^R = \sigma_{ij}^R n_j \quad \text{on } S_T\,. \tag{4.3}$$

Elsewhere, displacements are prescribed on S_U .

$$U_i^R = U_i^R(x_j, t)\,. \tag{4.4}$$

The linear or nonlinear elastic constitutive equations are

$$\varepsilon_{ij}^{R} = \varepsilon_{ij}^{e}(\sigma_{kl}^{R}, x_m, t). \tag{4.5}$$

Similarly, the solutions σ_{ij} , ε_{ij} and u_i to the nonlinear viscoelastic boundary problem satisfy

$$\frac{\partial \sigma_{ij}}{\partial x_j} + F_i = 0\,, \tag{4.6}$$

and

$$\varepsilon_{ij} = \frac{1}{2}\left(\frac{\partial u_i}{\partial x_j} + \frac{\partial u_j}{\partial x_i}\right). \tag{4.7}$$

The surface tractions are related to the stress components through

$$T_i = \sigma_{ij} n_j \quad \text{on } S_T\,. \tag{4.8}$$

Elsewhere, displacements are prescribed on S_U .

$$U_i = U_i(x_j, t) \tag{4.9}$$

Three correspondence principles were introduced by Schapery (1984), depending upon whether boundary surfaces S_T and S_U varied with time. The first correspondence principle applies in situations where both the pseudo strain and pseudo stress are used at the same time which requires that the boundary surfaces cannot vary with time. When a crack is growing and $dS_T / dt \geq 0$, the second correspondence principle should be used in conjunction with a pseudo strain model. In this case, the physical and reference tractions are the same, i.e.

$$T_i^R = T_i \qquad \text{on } S_T \text{ .} \tag{4.10}$$

The third correspondence principle applies to crack healing or $dS_T / dt \leq 0$ and requires the use of the pseudo stress. In this case, the elastic and viscoelastic displacements are the same, which requires that the displacement boundary condition in the physical problem should be same as that of the reference elastic boundary condition:

$$u_i^R = U_i \qquad \text{on } S_{U.} \tag{4.11}$$

There are some situations where the third correspondence principle can be applied to steady state crack growth. In this study, we take advantage of this special case.

4.2.2 *Pseudo Stress Model*

As indicated above, the pseudo stress model is required for the application of Schapery's third correspondence principle. In this model, the reference elastic and viscoelastic boundary value problems are related through a pseudo (reference) stress σ_{ij}^R that is defined through

$$\sigma_{ij} = \frac{1}{E_R} \int_0^t E(t-\tau) \frac{\partial \sigma_{ij}^R}{\partial \tau} d\tau \text{ ,} \tag{4.12}$$

where E_R is a reference modulus. In this case, the viscoelastic strains and displacements are the same as the reference elastic strains and displacements, i.e.

$$\varepsilon_{ij} = \varepsilon_{ij}^R \tag{4.13}$$

and

$$u_i = u_i^R . \qquad (4.14)$$

Hygrothermal effects enter the pseudo stress through the reduced time in the kernel of the relaxation function, so that

$$\sigma_{ij} = \frac{1}{E_R(T,c)} \int_0^t E(t' - \tau') \frac{\partial \sigma_{ij}^R}{\partial \tau} d\tau . \qquad (4.15)$$

where the kernel follows the standard linear viscoelastic thermal and hygral shifting and E_R is a function of temperature and solvent concentration.

4.2.3 *Linear Elasticity*

Linear elasticity can be used in conjunction with the pseudo stress model as the reference elastic boundary value problem. Linear elasticity allows the generalized J integral to be computed. However, unless a traction-separation law is specified for the failure zone, the work input and the fracture energy cannot be determined. As a result, the generalized J integral with linear elasticity was computed and only used in order to provide a reference for the nonlinear analysis that follows.

Linear elastic constitutive equations can be expressed as

$$E\varepsilon_{ij} = \left(1+\nu\right)\sigma_{ij} - \nu\sigma_{kk}\delta_{ij} \qquad (4.16)$$

where E and ν are Young's modulus and Poisson's ratio.

When Young's modulus and Poisson's ratio become the reference modulus and Poisson's ratio in the reference boundary value problem, it may be expressed as

$$E_R\varepsilon_{ij} = \left(1+\nu_R\right)\sigma_{ij} - \nu_R\sigma_{kk}\delta_{ij} \qquad (4.17)$$

where E_R and ν_R need to be calibrated at different temperature and humidity levels, respectively.

If constant strain-rate tension data at one rate were used to calibrate the reference modulus and Poisson's ratio, the corresponding J integral would be the same as the strain energy release rate. However, this is not useful for viscoelastic deformation because it cannot account for rate effects.

4.2.4 *Nonlinear Elasticity*

Deformation plasticity was chosen as a nonlinear elastic constitutive model for the reference elastic boundary value problem. Deformation theory in three dimensions can be expressed as

$$E\varepsilon_{ij} = (1+\nu)s_{ij} + (1-2\nu)\frac{\sigma_{kk}}{3}\delta_{ij} + \frac{3}{2}\alpha\left(\frac{\sigma_{eff}}{\sigma^{o}}\right)^{n-1} s_{ij}\,, \tag{4.18}$$

where α , σ^{o} and n are deformation plasticity parameters.

When deformation plasticity is used with the pseudo stress model at various temperature and humidity levels, it may be expressed as

$$E_R\varepsilon_{ij} = (1+\nu_R)s_{ij} + (1-2\nu_R)\frac{\sigma_{kk}}{3}\delta_{ij} + \frac{3}{2}\alpha\left(\frac{\sigma_{eff}}{\sigma^{o}}\right)^{n-1} s_{ij}\,, \tag{4.19}$$

where E_R, ν_R, α , σ^{o} and n are then dependent on the temperature and humidity levels.

4.2.5 *Results and Discussion*

The calibration of the pseudo stress model was first performed using the uniaxial ramp tension data at 23.5°C (Fig. 4.2a). The reference modulus and Poisson’s ratio were taken to be 2.46 GPa and 0.406, respectively. These were actually the relaxation values at 50 sec, which was chosen because it fell in the middle of the fastest ramp loading experiment. Only the nonlinear viscoelastic pseudo stress model was calibrated because neglecting the nonlinear parameters of nonlinear elasticity leads to the linear viscoelastic pseudo stress model. The initially rising region in the stress-strain curve corresponds to the linear viscoelastic pseudo stress model.

The pseudo stresses $\sigma_{11}^{R}(t)$ corresponding to the data ($\sigma_{11}(t)$) at each strain rate were determined using

$$\sigma_{11} = \frac{1}{E_R^{23.5}} \int_0^t E(t-\tau) \frac{\partial \sigma_{11}^{R}}{\partial \tau} d\tau . \tag{4.20}$$

The value of σ_{11}^{R} was determined iteratively by making an initial guess and then comparing the corresponding value of $\sigma_{11}(t)$ with the right hand side of Equation 4.20. The guess was updated successively until a good match was obtained. The tolerance was set to 7 kPa.

Once $\sigma_{11}^{R}(t)$ had been found, it was substituted into

$$\varepsilon_{11}(t) = \frac{\sigma_{11}^{R}(t)}{E_R^{23.5}} \left[1 + \alpha \left(\frac{\sigma_{11}^{R}(t)}{\sigma^{o}} \right)^{n-1} \right], \tag{4.21}$$

which is the uniaxial version of Equation 4.19, in order to determine the corresponding uniaxial strain $\varepsilon_{11}(t)$ for various values of α , σ^{o} and n . In calibrating the pseudo stress model, the plateau stress level was preferred to the peak stress level because of the large deformations that occur near crack tips. In addition, using the generalized J integral requires a uniform stress in the crack tip region, thereby greatly simplifying the computation of the fracture energy. Thus, the selected values of α , σ^{o} and n were those that produced a stress-strain curve that matched the measured plateau stress at the lowest strain rate, $\dot{\varepsilon}$ = 0.00015 m/m/s. In order to determine the stress-strain behavior at two higher rates, the same values of α , σ^{o} and n were used with the corresponding pseudo stress.

The calibration of the pseudo stress model at higher temperature levels was performed by taking account of the thermal shifting factor in order to adjust E_R and ν_R. In addition, the values of α , σ^{o} and n had to be reselected based on the data from the experiment at the lowest strain rate at each temperature (Figs.

4.2-3). The only exception to this procedure was at 48.9°C, where the highest strain rate was used because it was the only response that exhibited a plateau.

The WLF thermal shifting factor (Fig. 2.11) was used to determine E_R and ν_R. This adjustment was essential because the linear viscoelastic properties at higher temperatures are quite different. This ensured that the small strain response matched the data at all temperatures and strain rates. The extraction of α, σ^o and n was repeated at 32.2, 40.6 and 48.9°C and the resulting values of these parameters are shown in Table 4.1. It can be seen that E_R decreased with increasing temperature as expected. There was corresponding increase in ν_R. Amongst α, σ^o and n, the biggest effect of temperature was on σ^o. This essentially established the effect of temperature on the yield stress, σ^y, which is also listed and was determined by the 0.2% offset method. The parameter α was kept the same at all temperatures and although the hardening exponent n did change, it was in a range where the hardening is relatively insensitive to n.

The uniaxial tension data at 40.6°C and various humidity levels was used to calibrate the pseudo stress model in terms of humidity. The hygral shifting factor for nonlinear viscoelastic modeling (Eqn. 3.12) was used to determine $E_R(T=40.6^{\mathrm{O}}C,c)$ and $\nu_R(T=40.6^{\mathrm{O}}C,c)$. E_R and ν_R were determined using both horizontal and vertical shifting. The horizontal shifting was based on linear viscoelastic functions, $E(t)$ and $\nu(t)$. The vertical shifting was the same as was used in the hybrid model.

The horizontal shifting for humidity was essentially accomplished using Equation 3.12. However, it was converted to the WLF form

$$\log a_T = \frac{-C_1\left[T-T_M+\beta f_C(c)/\alpha\right]}{\left[C_2+T-T_M+\beta f_C(c)/\alpha\right]} \tag{4.22}$$

for consistency with the temperature effect and convenience.

The vertical shifting was applied to the reference modulus following horizontal shifting. Equation 3.13 was used to determine the vertical shifting factor at high humidity levels. The resulting values of E_R and ν^R are shown in Table 4.2 along with the values of α , σ_O and n , which were determined in the same way as they had been for different temperatures. The results are also shown in Figure 4.4. The plateau levels of the pseudo stress models were chosen so as to provide conservative estimates of the stress-strain behavior.

4.2.6 *Conclusions*

The pseudo stress model was calibrated on the basis of uniaxial tension data at various temperature and humidity levels. A three-dimensional power law was employed as the nonlinear elastic model for the reference elastic problem. The reference modulus and Poisson's ratio were adjusted using linear viscoelastic functions in order to account for temperature effects. Humidity required the use of horizontal and vertical shifting in parallel with the schemes that were used for the hybrid nonlinear viscoelasticity model. Rate effects were captured through the reference modulus and Poisson's ratio.

4.3 Generalized J integral for Viscoelastic Interfacial Cracks

The generalized J integral, designated J_v , was introduced in order to account for nonlinear viscoelastic material surrounding an interfacial crack. The main advantage of J_v was to combine well-established nonlinear elastic fracture mechanics concepts with linear viscoelastic time-dependency to create together a nonlinear viscoelastic fracture analysis. The parameter J_v was proposed as a nonlinear viscoelastic fracture parameter in the same spirit that J integral of Rice (1968) was used as a nonlinear elastic fracture parameter. This greatly reduced the effort required for the determination of the fracture energy because time and nonlinear elasticity effects are separated and the required finite element analyses were just elastic. The results from the nonlinear elastic fracture analysis were converted to nonlinear viscoelastic fracture energy through the pseudo stress model.

4.3.1 *Generalized J integral*

We now introduce a generalized J integral for the analysis of interfacial cracks between nonlinearly viscoelastic media. Since a pseudo stress model was used to represent the behavior of the epoxy primer, the following path independent integral is considered:

$$\mathrm{I} \equiv \int_C \left(\Phi dx_2 - T^R_i \frac{\partial u_i}{\partial x_1} \right) ds = 0 , \tag{4.23}$$

where T_i^R is the pseudo traction and a work potential was defined for each material through

$$\sigma_{ij}^R = \frac{\partial \Phi_1(\varepsilon_{ij}, x_k, t)}{\partial \varepsilon_{ij}} \tag{4.24}$$

and

$$\sigma_{ij}^R = \frac{\partial \Phi_2(\varepsilon_{ij}, x_k, t)}{\partial \varepsilon_{ij}} , \tag{4.25}$$

where the subscripts 1 and 2 designate the material above and below the interface, respectively.

With reference to Figure 4.5, we introduce two contour integrals.

$$J_f \equiv \int_{C_f} \left(\Phi dx_2 - T_i \frac{\partial u_i^R}{\partial x_1} \right) ds \tag{4.26}$$

and

$$J_v \equiv \int_{C_1} \left(\Phi dx_2 - T_i \frac{\partial u_i^R}{\partial x_1} \right) ds , \tag{4.27}$$

where both contours start at location 1 and progress to the end location 2 in a counterclockwise direction.

The condition **I** = 0 leads to

$$J_v = J_f . \tag{4.28}$$

Because the materials 1 and 2 were taken as epoxy and concrete, respectively and the concrete is linearly elastic, the pseudo stress in Equation 4.25 may be replaced by the physical stress. Thus,

$$\sigma_{ij} = \frac{\partial \Phi_2}{\partial \varepsilon_{ij}} . \tag{4.29}$$

The integral J_f can be defined using the relative displacement vectors, Δu_i^{ep} and Δu_i^{co} of epoxy and concrete inside the failure zone (Fig. 4.6) as

$$J_f \equiv \int_0^{\alpha} \left[\sigma_{2i}^R \left(\frac{\partial \Delta u_i^{ep}}{\partial \xi} + \frac{\partial \Delta u_i^{co}}{\partial \xi} \right) \right] d\xi , \tag{4.30}$$

where σ_{2i}^R are the pseudo stress components in the failure zone on $x_2 = 0$. The contribution from Φ in Equation 4.26 was neglected because the failure zone is thin relative to cohesive zone size, α.

Because the compliance of the concrete is much less than that of epoxy, its contribution can be neglected and J_f can be written as

$$J_f = \int_0^{\alpha} \left(\sigma_{2i}^R \frac{\partial \Delta u_i^{ep}}{\partial \xi} \right) d\xi . \tag{4.31}$$

It is assumed that the material in the cohesive zone has been strained to levels that gave rise to the nearly constant stress levels in the pseudo stress model (Figs. 4.2-4). As a result, the $\sigma_{2i}^R \neq \sigma_{2i}^R(\xi)$ and J_f becomes

$$J_f = \int_0^{\alpha} \left(\sigma_{2i}^R \frac{\partial \Delta u_i^{ep}}{\partial \xi} \right) d\xi = \sigma_{2i}^R \int_0^{\alpha} \frac{\partial \Delta u_i^{ep}}{\partial \xi} d\xi = \sigma_{2i}^R \, \Delta u_i^{ep} \Big|_{\alpha} . \tag{4.32}$$

If $J_f = J_{f1} + J_{f2} + J_{f3}$, where $J_{fi} = \sigma_{2i}^R \, \Delta u_i^{ep}\Big|_\alpha$ (no sum), then,

$$\sigma_{2i}^R = \frac{J_{fi}}{\Delta u_i^{ep}\Big|_\alpha} \text{(no sum)}. \tag{4.33}$$

When Equation 4.15 is substituted into Equation 4.33, the actual stress in the cohesive zone becomes

$$\sigma_{2i} = \frac{1}{E_R(T,c)} \int_0^t E(t' - \tau') \frac{\partial \left(J_{fi} / \Delta u_i^{ep}\Big|_\alpha \right)}{\partial \tau} d\tau \quad \text{(no sum)}. \tag{4.34}$$

In order to compute the fracture energy, it is necessary to consider the work input to a material element inside the cohesive zone. Since there is no need to consider time as an independent variable for steady state crack growth, the work input may be expressed as

$$W_f = \int_0^\alpha \sigma_{2i} \frac{\partial \Delta u_i^{ep}}{\partial \xi} d\xi . \tag{4.35}$$

It was again assumed that the material in the cohesive zone deformed according to the pseudo stress model in Figures 4.2-4. Consequently, $\sigma_{2i} \neq \sigma_{2i}(\xi)$, but $\sigma_{2i} = \sigma_{2i}(t)$. This assumption may be reasonable for materials that are subject to constant strain rate loading under uniaxial tension. Thus, the work input becomes

$$W_f = \sigma_{2i} \int_0^\alpha \frac{\partial \Delta u_i^{ep}}{\partial \xi} d\xi = \sigma_{2i} \, \Delta u_i^{ep}\Big|_\alpha . \tag{4.36}$$

Substituting Equation 4.34 into Equation 4.36 and, making use of the fact that $\Delta u_i^{ep}\Big|_\alpha$ is independent of time during steady state crack growth, yields

$$W_f = \frac{1}{E_R(T,c)} \int_0^t E(t' - \tau') \frac{\partial \left(J_f \right)}{\partial \tau} d\tau . \tag{4.37}$$

Because of the result given in Equation 4.28, the work input becomes

$$W_f = \frac{1}{E_R(T,c)} \int_0^t E(t'-\tau') \frac{\partial\left(J_v\right)}{\partial \tau} d\tau. \tag{4.38}$$

The integrand can be simplified by picking a constant modulus. Schapery (1975c) did this by choosing the modulus at a time $t = k\alpha / \dot{a}$, where k is a factor which depends on is the slope $n = \partial\left(\log E\right) / \partial\left(\log t\right)$ of the transition of the relaxation function. This assumption is quite reasonable for small values of n which is the case for the epoxy primer considered here. Thus, the work input at a particular combination of temperature T and solvent concentration c becomes

$$W_f = \frac{1}{E_R(T,c)} E\left(\frac{k\alpha / \dot{a}}{a_T(T,c)} \right) J_v . \tag{4.39}$$

Because the fracture energy Γ which is defined like a surface energy, is twice the work input to the failing material,

$$2\Gamma = \frac{1}{E_R(T,c)} E\left(\frac{k\alpha / \dot{a}}{a_T(T,c)} \right) J_v . \tag{4.40}$$

Equation 4.40 essentially requires the condition that the pseudo tractions and displacements in a failure zone with fixed $\dot{a}$ and α are constant during the time interval $\alpha / \dot{a}$ for a crack to propagate over the cohesive zone length. This condition is satisfied for the steady state crack growth considered in this study.

There are some restrictions to using the generalized J integral with the pseudo stress instead of the pseudo strain. The third correspondence principle (Schapery, 1984) usually applies to crack healing. However, it can also be used for steady state crack growth, which does not violate the condition that $dS_T / dt \leq 0$ when the position of the prescribed displacement moves at the same speed as the crack tip. In other words, the third correspondence principle applies to crack growth when both the crack tip and the applied displacement move at the same speed. The instrumented wedge experiment (Fig. 4.1) is just such a case.

4.3.2 *Stress Analysis of the Driven Wedge Test*

The driven wedge test was conducted over a range of wedge speeds and temperature and humidity levels. A stress analysis on viscoelastic beam was required in order to extract the equivalent compliance as a function of a wedge speed. The compliance was required for determining the work input to the failure zone. Data was only taken once the steady state crack speed matched the wedge speed. For convenience, Figure 4.7 (a) shows the specimen being driven over a fixed wedge. As a result, the stress analysis of the driven wedge test reduced to an analysis of a propped cantilever beam being driven over a fixed prop. In this problem, the amount of relaxation in the beam depends on the drive speed, thereby affecting the compliance. The curvature of the beam was found in order to determine the equivalent elastic compliance causing the same curvature of the viscoelastic beam.

The beam was divided (Fig. 4.7 (b)) into N equal elements. Thus, each element had a length, dx, which suffered a different loading history. For example, element 0 has just become part of cantilever and will be subjected to the same stress history as element N, which is about to leave the cantilever, underwent. As a result, each element has a different curvature which gave rise to the deflected shape of the beam which in turn becomes a function of the drive speed. Standard correspondence principle or extended correspondence principle could not be used because of the fact that displacement-prescribed boundary surfaces and traction-prescribed boundary surfaces are mixed. Thus, the linear viscoelastic stress analysis had to be conducted on each segment of the beam.

The curvature, K for each segment of a beam along a longitudinal axis is using linear elastic beam theory

$$K = \frac{M}{EI}, \tag{4.41}$$

where M is a moment, E is Young's modulus and I is a moment of inertia of the section.

For each element of a linear viscoelastic beam, the curvature is

$$K(t) = \frac{1}{I}\int_0^t \frac{1}{E(t-\tau)} \frac{\partial M(\tau)}{\partial \tau} d\tau \,. \tag{4.42}$$

Because the slope of $\log E(t)$ versus $\log t$ is small, $1/E(t)$ can be replaced by $D(t)$, the uniaxial creep compliance using quasi-elastic approximation (Schapery, 1965). Then, the curvature becomes

$$K(t) = \frac{1}{I}\int_0^t D(t-\tau) \frac{\partial M(\tau)}{\partial \tau} d\tau \,. \tag{4.43}$$

Because the moment applied to each element can be expressed as

$$M_i = P \times l_i \,, \tag{4.44}$$

where P is the load applied to the tip of the beam and l_i is the distance between the tip of the beam and each element.

For the time interval of Δt after the first element becomes subject to loading,

$$K_{(1)}(t=\Delta t) = \frac{P_o\left(a_0 - \Delta x\right)}{I} \int_0^{t=\Delta t} D(t-\tau) \frac{\partial}{\partial \tau}\left[H(\tau)\right] d\tau \,, \tag{4.45}$$

where P_o is taken constant for steady state crack growth, a_o is the crack length or the moment arm during steady state crack growth. Because $\partial\left[H(\tau)\right]/\partial\tau = \delta(\tau)$,

$$IK_{(1)}(t=\Delta t) = P_o\left(a_0 - \Delta x\right) D(t=\Delta t) \,. \tag{4.46}$$

The second element is subject to smaller moment by $P_o\Delta x$ because of the shorter moment arm, so its curvature can be expressed as

$$IK_{(2)}(t=2\Delta t) = P_o\left(a_0 - \Delta x\right) \int_0^{t=2\Delta t} D(t-\tau) \frac{\partial}{\partial \tau} \begin{bmatrix} \left(a_0 - \Delta x\right) H(\tau) \\ -\Delta x H(\tau - \Delta\tau) \end{bmatrix} d\tau \,. \tag{4.47}$$

Note that the time duration was $t = 2\Delta t$ which includes the loading history applied to the first element from $t = 0$ to $t = \Delta t$. The curvature of the second element can be arranged to

$$IK_{(2)}(t = 2\Delta t) = P_o a_0 D(t = 2\Delta t) - P_o \Delta x D(t = 2\Delta t) - P_o \Delta x D(t = \Delta t) \tag{4.48}$$

In a similar manner, the i^{th} element would have a curvature of

$$\begin{aligned} IK_{(i)}(t = i\Delta t) &= P_o a_0 D(t = i\Delta t) - P_o \Delta x D(t = i\Delta t) - P_o \Delta x D(t = (i-1)\Delta t) \\ &-P_o \Delta x D(t = (i-2)\Delta t) - \ldots - P_o \Delta x D(t = \Delta t) \end{aligned} \tag{4.49}$$

or,

$$IK_{(i)} = P_o a_0 D(t = i\Delta t) - \sum_{j=1}^{i} P_o \Delta x D(t = j\Delta t) \tag{4.50}$$

Because $\Delta x = \dot{a}\Delta t$

$$\frac{IK_{(i)}}{P_o} = a_0 D(t = i\frac{\Delta x}{\dot{a}}) - \sum_{j=1}^{i} \Delta x D(t = j\frac{\Delta x}{\dot{a}}). \tag{4.51}$$

Because $x = i\Delta x$

$$\frac{IK_{(i)}}{P_o} = a_0 D(t = \frac{x}{\dot{a}}) - \sum_{j=1}^{i} \Delta x D(t = \frac{x}{\dot{a}}). \tag{4.52}$$

The normalized curvatures at two different wedge speeds are shown in Figure 4.7. Note that the curvature would be straight line for linear elastic materials.

The effective time-independent compliance was determined at each position as

$$\hat{D}(x) = \frac{IK(x)}{P_o} \frac{1}{(a_0 - x)}. \tag{4.53}$$

The normalized effective compliance was determined by dividing $\hat{D}(x)$ by $\hat{D}(x = 0)$ at the crack tip. The normalized effective compliance was used to scale the modulus over the span of the beam. Consequently, the scaled modulus was used to compute the generalized J integral. The beam was divided into 10 groups of elements where each group consisted of 5 elements, each having the same modulus.

4.3.3 *Determination of Cohesive Zone Size and Mode Mix*

The previous section dealt with global stress distribution whereas this section deals with the stress distribution in the cohesive zone. As a result, this section describes how the cohesive zone size α was determined. Once the cohesive zone size is known, the work input to the cohesive zone could be determined using J_v (Eqn. 4.39).

The stress distribution in the cohesive zone was determined for each rate at which the wedge was driven into the specimen. The modulus, Poisson's ratio and power-law parameters at each rate were obtained from the calculations described in the previous sections. The crack length and the wedge displacement for each rate were obtained from the video measurements described in Section 2.1.2. This material, geometrical and boundary condition information was used as input data for numerical analysis using the finite element code ABAQUS. The finite element model consists of 6720 quadratic elements. The refined meshes with quarter point, plane strain elements were used for the crack tip. Crack blunting due to the power-law hardening nature of the material was allowed for by not tying the collapsed nodes of the quarter point elements. The crack tip mesh was further refined using a scheme called SUBMODEL which consisted of 784 elements.

The wedge displacement was prescribed on three nodes on the epoxy fracture surface while the adjacent three nodes on the concrete surface were held fixed. The displacements of two outer nodes were adjusted to yield a smooth displacement field that matched the overall deformed configuration from the global analysis.

The fracture mode mix was obtained from the finite element solutions. In the case of linear analysis, the mode I and II stress intensity factors are extracted from the solutions using an interaction integral method. Then, the mode mix angle was

$$\psi = \tan^{-1}\left(\frac{K_2}{K_1}\right) \tag{4.54}$$

It was found that $\psi = -25.5^O \pm 5^O$ over the range of strain rates, temperature and humidity levels.

In the case of the nonlinear behavior, the fracture mode mix was obtained from the ratio of the shear stress to normal stress over a range of locations from the crack tip. Then,

$$\psi = \tan^{-1}\left(\frac{\sigma_{12}}{\sigma_{22}}\right) \tag{4.55}$$

It was found that ψ was $\psi = -15^O \pm 4$ for $3\times10^{-6} \le r \le 3\times10^{-5}$ m over the range of strain rates, at T = 23.5℃.

The cohesive zone was defined as the region where the stress levels exceeded the onset stress level for material failure. The 0.2% strain offset method was used to define the onset stress level from the pseudo stress-strain curves that were developed for uniaxial tension at each temperature and humidity level (Fig. 4.8). The specific onset stress levels for each case are given in Tables 4.1 and 4.2. Note that the stress levels following onset were slightly dependent on strain level and were rate-dependent, as suggested by the pseudo stress model. As a result, the traction-separation law for this problem was rate-dependent.

4.3.4 *Results and Discussion*

The data from the driven wedge test at various wedge speeds, temperature and humidity levels are now presented. The values of the generalized J integral during steady state crack growth and the corresponding cohesive zone sizes were determined by finite element analyses that represented the material behavior through the pseudo stress model. These were then used to determine the fracture energy of the concrete/primer interface.

The driven wedge tests were conducted at 23.5, 32.2, 40.6 and 48.9°C. The humidity levels were 35, 65, 75, 95%RH at 40.6°C. In separate experiments, the wedge was driven at constant speeds of $2.5\text{x}10^{-2}$, $7.6\text{x}10^{-3}$, $2.5\text{x}10^{-3}$, $7.6\text{x}10^{-4}$, $2.5\text{x}10^{-4}$, $2.5\text{x}10^{-5}$, $7.6\text{x}10^{-6}$, $2.5\text{x}10^{-6}$, $2.5\text{x}10^{-7}$ and $5.1\text{x}10^{-8}$ m/s. The raw data from experiments at the four temperature levels are shown in Figure 4.9 as plots of crack length vs. crack speed. The crack length is essentially an indicator of the load level in any particular experiment because it can be transformed into the generalized J integral using the procedures described in earlier parts of this section.

Slower crack growth rates led to shorter crack lengths. This can be attributed to the fact that the stress relaxed more over sections of the beam that were subjected to loading for a longer period of time. In addition, the faster wedge speed caused more brittle failure at the interface due to the fact that the ultimate strain generally decreases with increases in the deformation rate. The higher temperatures generally lowered the crack length except for the experiment at 48.9°C. This can be ascribed to the fact that the effect of the stress relaxation in the beam was stronger than the decrease in the fracture energy at higher temperature levels. The crack lengths were independent of crack speeds and almost the same at 40.6°C and 48.9°C. This can be ascribed to the fact that the stress relaxation of the beam balanced the decrease in fracture energy. The crack lengths at various humidity levels are shown in Figure 4.10. Within the uncertainty of measurements, the crack length seemed to be independent of the wedge speeds at 40.6°C and all humidity levels except

95%RH. This is probably also due to the balance between stress relaxation and fracture energy.

The generalized J integral J_v was obtained via ABAQUS computations that made use of the pseudo stress model at various temperature and humidity levels (Fig. 4.10). The slower crack growth rates required higher values of the generalized J integral at 23.5°C and 32.2°C (Fig. 4.10a). This is because slower crack growth rates gave rise to smaller crack lengths, which in turn results in higher values of J_v. It is interesting to note that, within the scatter of measurements, J_v did not seem to be dependent on the temperature level. For this to be the case, the fracture energy must decrease because stress levels must decrease with increasing temperature. The effect of humidity is shown in Figure 4.10b. In all cases, the crack speeds were independent of the level of J_v. The data for 35 to 75%RH was independent of humidity level. However, there was noticeable decrease in J_v values at 95%RH.

The generalized J integral was obtained using the pseudo stress model that was calibrated with linear viscoelasticity (Fig. 4.11). When the nonlinear elasticity parameters were taken zero, the nonlinear viscoelastic pseudo stress model became the linear viscoelastic pseudo stress model with the same reference moduli. J_v increased significantly due to the fact that linear viscoelastic materials are stiffer than nonlinear viscoelastic materials when both have the same the reference modulus. The averaged ratio of linear to nonlinear generalized J integral are shown at each temperature and humidity level. The nonlinear effect was least at 48.9°C (Fig. 4.11a), which corresponded to the smallest cohesive zone (Fig. 4.12) obtained at the same temperature.

The cohesive zone size (Fig. 4.12) was determined at various crack speeds because it was required in order to compute the work input. The region over which the effective stress level was higher than σ^y (Fig. 4.8) was taken as the cohesive zone. The cohesive zone size decreased slightly with crack speed due to the higher stress created at higher deformation rates. The reason that the cohesive zone size varied slightly with crack speeds can be attributed to the fact that the volume of failing material is proportional to the length of the cohesive zone squared. Consequently, a cross plot of the cohesive zone size versus J_v would be relatively insensitive to it.

Once J_v and the cohesive zone size had been determined, it was possible to determine the fracture energy from Equation 4.40 and the reference and tensile relaxation modulus. The results are presented in Figure 4.13 which show the effect of temperature and relative humidity on the fracture energy.

In contrast to J_v, the fracture energy decreased (Fig. 4.13a) with lower crack growth rates for all the temperatures that were considered. The rate of decrease decreased with increasing temperature level. This was brought about by the accelerating time scale in the tensile relaxation modulus. The fracture energy decreased at higher temperature levels. This was expected because the activation energy for fracture should decrease with increasing temperature. The fracture energy at 48.9°C was almost 10 times smaller than that at 23.5°C.

At different humidity levels, the fracture energy also decreased (Fig. 4.13b) with decreasing crack growth rate. There was also significant drop in fracture energy as humidity levels were increased. The fracture energy at 95%RH was 20 times smaller than that at 35%RH. The difference between the curves was greatest between 75 and 95%RH. This corresponds to the large change in ramp tensile behavior (Fig. 4.4).

4.3.5 *Conclusions*

The nonlinear viscoelastic fracture behavior of the interface between the epoxy primer and concrete was examined through the driven wedge tests and characterized by making use of the pseudo stress model and the generalized J integral concept introduced by Schapery.

It was found that the fracture energy of the viscoelastic material was dependent on crack speed, temperature and humidity. This essentially means that the traction-separation law for the interface is rate-dependent.

5. Conclusions

The durability of adhesive joints between concrete and FRP reinforcement in aggressive environments was characterized at different loading rates and various temperature and humidity levels. Due to the hygrothermal viscoelastic behavior of the epoxy primer, linear and nonlinear viscoelastic characterizations were performed at various temperature and humidity levels. Nonlinear viscoelastic fracture analyses were used in order to account for nonlinear, rate-dependent interfacial fracture.

For the linear viscoelastic characterization, two experiments were conducted. Bulk longitudinal relaxation experiments simultaneously determined the two linear viscoelastic functions of the epoxy primer using a single specimen in a confining cylinder. The deformation of the confining cylinder accounted for the actual loading conditions. The linear viscoelastic functions, $K(t)$, $\mu(t)$, $E(t)$ and $\nu(t)$ were deduced using three-dimensional, linear viscoelastic constitutive equations. The transition zone of the bulk relaxation modulus was as wide as 13 decades.

Bulk creep experiments determined the bulk creep compliance in order to validate the bulk longitudinal experiments. Relatively low pressure levels were required by elongating the gage length effectively. Good agreement was obtained between both sets of experiments.

The thermal and hygral expansions of the primer were also measured. The parameters that characterized these responses were extracted and used in the development of nonlinear viscoelastic models.

The hygrothermal nonlinear viscoelastic characterization was conducted using napkin ring torsion and uniaxial tension experiments at three different strain rates and four temperature and humidity levels. A hybrid model was used to capture the hygrothermal nonlinear viscoelastic behavior of epoxy primer. It combined free volume concepts with nonlinearities introduced by Schapery.

The nonlinear viscoelastic fracture behavior of the interface between the epoxy primer and concrete was investigated by conducting a series of driven wedge tests. The pseudo stress model and the generalized J integral concept, which were introduced by Schapery, were used to compute the fracture energy.

It was found that the fracture energy of the viscoelastic material was dependent on crack speed, temperature and humidity. Faster growing cracks yielded higher fracture energies, suggesting that a rate-dependent traction-separation law governed the fracture process. High temperature and humidity levels decreased the fracture energy.

For future work, this durability study can be used in predictions of the life of FRP strengthened structures when used in conjunction with the fracture characteristics of concrete and FRP. Once the fracture behavior of concrete and FRP are characterized, it will be possible to account for most of the failure mechanisms that have been observed.

Tables

	Log(ρ_m) [s]	K_m [MPa]	μ_m [MPa]	E_m [MPa]	ν_m
1	-4.3	24.64	0.22	0.21	-3.11×10^{-4}
2	-3.3	25.54	0.45	0.11	-4.95×10^{-4}
3	-2.3	104.24	20.88	68.48	-8.31×10^{-4}
4	-1.3	29.14	20.32	29.72	-1.13×10^{-3}
5	-0.3	150.32	22.11	93.33	-3.19×10^{-3}
6	0.7	155.61	160.32	387.51	-2.40×10^{-3}
7	1.7	440.03	161.77	491.45	-5.44×10^{-3}
8	2.7	330.48	310.46	758.45	-6.53×10^{-3}
9	3.7	438.32	159.01	552.47	-1.19×10^{-2}
10	4.7	226.82	187.85	377.34	-1.66×10^{-2}
11	5.7	206.62	71.09	256.68	-1.74×10^{-2}
12	6.7	245.83	63.80	137.01	-2.59×10^{-2}
13	7.7	49.88	21.35	95.43	-6.03×10^{-2}
14	8.7	169.51	20.31	47.03	-1.18×10^{-2}
15	9.7	34.86	11.30	53.36	3.00×10^{-3}
16	10.7	82.59	6.45	15.69	-3.04×10^{-3}
17	11.7	11.97	3.08	17.01	2.20×10^{-3}
18	12.7	40.06	0.25	4.14	-9.92×10^{-4}
19	13.7	8.54	1.29	7.19	1.57×10^{-4}
	∞	2337.41	12.34	36.91	0.4974

$$K(t) = K_\infty + \sum_m^{19} K_m e^{-\frac{t}{\rho_m}}, \quad \mu(t) = \mu_\infty + \sum_m^{19} \mu_m e^{-\frac{t}{\rho_m}},$$

$$E(t) = E_\infty + \sum_m^{19} E_m e^{-\frac{t}{\rho_m}}, \quad \nu(t) = \nu_\infty + \sum_m^{19} \nu_m e^{-\frac{t}{\rho_m}}$$

Table 2.1: Prony series coefficients of linear viscoelastic functions.

T (°C)	E_R (GPa)	ν_R	α	σ^o (MPa)	n	σ^y (MPa)
23.5	2.46	0.406	0.001	20.6	16	29.3
32.2	1.05	0.445	0.001	11.0	20	14.3
40.6	0.600	0. 469	0.001	6.9	13	10.3
48.9	0.330	0. 481	0.001	4.83	10	7.89

Table 4.1: The reference modulus, Poisson's ratio, α , σ^o , n and σ^y at various temperatures.

RH (%)	E_R (GPa)	ν_R	α	σ^o (MPa)	n	σ^y (MPa)
35	0.600	0. 469	0.001	6.9	13	10.3
65	0.490	0.474	0.001	6.55	13	9.63
75	0.424	0.477	0.001	4.83	10	7.96
95	0.329	0.481	0.001	2.07	10	3.47

Table 4.2: The reference modulus, Poisson's ratio, α , σ^o , n and σ^y at various humidity at 40.6°C.

Figures

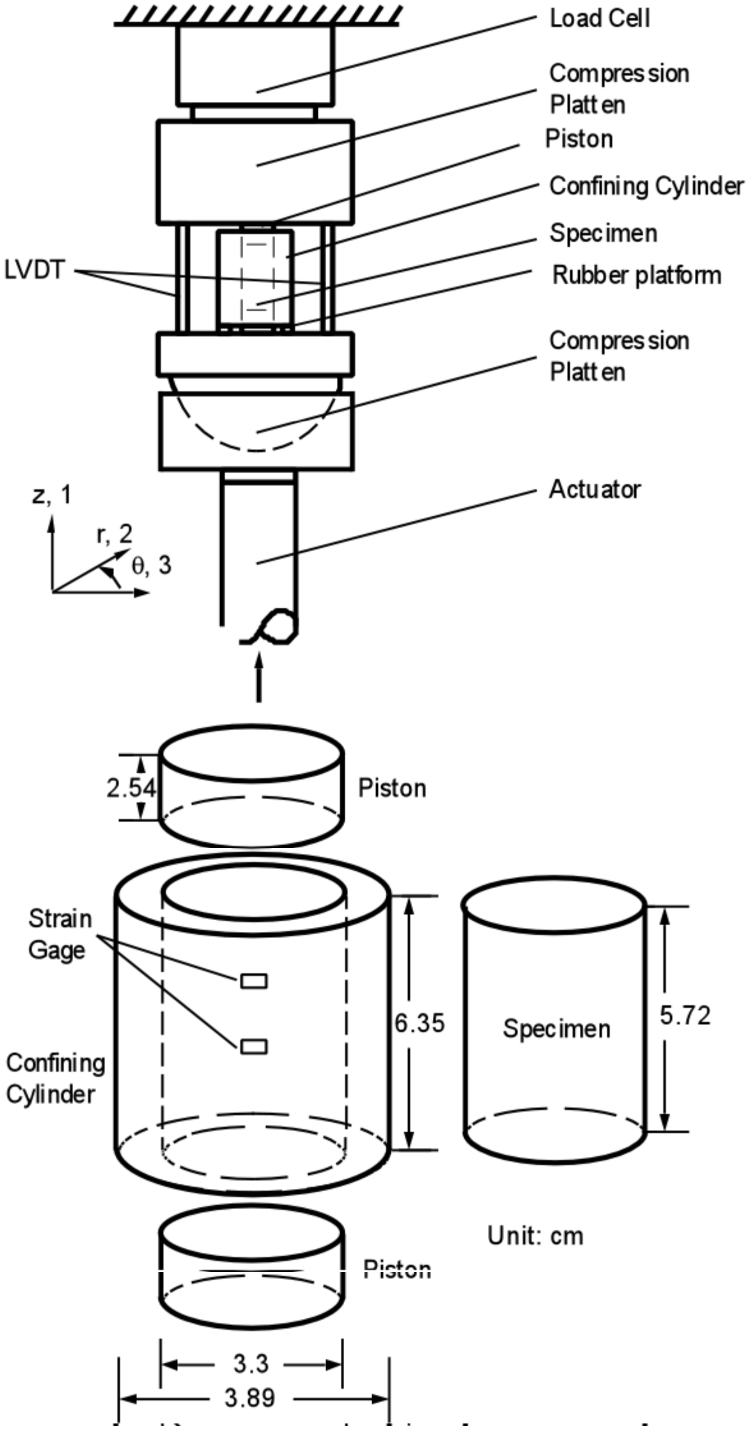

Figure 2.1: Schematic of longitudinal bulk relaxation modulus experiments.

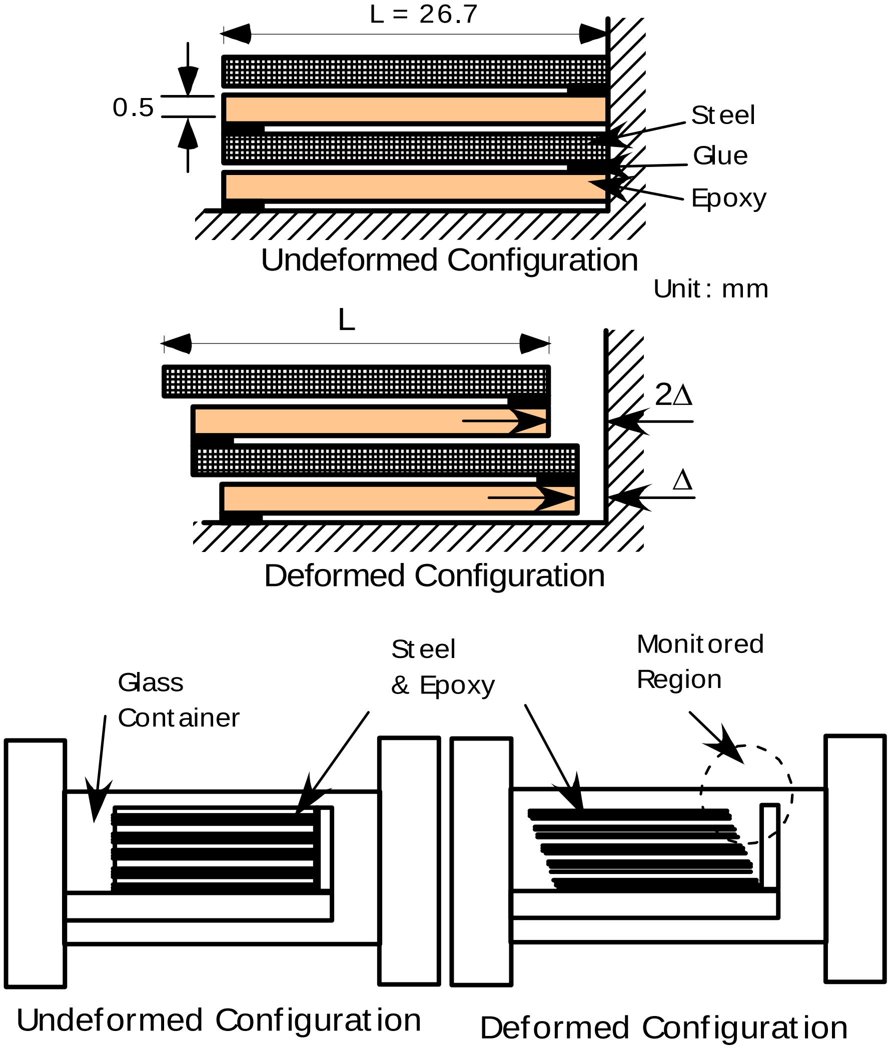

Figure 2.2: Deformed configuration of bulk compliance experiments.

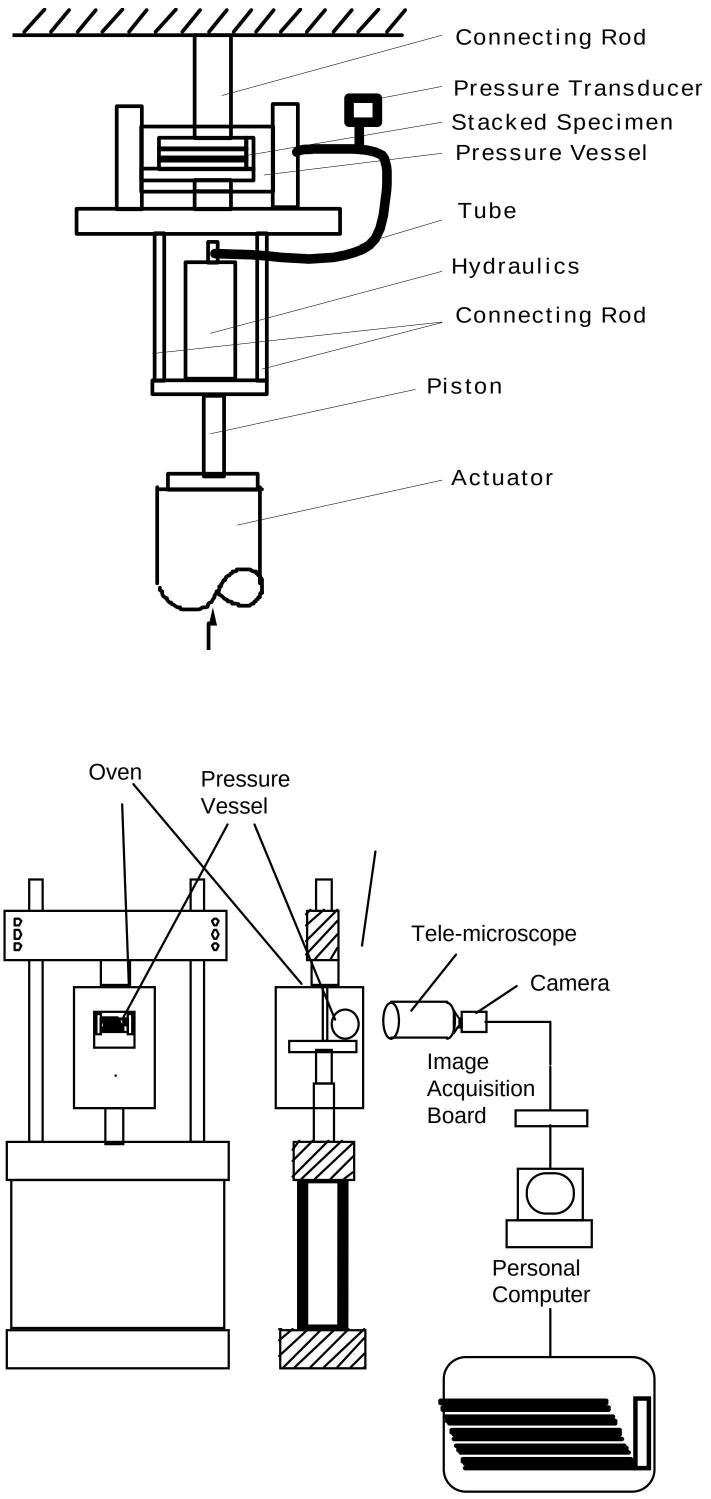

Figure 2.3: Schematic of bulk compliance experiments.

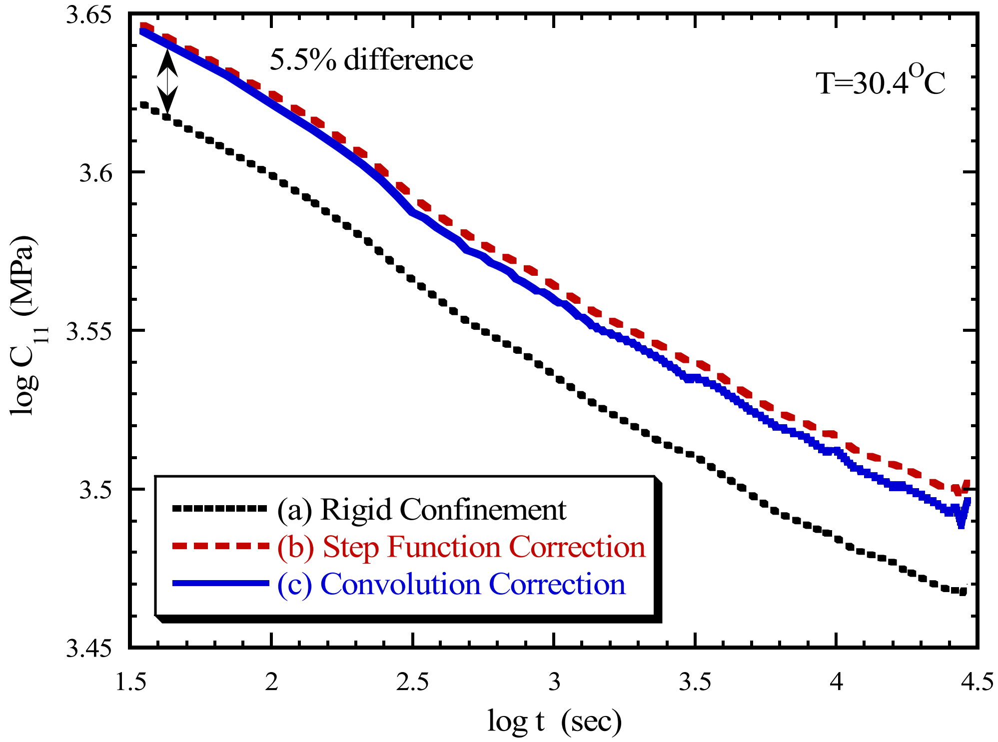

Figure 2.4: Values of $C_{11}(t)$ as calculated using (a) rigid confinement assumption, (b) step function correction and (c) convolution correction.

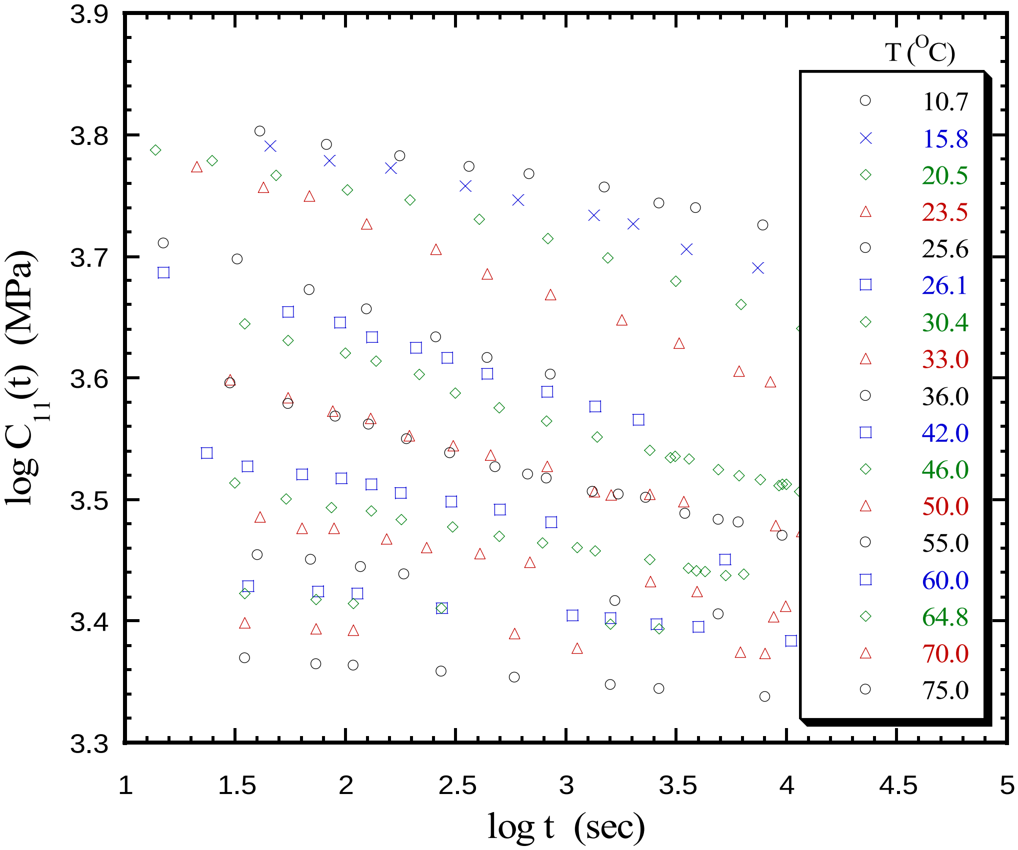

Figure 2.5: $C_{11}(t)$ at various temperature levels.

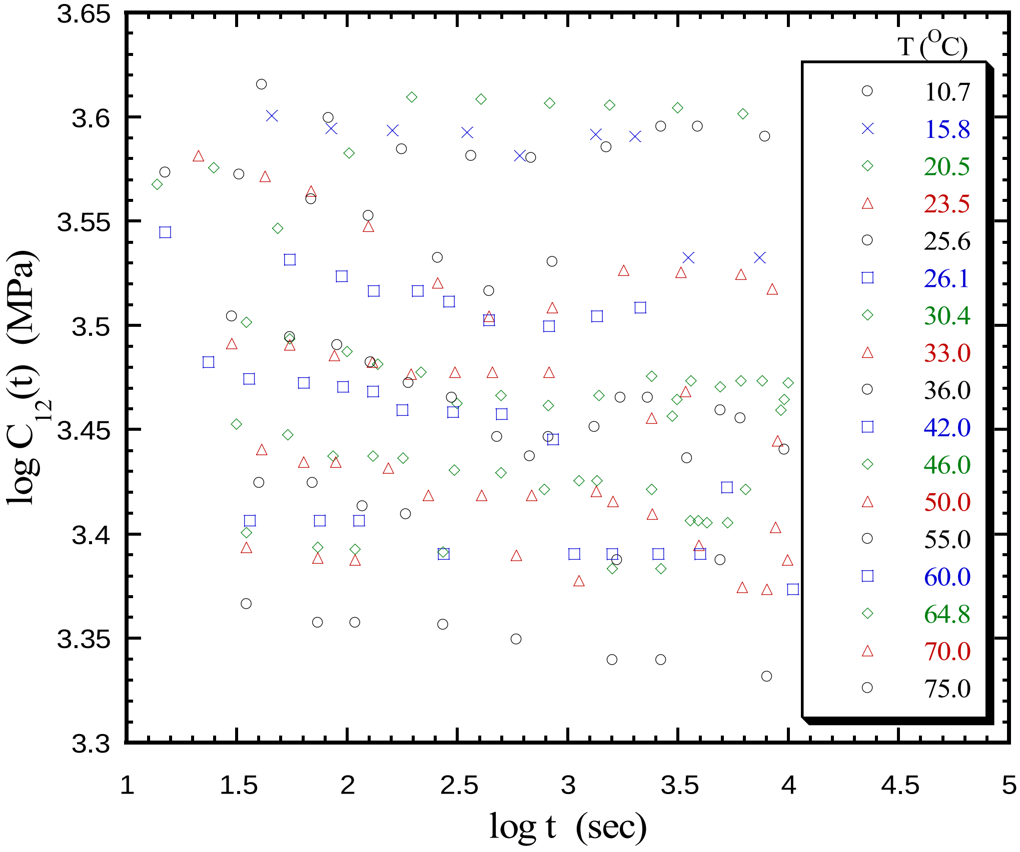

Figure 2.6: $C_{12}(t)$ at various temperature levels.

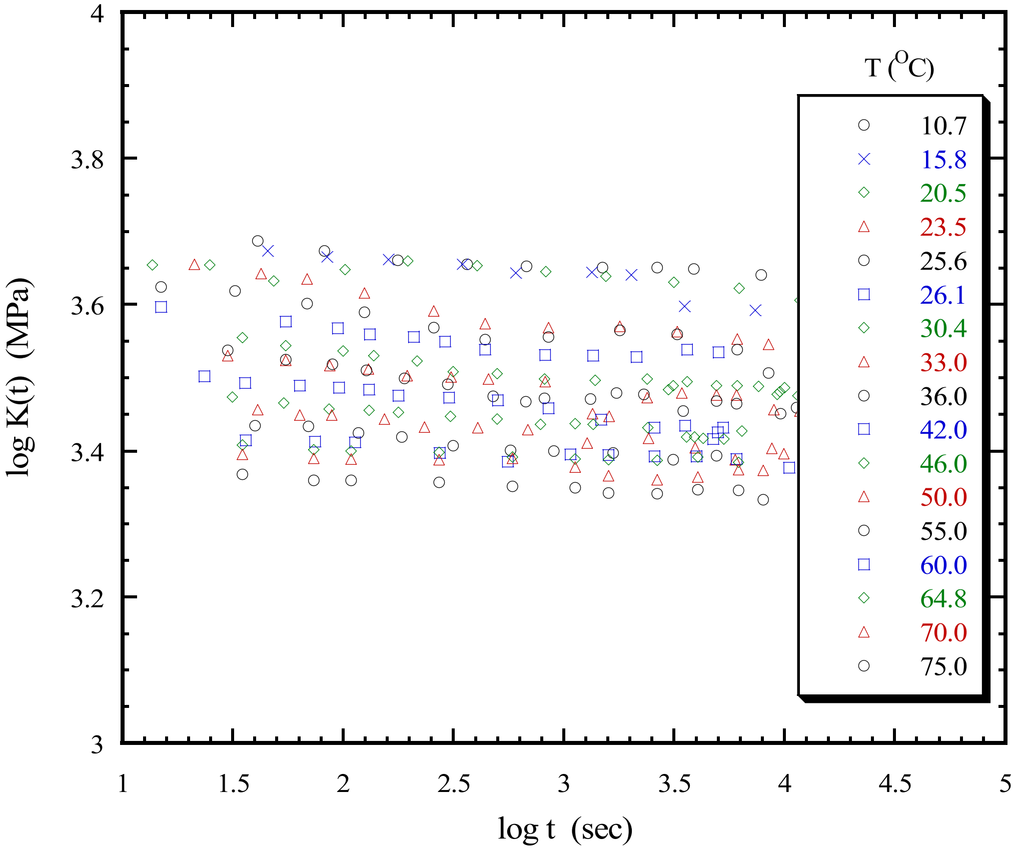

Figure 2.7: K(t) at various temperature levels.

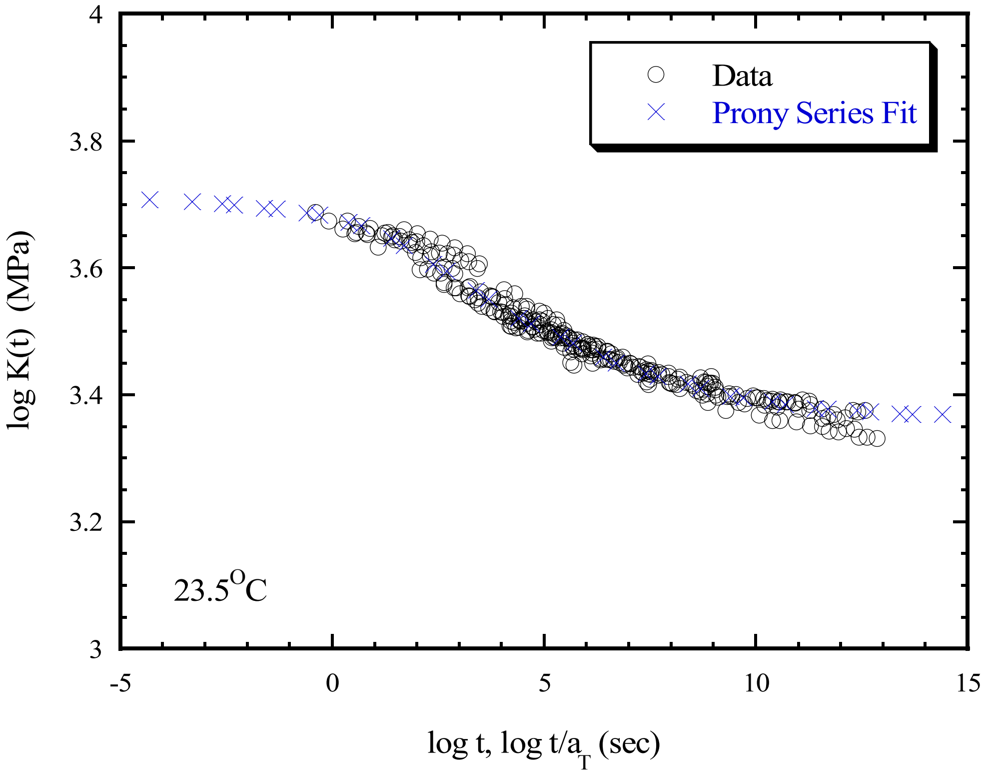

Figure 2.8: Master curve of K(t) and Prony series fit.

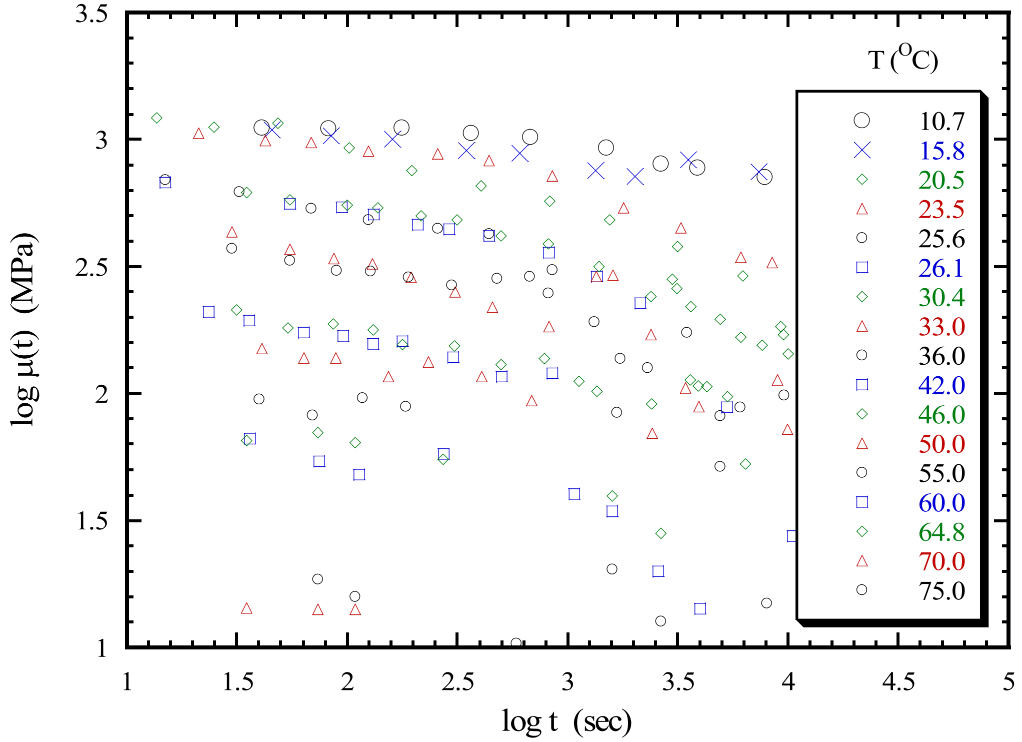

Figure 2.9: μ(t) at various temperature levels.

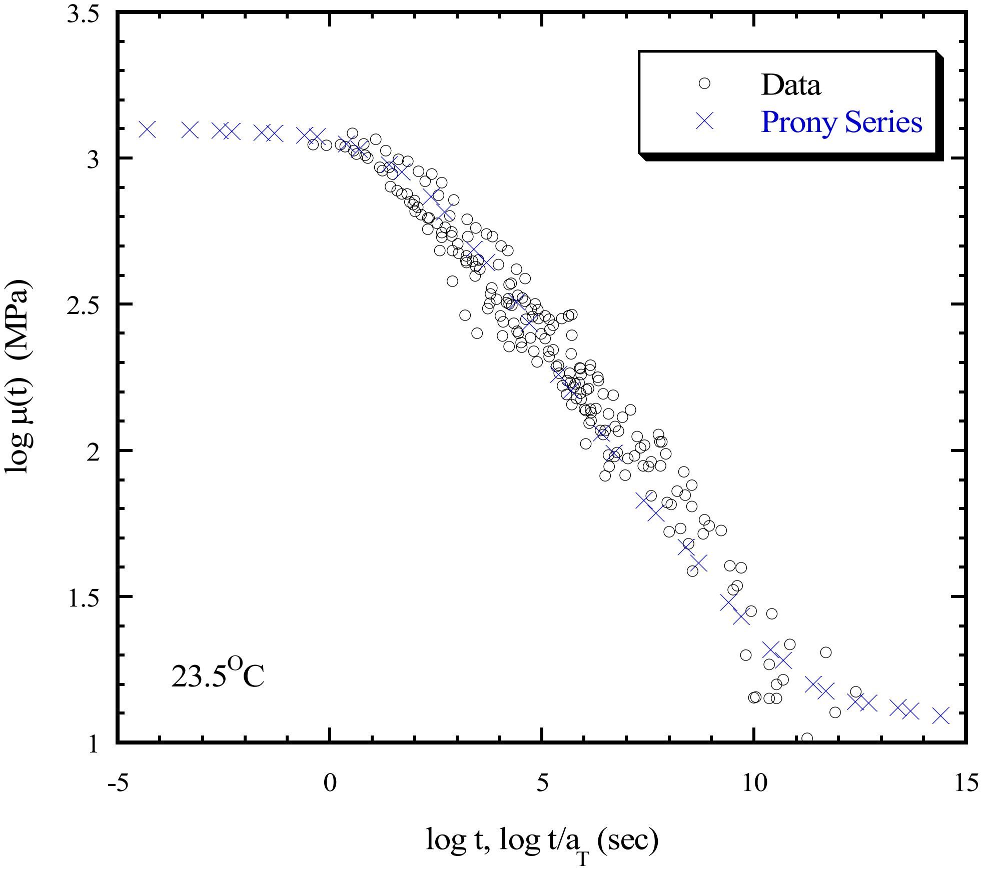

Figure 2.10: Master curve of $\mu(t)$ and Prony series fit.

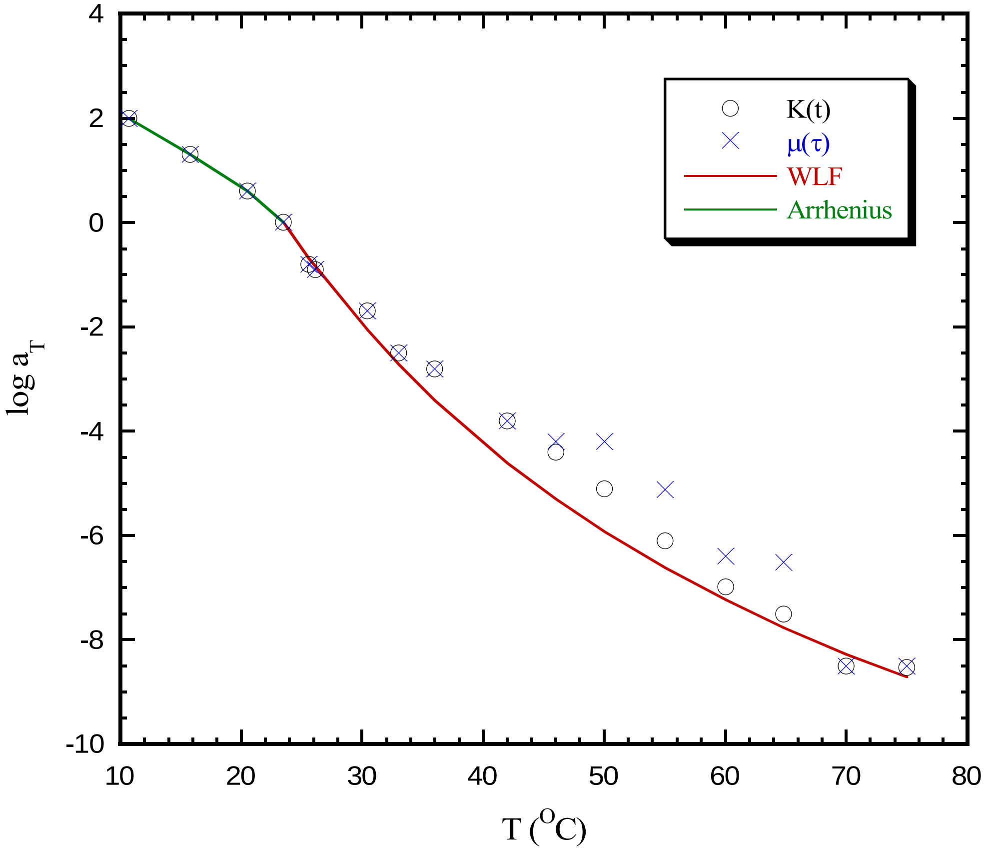

Figure 2.11: Thermal shifting factors for K(t) and μ(t).

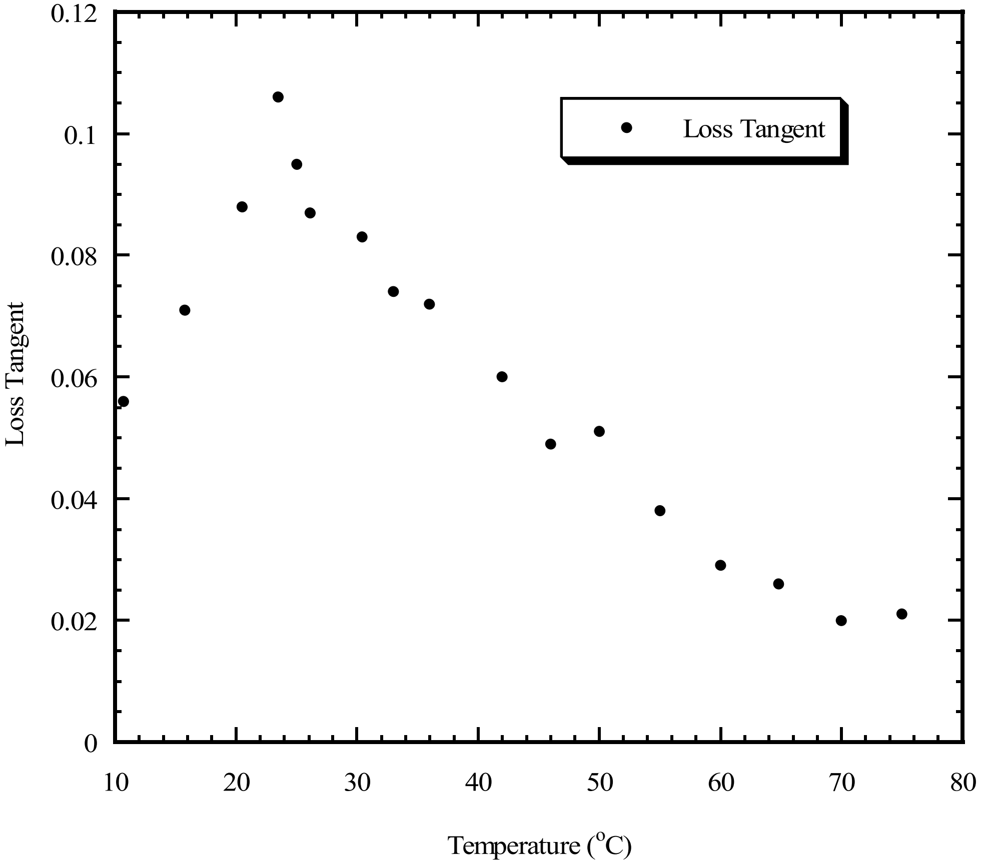

Figure 2.12: Loss tangent of $C_{11}(t)$ and the glass transition temperature.

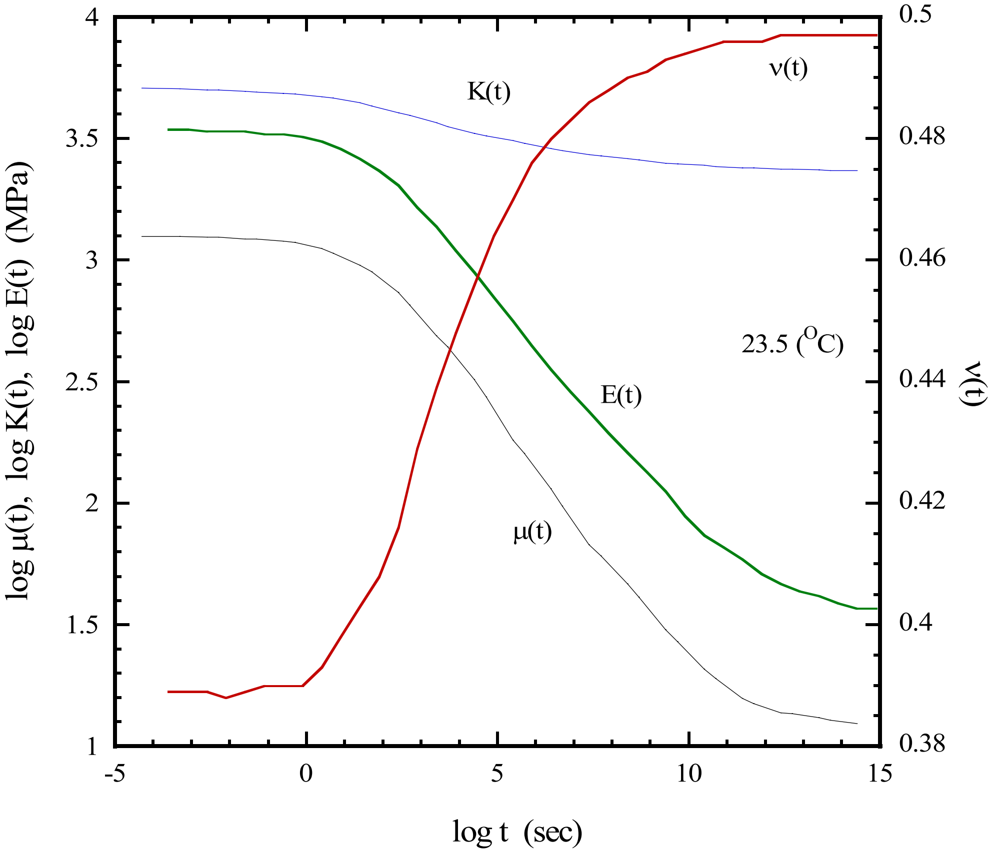

Figure 2.13: Measured and deduced linear viscoelastic relaxation functions.

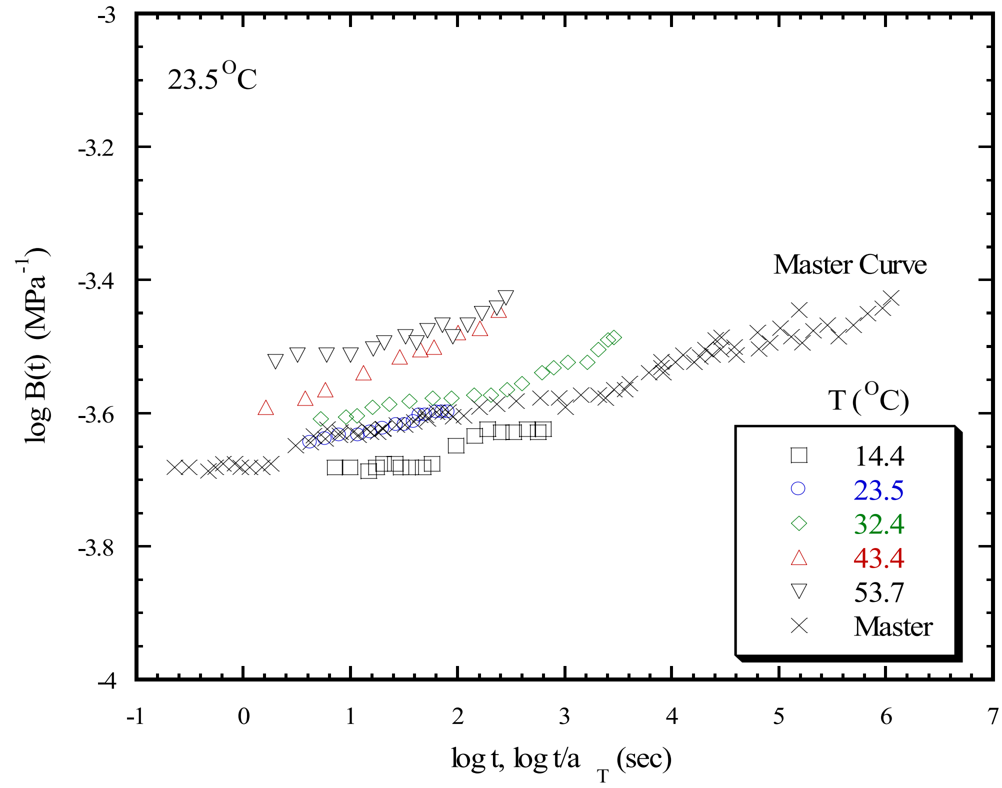

Figure 2.14: B(t) at various temperature levels.

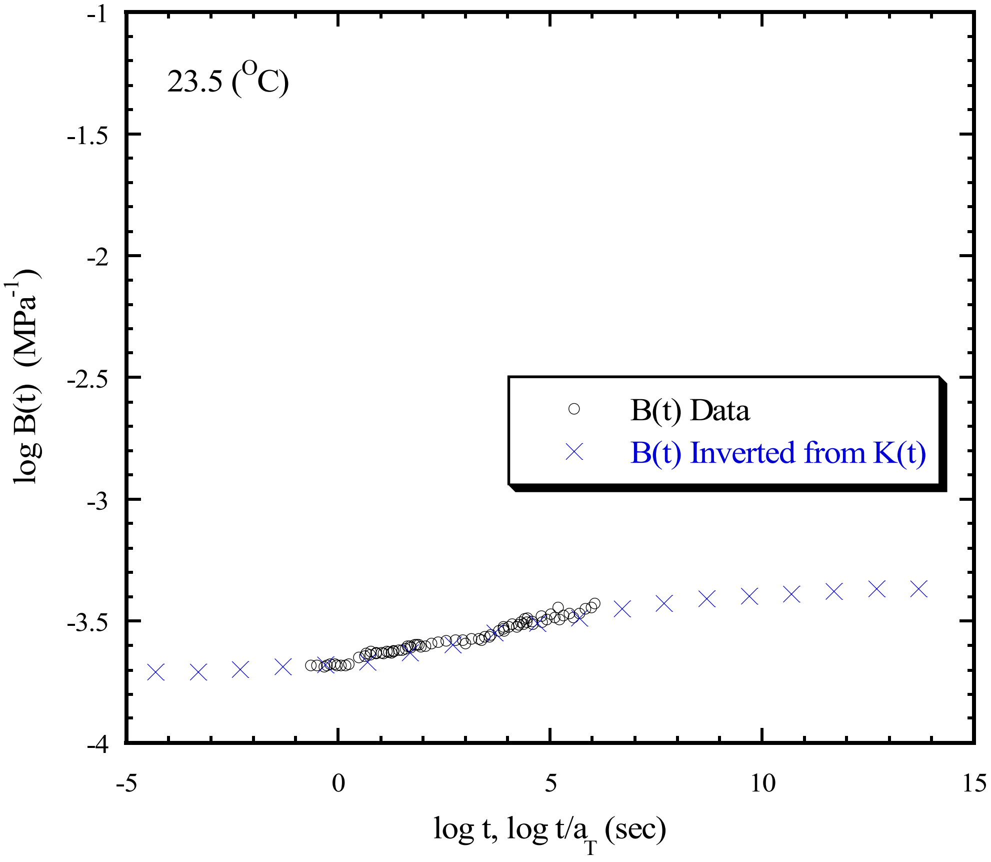

Figure 2.15: B(t) from bulk compliance experiments and B(t) deduced from bulk longitudinal relaxation modulus experiments.

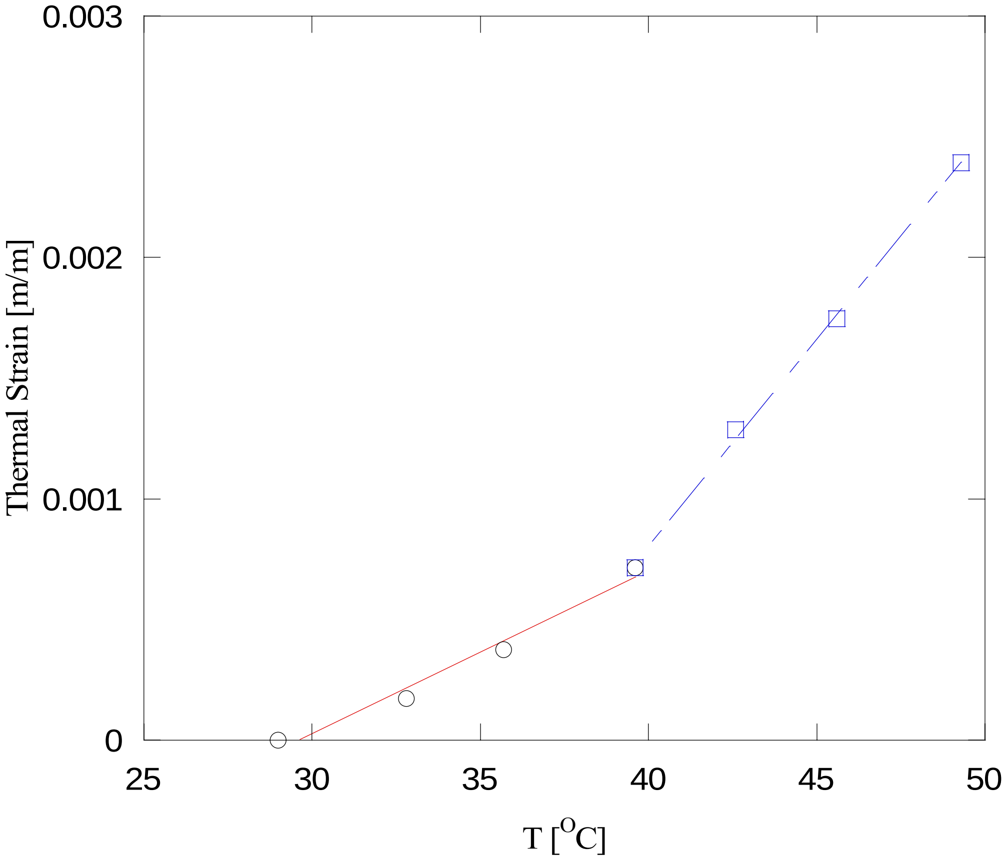

Figure 2.16: Thermal expansion behavior.

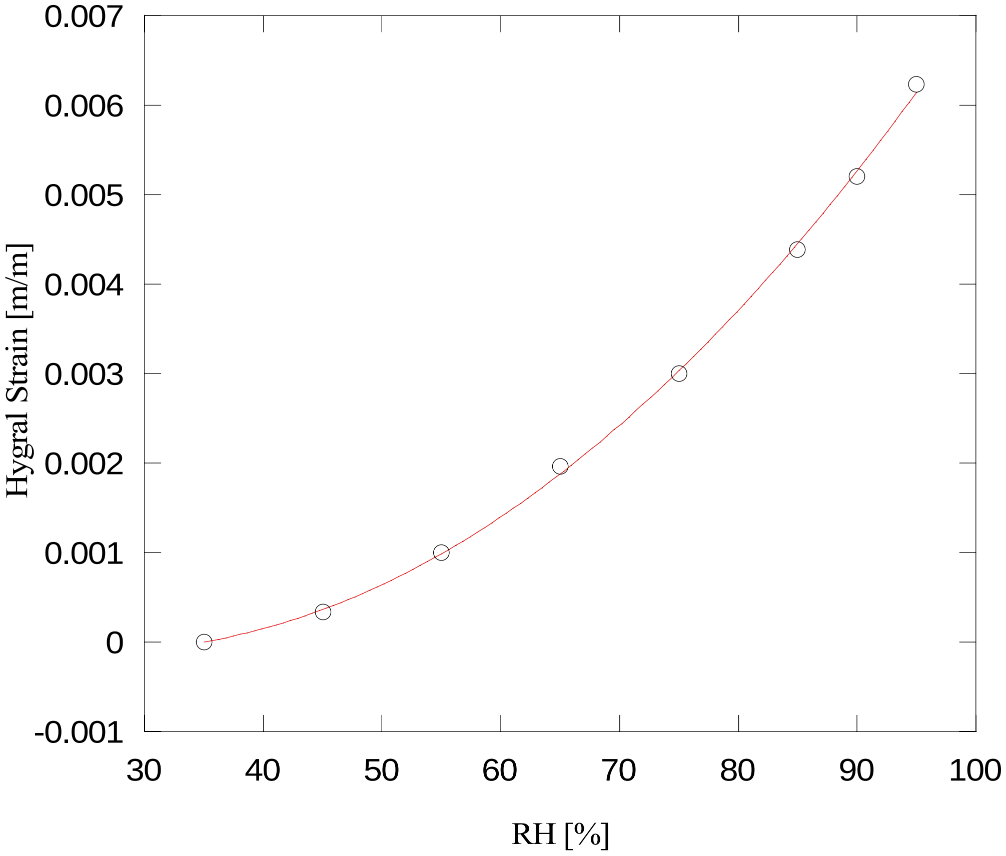

Figure 2.17: Hygral expansion behavior at 40.6^{O}C.

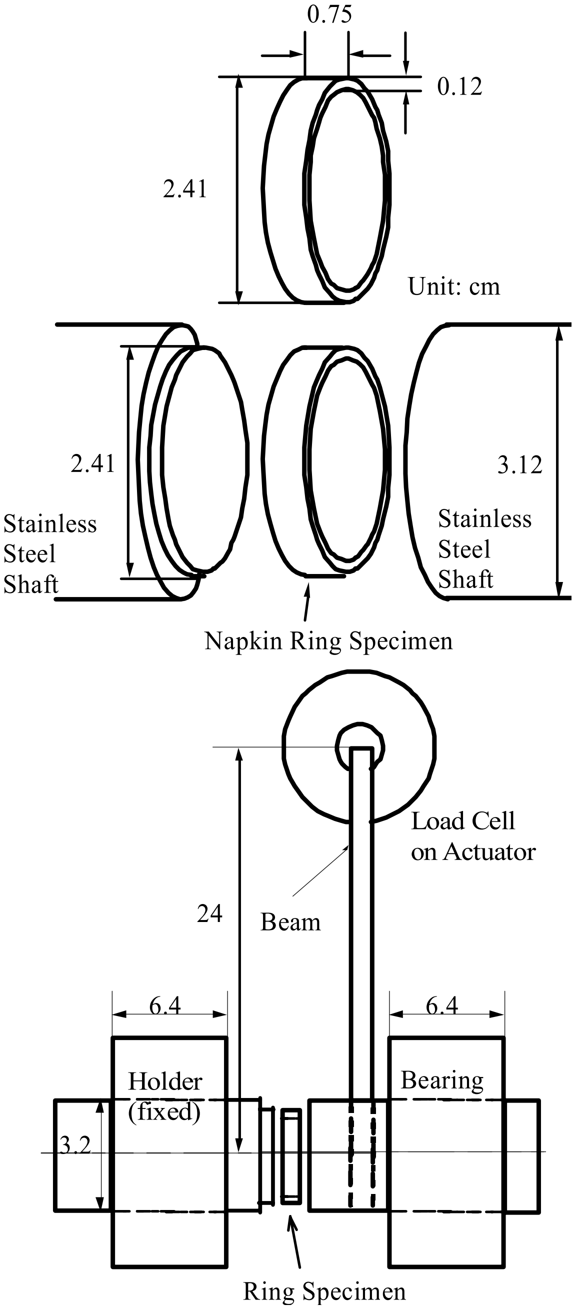

Figure 3.1: Schematic of napkin ring torsion tests.

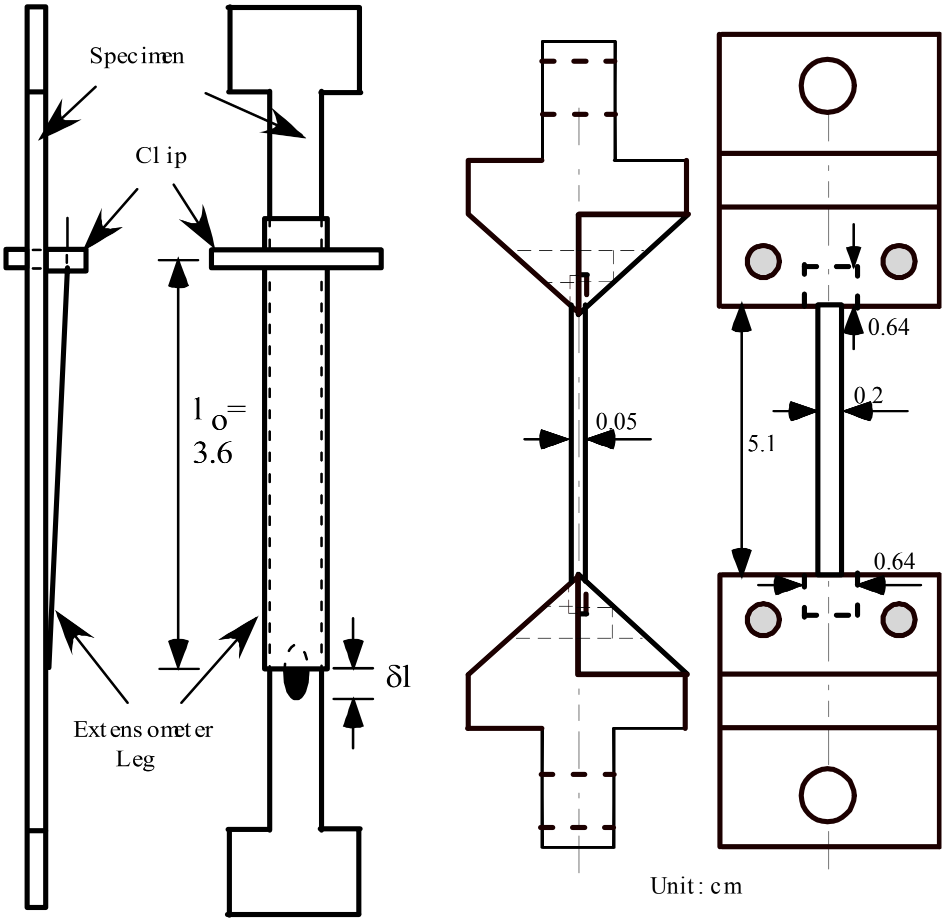

Figure 3.2: Uniaxial tension specimen and the grips.

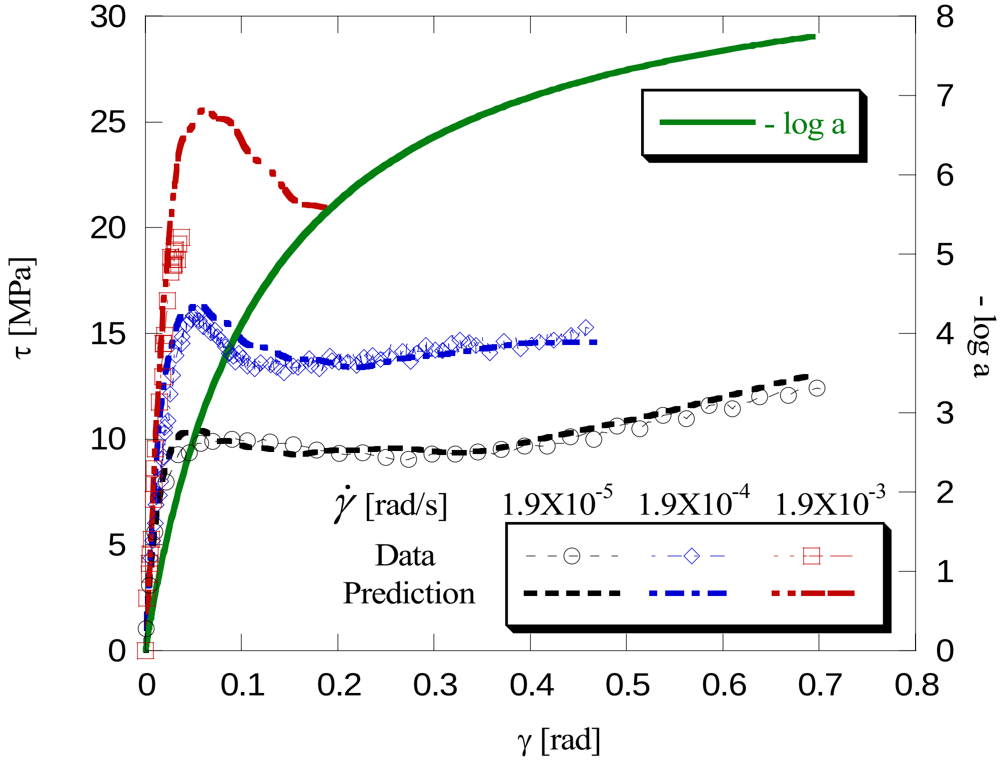

Figure 3.3: Torsion test data and predictions for the primer at 23.5°C and 35% RH.

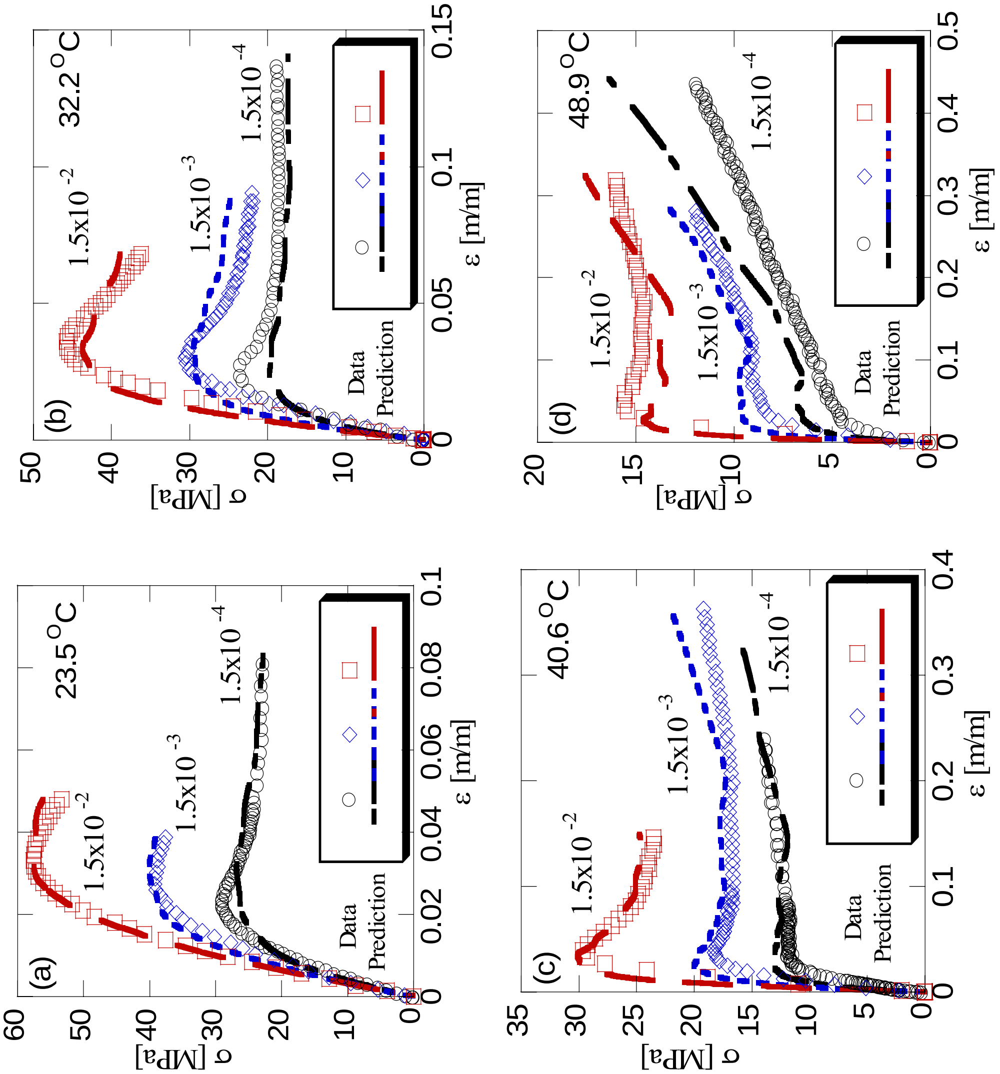

Figure 3.4: Uniaxial tension data and predictions at various temperature levels.

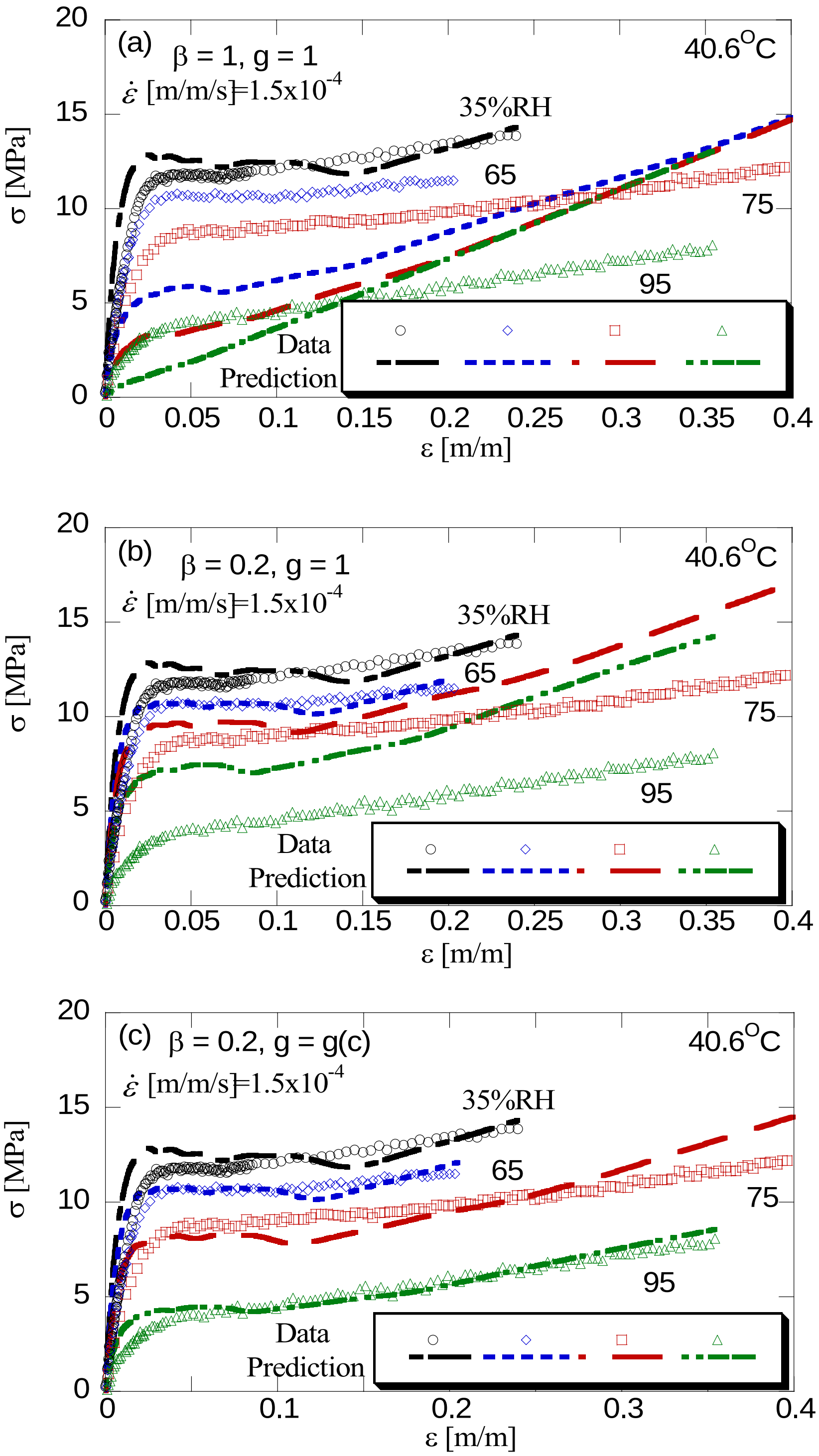

Figure 3.5: Uniaxial tension data and prediction at 40.6°C and various %RH levels.

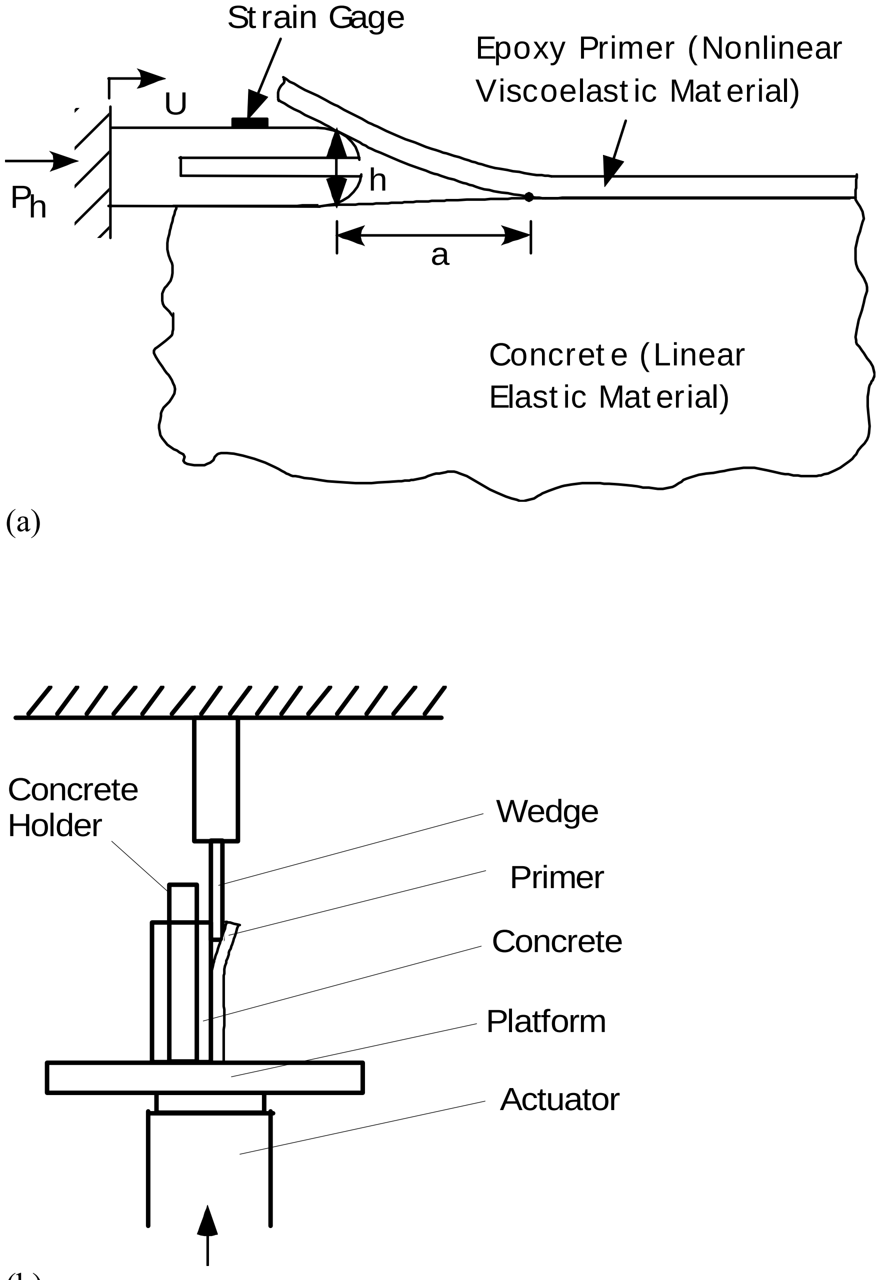

Figure 4.1: Schematic of driven wedge tests.

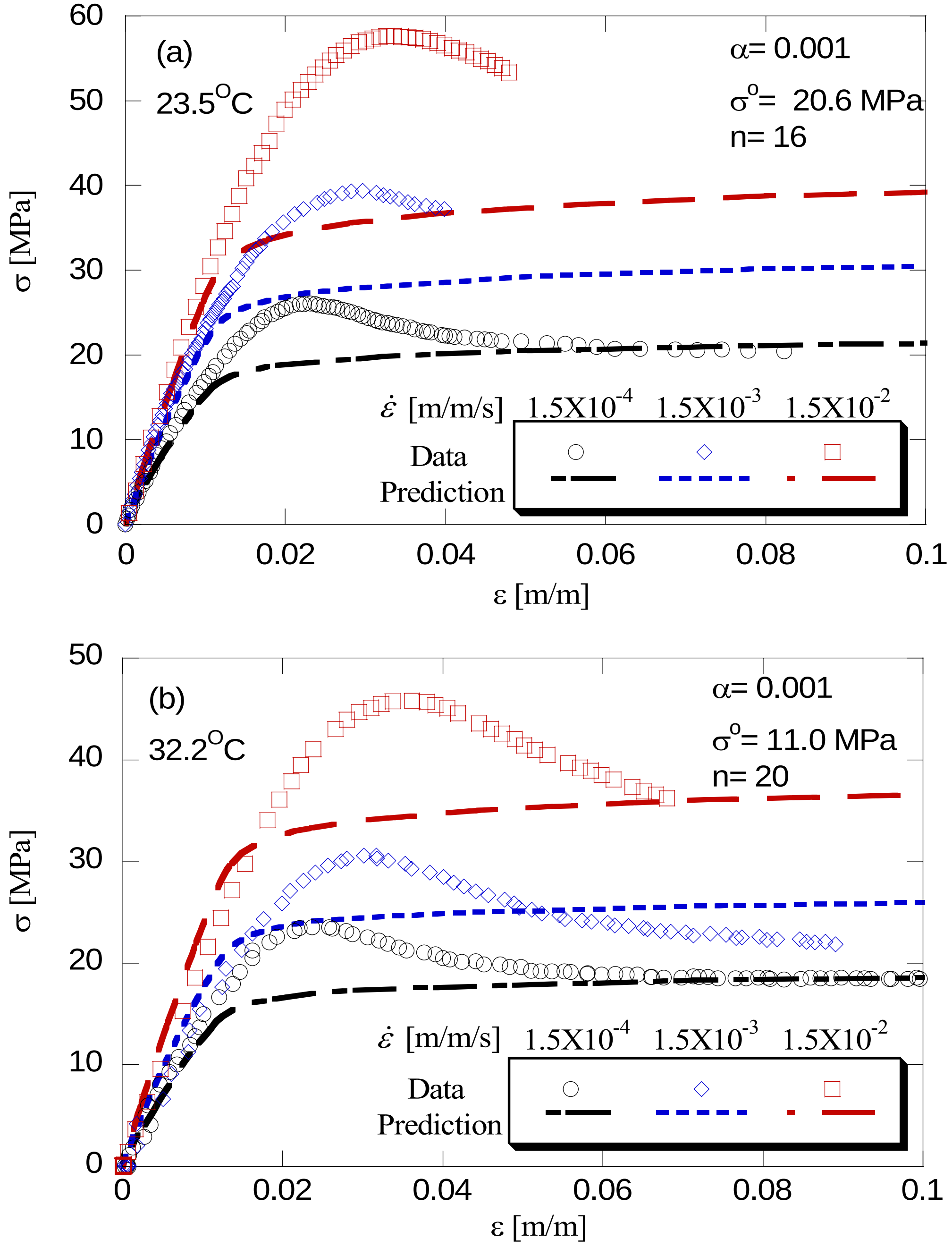

Figure 4.2: Pseudo stress model under tension at 23.5°C and 32.2°C.

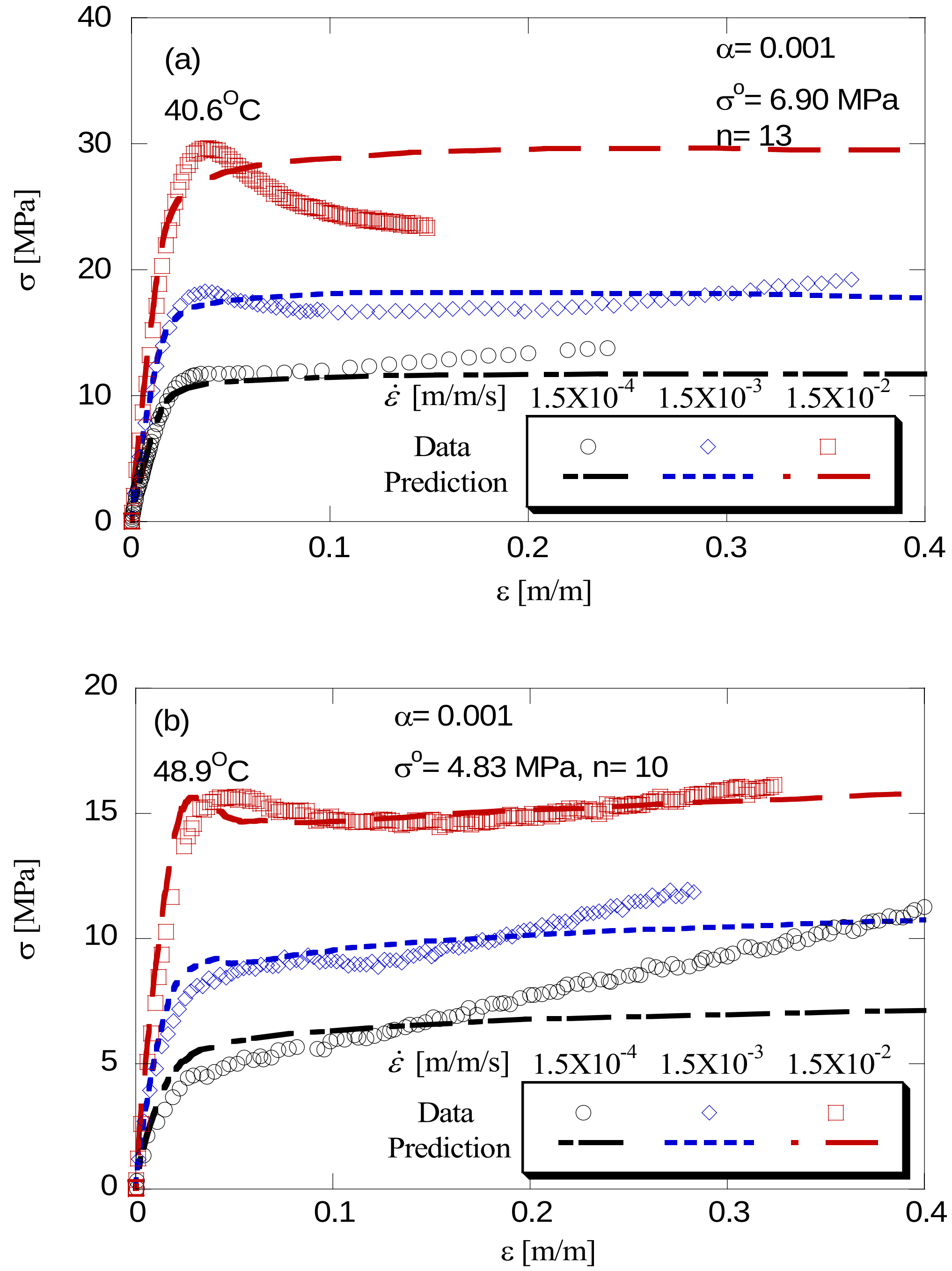

Figure 4.3: Pseudo stress model under tension at 40.6°C and 48.9°C.

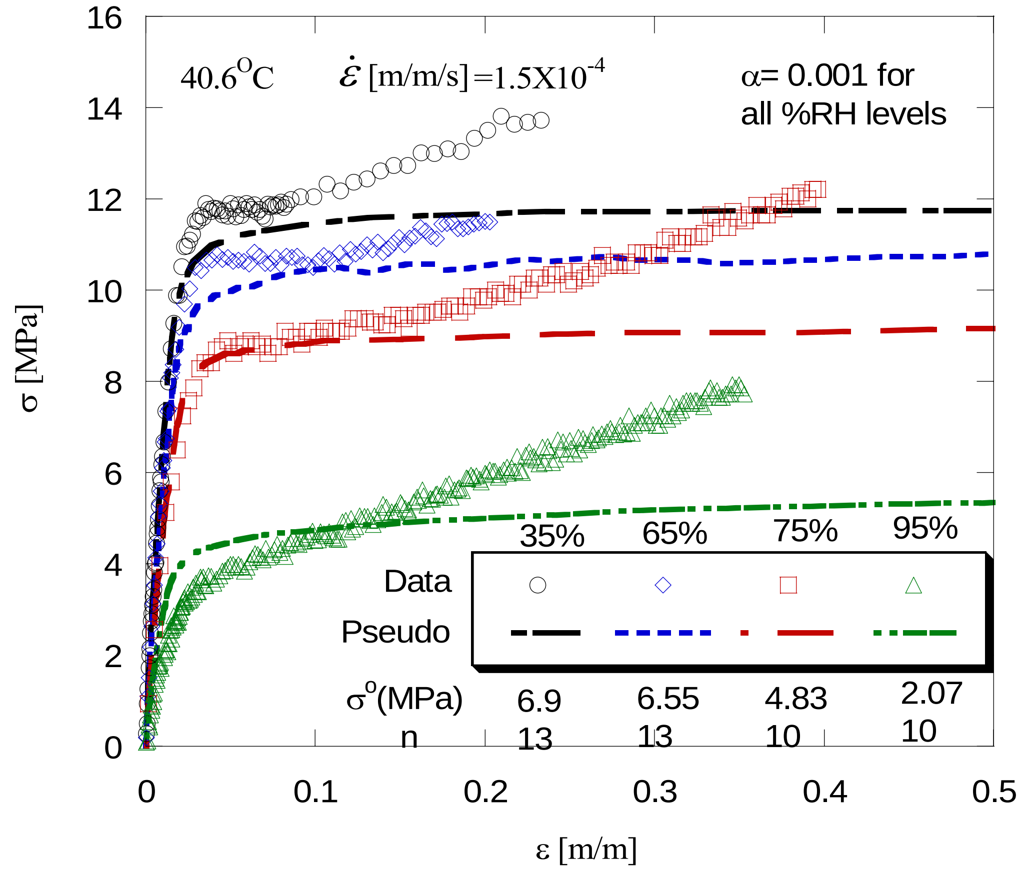

Figure 4.4: Pseudo stress under tension at 40.6°C and various humidity levels.

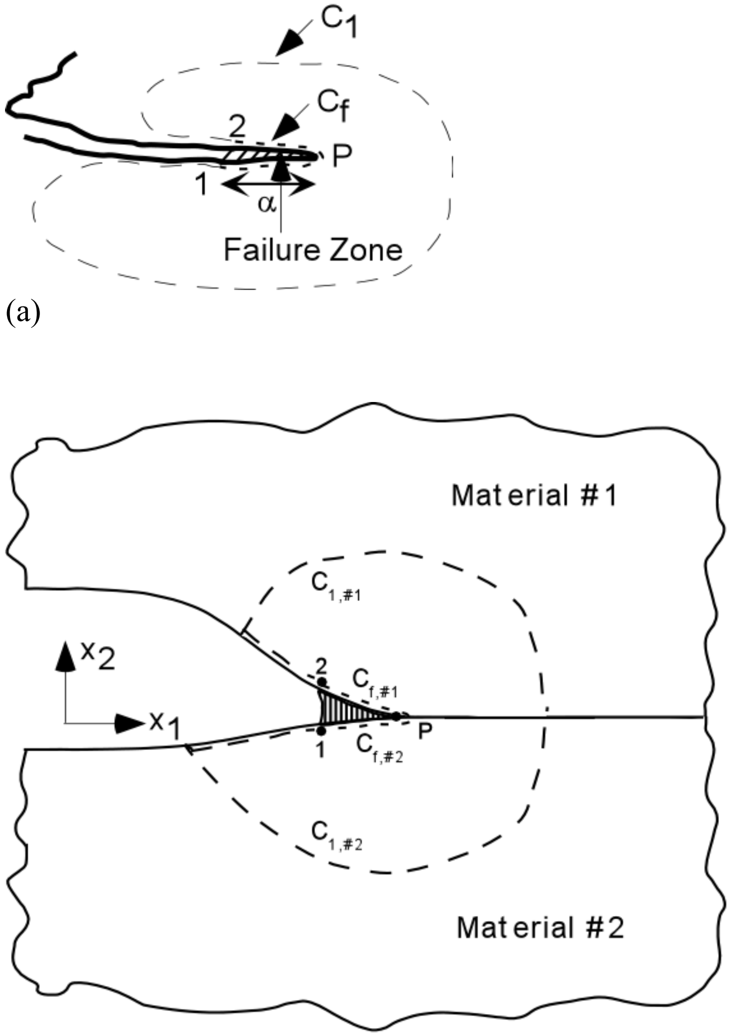

(a)

(b)

Figure 4.5: Contours of line integrals for (a) homogeneous materials and (b) bimaterials

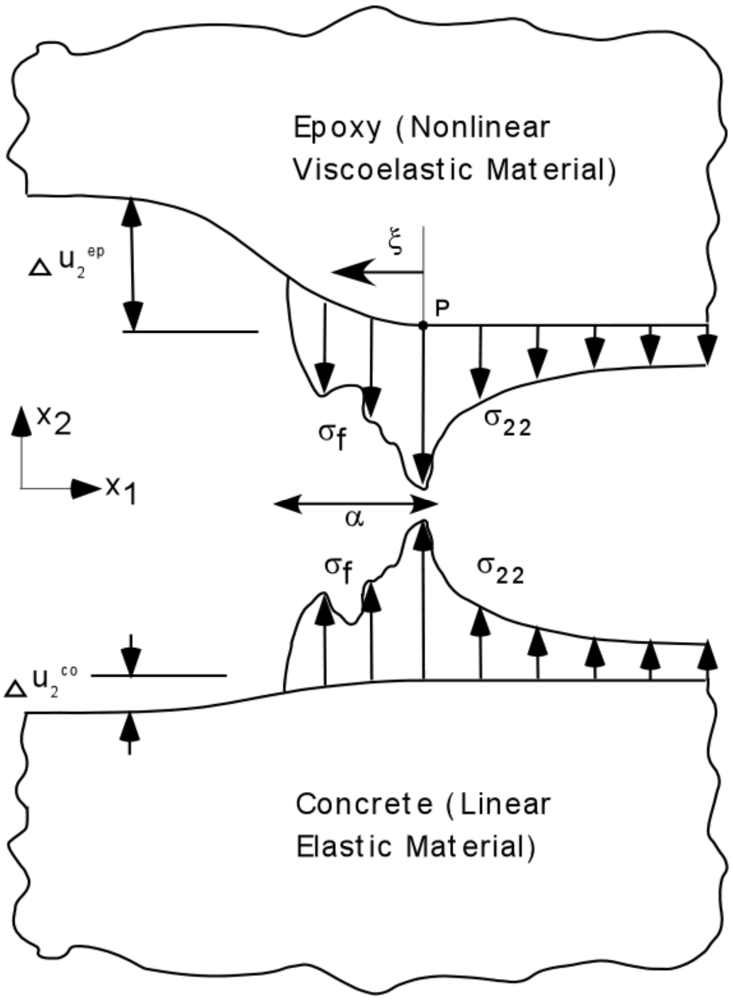

Figure 4.6: Stress distribution in a failure zone.

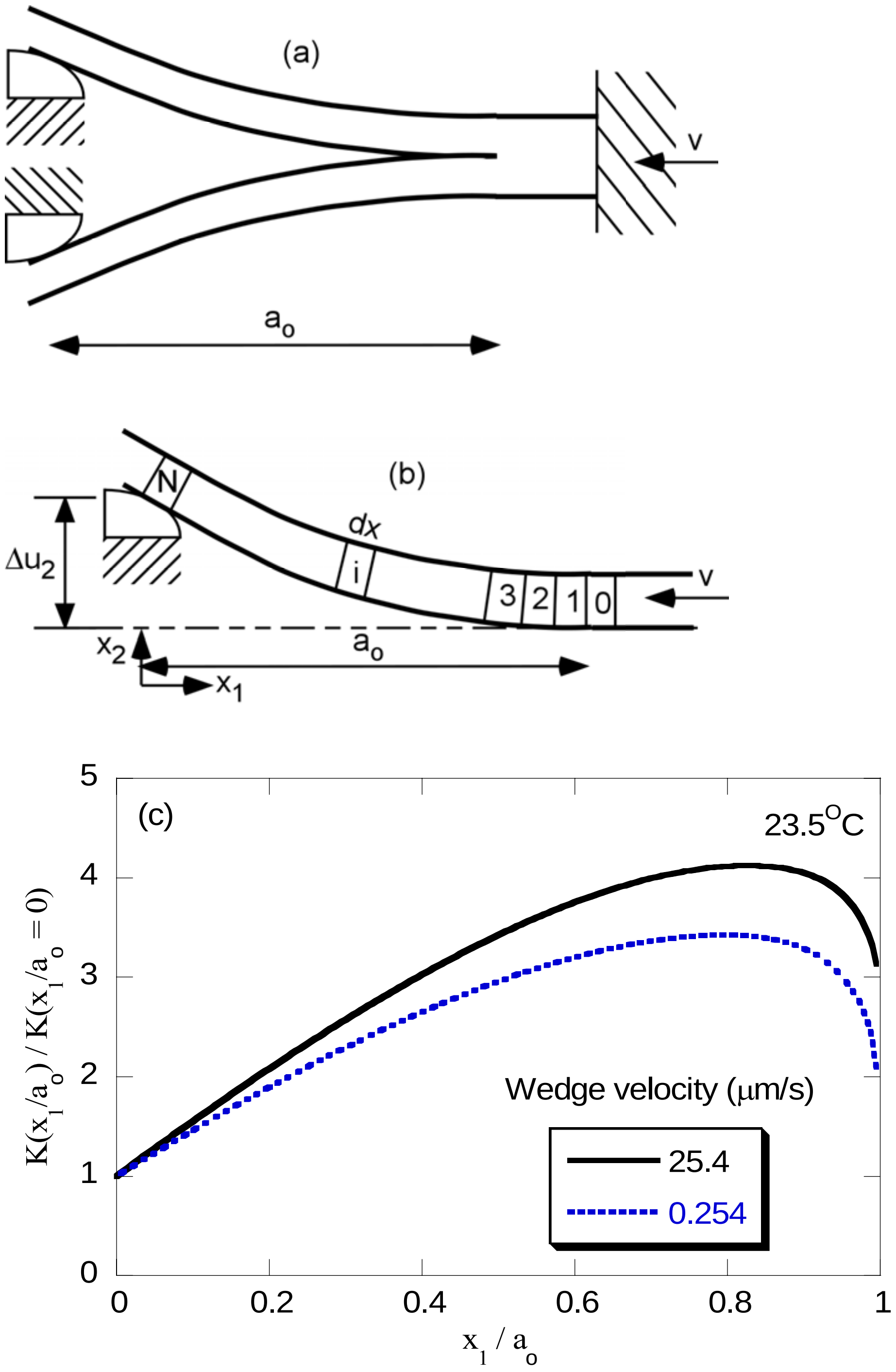

Figure 4.7: Control volume with crack length a_o during steady state. Segment #0 has zero curvature. Segment #1 to N have nonzero curvatures.

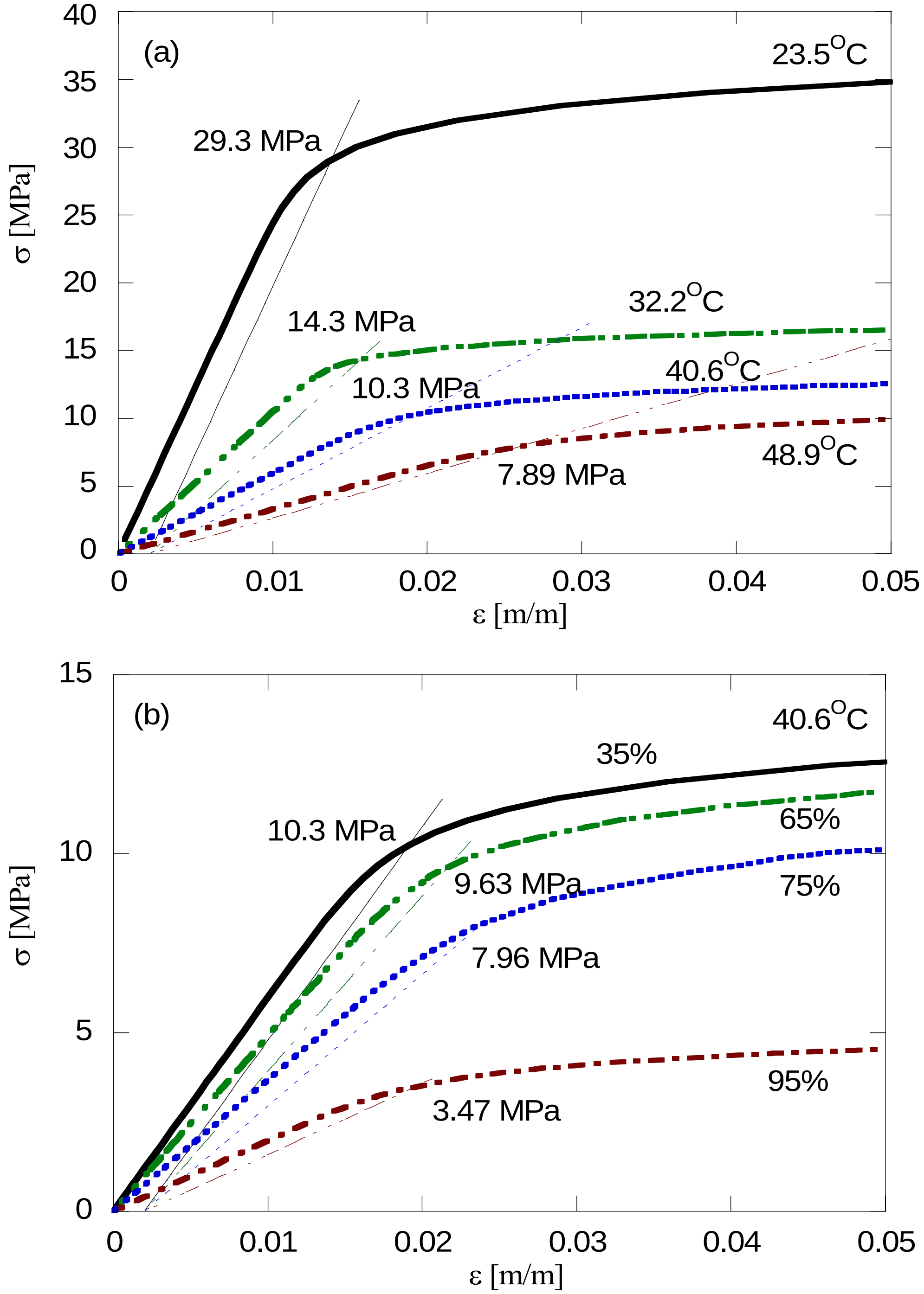

Figure 4.8: Onset stress σ^y of cohesive zones at (a) various temperature levels and (b) humidity levels.

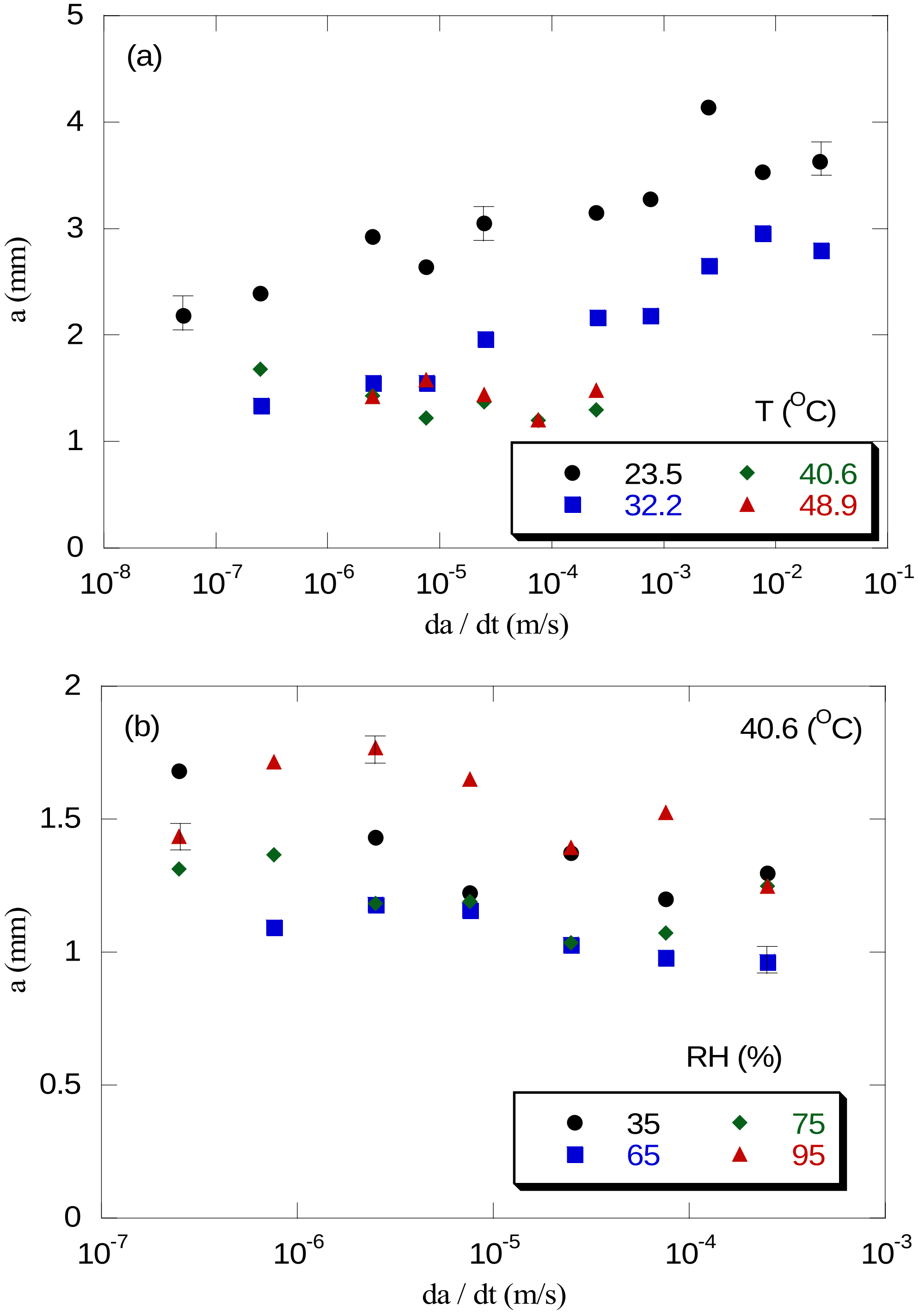

Figure 4.9: Crack length vs. wedge speed at (a) various temperature levels and (b) humidity levels.

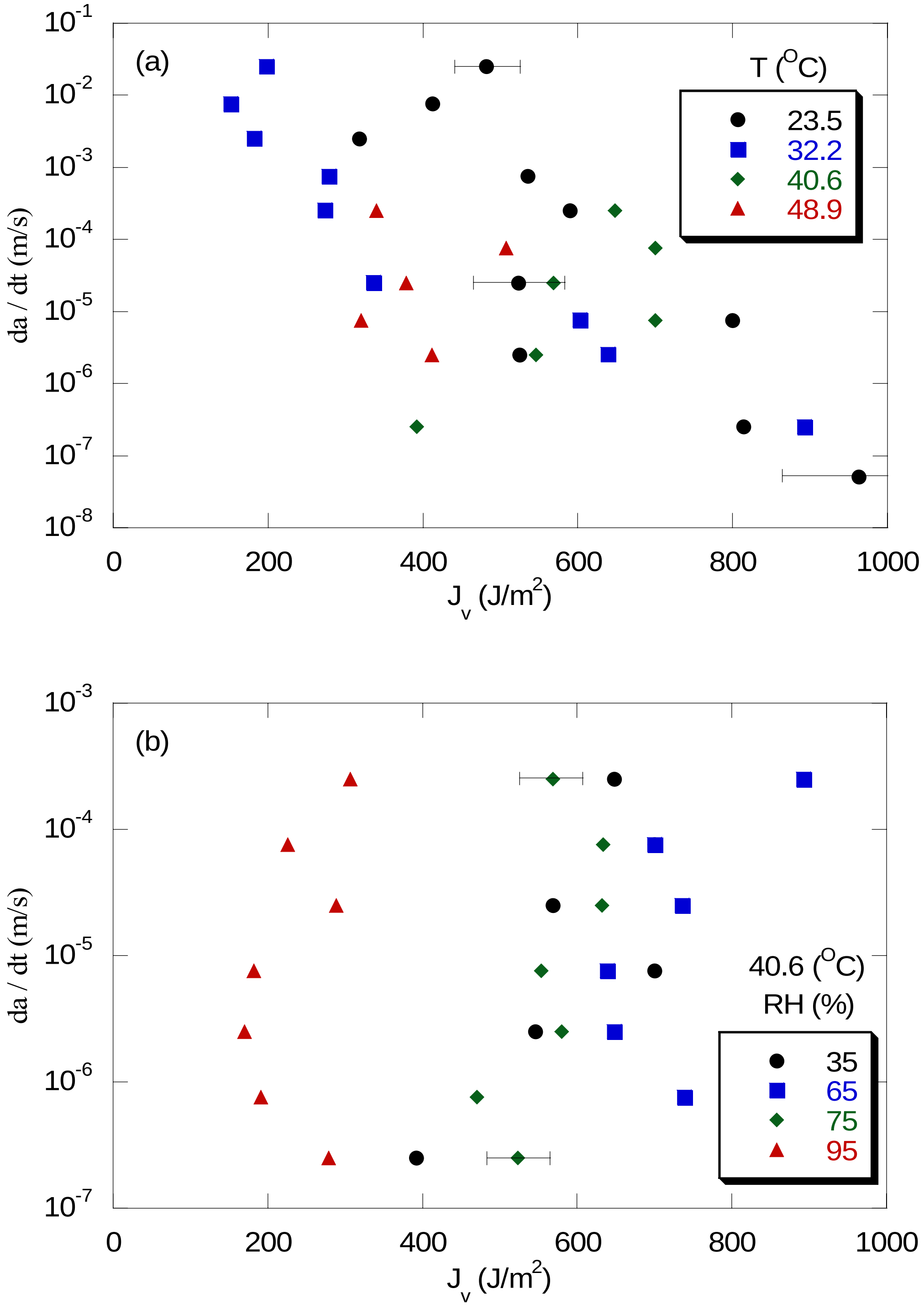

Figure 4.10: Crack speed vs. J_v at (a) various temperature levels and (b) humidity levels.

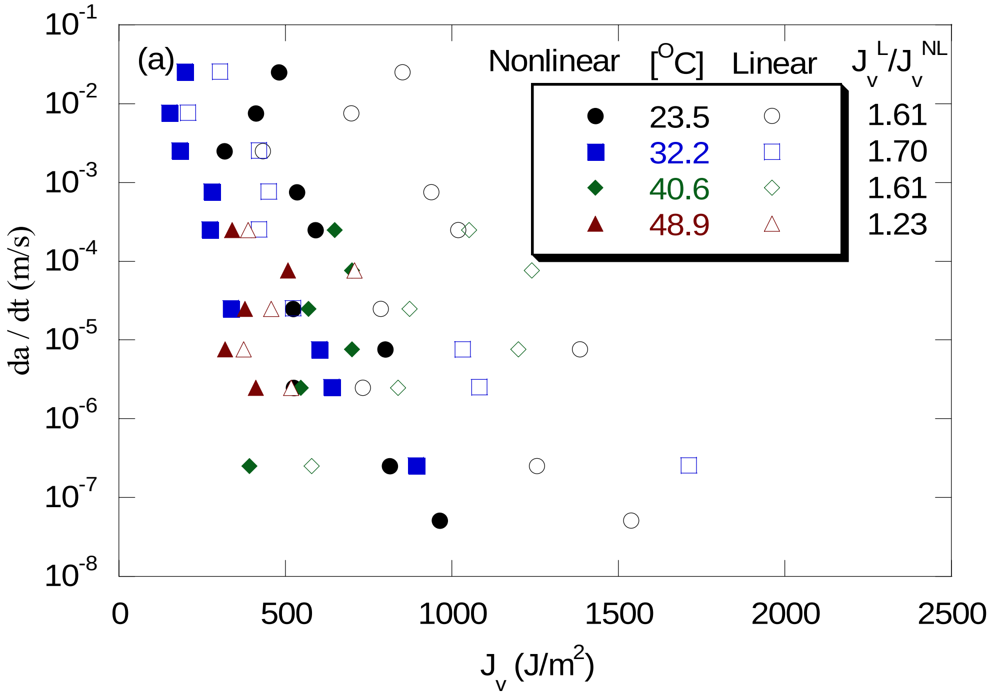

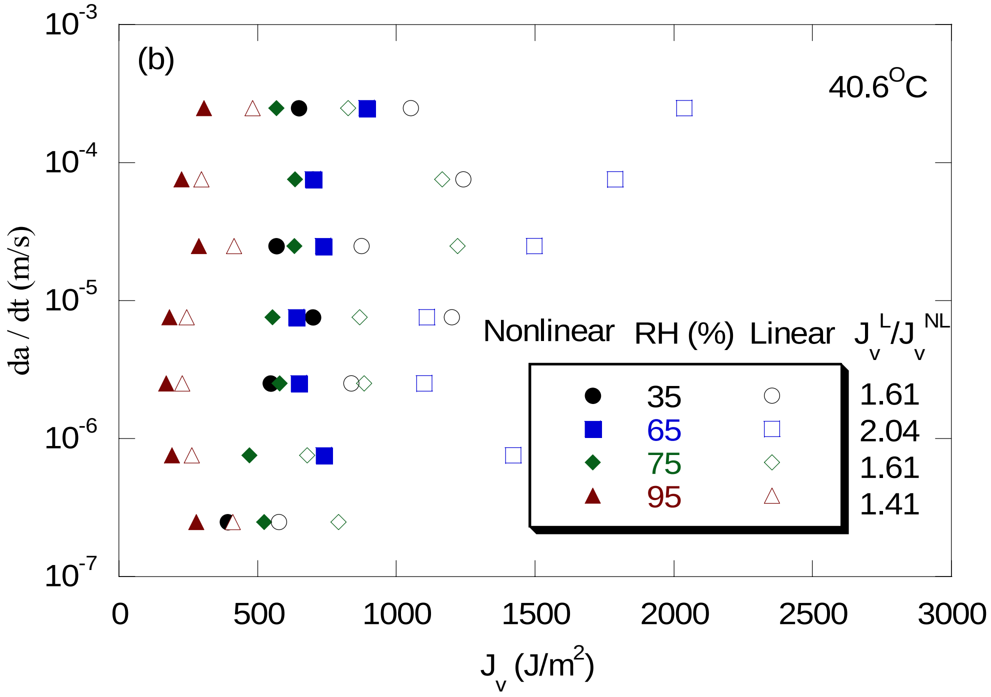

Figure 4.11: Comparison of J_v using linear and nonlinear viscoelasticity at (a) various temperature levels and (b) humidity levels.

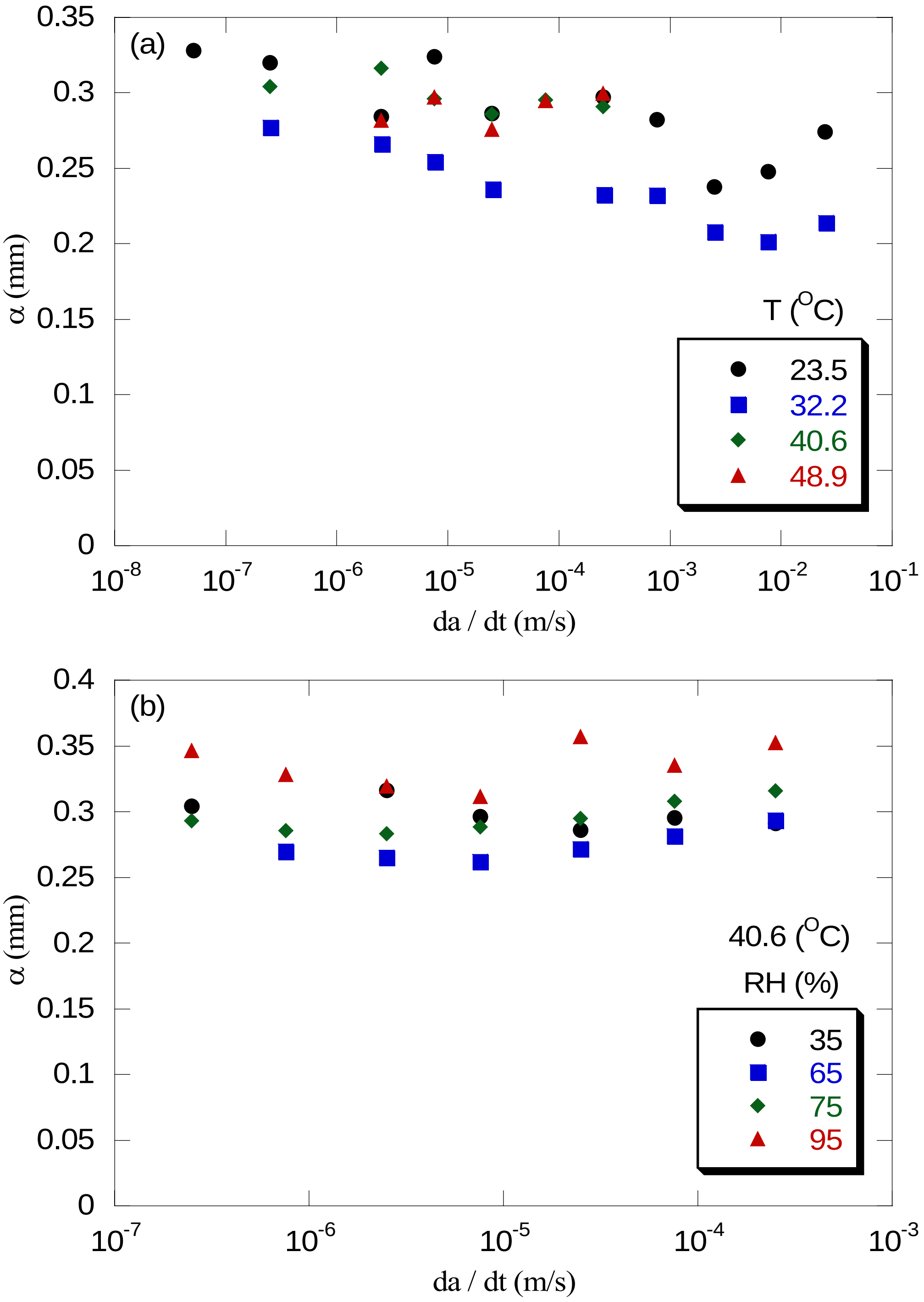

Figure 4.12: Cohesive zone size vs. crack speed at (a) various temperature levels and (b) humidity levels.

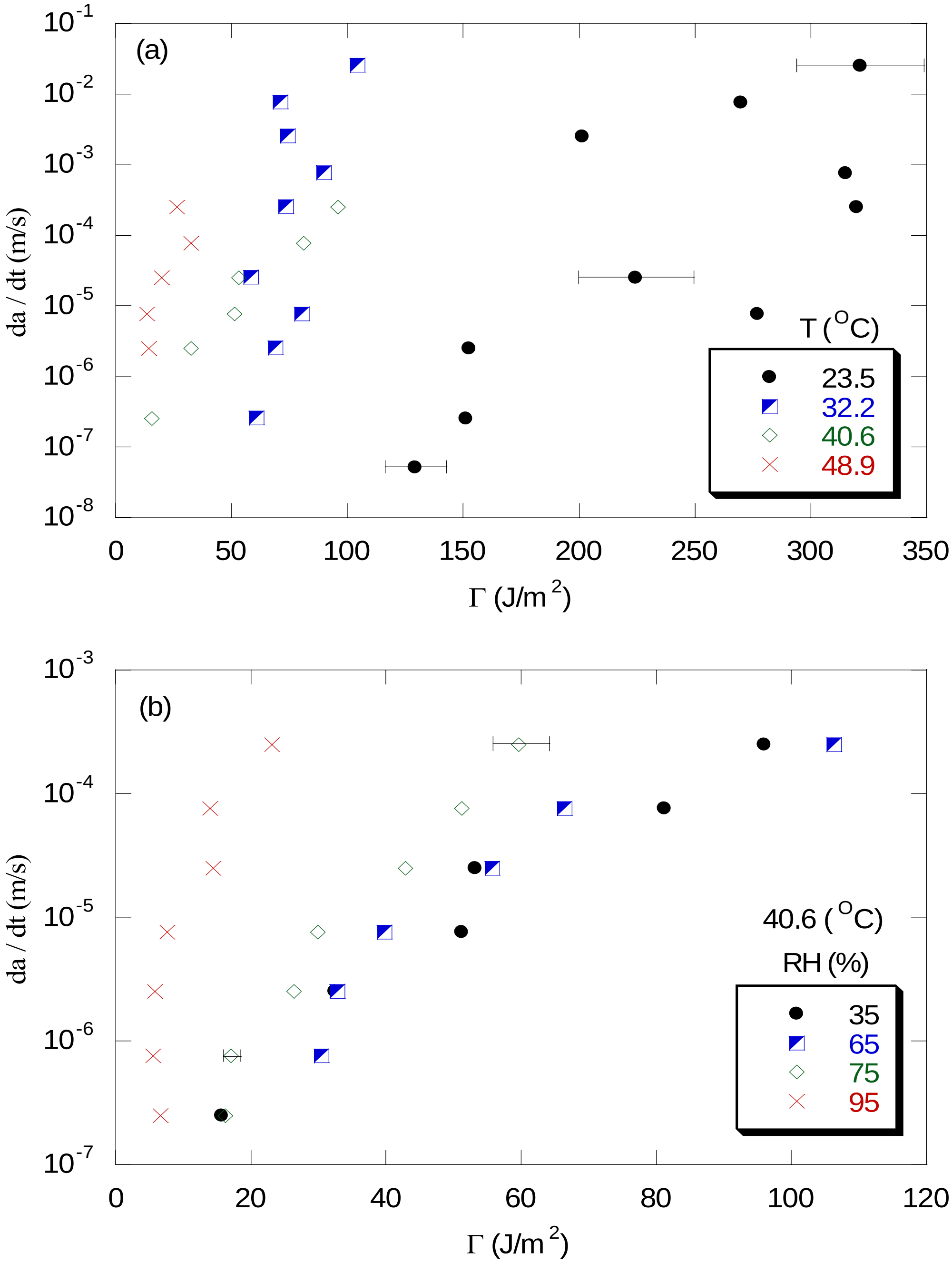

Figure 4.13: Crack speed vs. fracture energy at (a) various temperature levels and (b) humidity levels.

References

Allen, D. H. and Searcy, C. R., 'A micromechanical model for a viscoelastic cohesive zone,' *International Journal of Fracture* **107**, 2001, 159--176.

Arzoumanidis, G. A. and Liechti, K. M. 'Linear Viscoelastic Property Measurement and Its Significance to Some Nonlinear Viscoelasticity Models', *Mech. Time-Dependent Mater.* **7 (3-4),** 2003, 209--250.

Cao, H.C., and Evans, A.G., 'An Experimental Study of the Fracture Resistance of Bimaterial Interfaces,' *Mechanics of Material* **7**, 1989, 295-304.

Christensen, R.M., *Transaction of the Society of Rheology* **21** (1977), 163.

Christensen, R.M., 'A rate-dependent criterion for crack growth,' *International Journal of Fracture* **15**, No. 1, 1979, 3--21.

Christensen, R.M. and Wu, E.M, 'A Theory of Crack Growth in Viscoelastic Materials,' *Engineering Fracture Mechanics* **14**, 1981, 215--225.

Deng, T.H. and Knauss, W.G., 'The Temperature and Frequency Dependence of The Bulk Compliance of Poly(vinyl acetate). A Re-examination', *Mech. Time-Dependent Mater.* **1**, 1997, 33--49.

Doolittle, A.K., 'Studies in Newtonian Flow. II. The Dependence of the Viscosity of Liquids on Free-Space', *J. Appl. Mech.* **22**, 1951, 1471--5.

Drozdov, A., *Viscoelasic Structures – Mechanics of Growth and Aging*, Academic Press, 1998.

Dundurs, J., 'Edge-bonded dissimilar orthogonal elastic wedges', *J. Appl. Mech* **36**, 1969, 650--652.

Ferry, J. D., Viscoelastic Properties of Polymers, John Wiley & Sons, New York, 1980.

Gamby, D. and Chaoufi, J., 'Application of viscoelastic fracture criteria to progressive crack propagation in polymer matrix composites,' International Journal of Fracture, **100**, 1999, 379--399.

Georgiou, I., Ivankovic, A., Kinloch, A.J. and Tropsa, V., 'The Transferability of CZM Parameters between TDCB and IWP Specimens,' Proceedings of

27th Annual Meeting of The Adhesion Society, Inc., Feb 15-18, 2004, Wilmington, NC

Graham, G.A.C., 'The Correspondence Principle of linear Viscoelasticity Theory for Mixed Boundary Value Problems Involving Time-Dependent Boundary Regions, Q. Applied math. **26**, 1968, 167--174.

Guth, E. Wack, P.E. and Anthony, R.L., 'Significance of the Equation for State for Rubber', J. Appl. Phys. **17**, 1946, 347--351.

Hutchinson, J. W. and Suo, Z., Advances in Applied mechanics, **29**, 1992, 63--199.

Kaminsky, A.A. and Chernoivan, Y.A., 'On a crack in viscoelastic isotropic media opened by a rigid growing wedge', International Journal of Fracture, **117**, 2002, L15-L19.

Knauss, W.G., 'Stable and Unstable Crack Growth in Viscoelastic Media,' Transactions of the Society of Rheology 13:3, 1969, 291--313

Knauss, W.G., 'Delayed Failure – The Griffith Problem for Linearly Viscoelastic Materials', International Journal of Fracture Mechanics **6**, No. 1, 1970, 7--20.

Knauss, W.G. and Emri, I., 'Volume Change and the Nonlinearly Thermo-Viscoelastic Constitution of Polymers', Polymer Engineering and Science, **27**, No. 1, 1987, 86--100.

Knauss, W.G. and Emri, I., 'Non-Linear Viscoelasticity Based on Free Volume Consideration', Computers & Structures **13**, 1981, 123--8.

Knauss, W.G. and Kenner, V.H., 'On the Hygrothermomechanical Characterization of Polyvinyl Acetate', J. Appl. Phys. **51**, No. 10, 1980, 5131--5136.

Lai, J., Bakker, A. '3-D Schapery Representation for Non-linear Viscoelasticity and Finite Element Implementation,' Computational Mechanics **18**, 1996, 182--191.

Leaderman, H., ‘Elastic and Creep Properties of Filamentous Materials and Other High Polymers,’ The Textile Foundation, Washington, D.C., 1943.

Liechti, K.M. and Chai, Y.S., ‘Biaxial Loading Experiments for Determining Interfacial fracture toughness,’ J. Appl. Mech, Transactions of the ASME **59**, 1992, 295-304.

Liechti, K.M., Wu, J.D., ‘Mixed-Mode, Time-Dependent Rubber/Metal Debonding’, Journal of the Mechanics and Physics of Solids **49**, 2001, 1039—1072.

Losi, G.U. and Knauss, W.G., ‘Free Volume Theory and Nonlinear Thermoviscoelasticity’, Polym. Eng. Sci. **32**, 1992, 542--557.

Lou, Y.C. and Schapery, R.A., ‘Viscoelastic Characterization of a Nonlinear Fiber-Reinforced Plastic’, J. Comp. Mat. **5**, 1971, 208--234.

Ma, Z. and Ravi-Chandar, K., ‘Confined Compression: A Stable Homogeneous Deformation for Constitutive Characterization’, Experimental Mechanics **40**, 2000, 38--45.

Makhmutov, I.M., Sorina, T.G., Suvorova, Y.V. and Surgucheva, A.I., ‘Failure of Composites with Account for the Effects of Temperature and Moisture’, Mech. Composite Mater. **19**, 1983, 175--180.

Mamlouk, M.S. and Zaniewski, J.P., Materials for Civil and Construction Engineers, Addison-Wesley, 1999.

Matsuoka, S. and Maxwell, B., ‘Response of Linear high Polymer to Hydrostatic Pressure’, J. Polymer Sci. **32**, 1958, 131--159.

MBraceTM composite strengthening system specification, Master Builders, 1998.

McKinney, J.E., Edelman, S., and Marvin, R.S., ‘Apparatus for the Direct Determination of the Dynamic Bulk Modulus,’ J. Appl. Phys. **27**, 1956, 425--430.

Micro-Measurements, Precision Strain Gages (CEA-06-125UW-350), Engineering Data Sheet.

Nanni, A., ‘Composite: Coming on Strong’, Concrete Construction **44**, 1999, 120--125.

Park, S. J. and Liechti, K.M., ‘Rate-Dependent Large Strain Behavior of a Structural Adhesive’, Mech. Time-Dependent Mater. **7**, 2003, 143--164.

Popelar, C. F. and Liechti, K.M., ‘Multiaxial Nonlinear Viscoelastic Characterization and Modeling of a Structural Adhesive’, J. Engineering Materials and Technology., Transactions of the ASME **119**, 1997, 205--210.

Popelar, C. F. and Liechti, K.M., ‘A Distortion-Modified Free Volume Theory for Nonlinear Viscoelastic Behavior’, Mech. Time-Dependent Mater. **7**, 2003, 89--141.

Peretz, D. and Weitsman, Y, ‘Nonlinear Viscoelastic Characterization of FM-73 Adhesive’, Journal of Rheology **26**(3), 1982, 245--261.

Ravi-Chandar, K. and Ma, Z., ‘Inelastic Deformation in Polymers under Multiaxial Compression’ Mech. Time-Dependent Mater. **4**, 2000, 333--357.

Rice, J.R., ‘A Path Independent Integral and the Approximate Analysis of Strain Concentration by Notches and Cracks,’ J. Appl. Mech **35**, 1968 379--386.

Rice, J.R., ‘Elastic Fracture Mechanics Concepts for Interfacial Cracks,’ J. Appl. Mech **55**, 1988 98--103.

Rice, J.R. and Shih, G.C., ‘Plane Problems of Cracks in Dissimilar Media,’ J. Appl. Mech **32**, 1965 418--423.

Romanko, J. and Knauss, W.G., ‘On the Time Dependence of the Poisson’s Ratio of a Commercial Adhesive Material’, J. Adhesion **10**, 1980, 269--277.

Roy, S., 2003, private communication.

Sane, S.B. and Knauss, W.G., ‘The time-dependent bulk response of poly(methyl methacrylate)’, Mech. Time-Dependent Mater. **5**, 2001a, 293--324.

Sane, S.B. and Knauss, W.G., 'On Interconversion of Various Material Functions of PMMA', Mech. Time-Dependent Mater. **5**, 2001b, 325--343.

Saxena, A., 'Creep crack growth under non-steady-sate conditions.' ASTM STP 905, American Society for Testing and Materials, Philadelphia, 1986, 691--698.

Schapery, R.A., 'Application of Thermodynamics to Thermomechanical, Fracture, and Birefringent Phenomena in Viscoelastic Media', Journal of Applied Physics **35**, 1964, 1451--1465.

Schapery, R.A., 'A Method of Viscoelastic Stress Analysis Using Elastic Solutions', Journal of the Franklin Institute **279**, 1965, 268--289.

Schapery, R. A., 'An Engineering Theory of Nonlinear Viscoelasticity with Applications', Int. J. Solids Struct. **2**, 1966, 407--25.

Schapery, R. A., 'Further Development of a Thermodynamic Constitutive Theory: Stress Formulation', AA&ES Report No. 69-2, 1969a, Purdue University, West Lafayette.

Schapery, R.A., 'On the Characterization of Nonlinear Viscoelastic Materials', Polymer Engineering Science **9**, 1969b, 295--310.

Schapery, R.A., 'Nonlinear Facture Analysis of Viscoelastic Composite Materials Based on a Generalized J Integral Theory,' Composite Materials, K. Kawata & T. Akasak, Ed., Proc. Japan-U.S. Conference, Tokyo, 1981.

Schapery, R.A., 'Correspondence principles and a generalized J integral for large deformation and fracture analysis of viscoelastic media,' International Journal of Fracture **25**, 1984, 195--223.

Schapery, R.A., in Encyclopedia of Materials Science and Engineering, Pergamon Press LTD, 1986, 5043—5053.

Schapery, R.A., 'On some path independent integrals and their use in fracture of nonlinear viscoelastic media,' International Journal of Fracture **42**, 1990, 189—207.

Schapery, R.A., ‘Nonlinear Viscoelastic and Viscoplastic Constitutive Equations Based on Thermodynamics’, Mech. Time-Dependent Mater. **1**, 1997, 209--240.

Shen, Chi-Hung and Springer, G. S., ‘Moisture Absorption and Desorption of Composite Materials’, Journal of Composite Materials **10**, 1976, 2--20.

Shih, C.F. and Asaro, R.J., ‘Elastic-plastic analysis of cracks on biomaterial interfaces: Part I – small scale yielding,’ J. Appl. Mech, **55**, 1988, 299--316.

Swadener, J.G., Liechti, K.M., ‘Asymmetric Shielding Mechanisms in the Mixed-Mode Fracture of a Glass/Epoxy Interface,’ J. Appl. Mech, Transactions of the ASME **65**, 1998, 25-29.

Talybly, L.K., ‘Nonlinear Theory of Thermal Stresses in Viscoelastic Bodies’, Mech. Composite Mater. **19**, 1983, 419--425.

Tschoegl, N.W., Knauss, W.G. and Emri, I., ‘Poisson’s Ratio in Linear Viscoelasticity – A Critical Review’, Mech. Time-Dependent Mater. **6**, 2002, 3--51.

Viktorova, I.V., ‘Description of a Delayed Failure in Inelastic Materials with Account for Temperature’, Mech. Composite Mater. **19**, 1983, 35--38.

Williams, M.L., Landel, R. F., and Ferry, J. D., ‘The Temperature Dependence of Relaxation Mechanisms in Amorphous Polymers and Other Glass-forming Liquids’, J. Am. Chem. Soc. **77**, 1955, 3701--3707.

Williams, M.L., ‘The stress around a fault or crack in dissimilar media’, Bulletin of the Seismologic Society of America **49**, 1959, 199--204.

VITA

Soojae Park was born at Seoul in Republic of Korea on November 29, 1969 to Gapcheon Park and Keumja Yu. After graduating from Hanyung High School, Seoul in 1988, he started his college years at the Inha University in Incheon, Republic of Korea. He served in Republic of Korea Army as a military police from 1990 to 1993. He transferred to the University of Iowa at Iowa City, Iowa in 1994 and completed requirements of a Bachelors of Science degree from the Department of Mechanical Engineering in 1997. He received a Masters of Science at the Department of Aerospace Engineering and Engineering Mechanics in the University of Texas at Austin in 2000.

Permanent address: Majang-dong 504-1, Hanyang villa Ga, 204, Sungdong-gu,
Seoul, Korea
This dissertation was typed by the author.